Interference Suppression in Massive MIMO VLC Systems

Dissertation

zur Erlangung des akademischen Grades
Doktor der Ingenieurswissenschaften
(Dr.-Ing.)
der Technischen Fakultät
der Christian-Albrechts-Universität zu Kiel

vorgelegt von
Adrian Krohn

Kiel
2022

Tag der Einreichung: 30.12.2022
Tag der Disputation: 28.04.2023

Berichterstatter: Prof. Dr.-Ing. Peter Adam Höher
Prof. Dr.-Ing. Stephan Pachnicke

Vorwort

Die vorliegende Arbeit ist im Rahmen meiner Tätigkeit als wissenschaftlicher Mitarbeiter an den Lehrstühlen Informations- und Codierungstheorie sowie Nachrichtenübertragungstechnik entstanden. Die Arbeit an den beiden Lehrstühlen mit ihren unterschiedlichen Schwerpunkten erlaubte es mir, Einblicke in die zahlreichen Aspekte des Themas von unterschiedlichen Perspektiven aus zu erlangen. Ich danke Prof. Peter Adam Höher und Prof. Stephan Pachnicke dafür, dass sie mir diese Möglichkeit boten und dabei stets hilfreich, ermunternd und wohlwollend zur Seite standen und mit mir diese Arbeit zu Ende geführt haben. Ebenso danke ich herzlich Prof. Michael Höft und Prof. Robert Rieger für ihre Bereitschaft und Zeit zur Bildung der Prüfungskommission.

Auch danke ich den Kolleginnen und Kollegen beider Lehrstühle für die stets angenehme Arbeitsatmosphäre, allzeit offenen Türen, fruchtbaren Diskussionen, Mittagessen, Grillabende, spannenden (Dienst-)Reisen und gegenseitige Unterstützung – insbesondere Gilbert und Andrej für die erfolgreiche, gemeinsame Zeit im Büro und Labor! Darüber hinaus auch vielen Dank an meine Hiwis, die ebenso mit Rat und Tat an vielen Projekten mitgewirkt haben.

Für das immer erstklassige Korrekturlesen bedanke ich mich bei meinem hochgeschätzten Freund Lukas, sowohl für das akribische Lesen der vorliegenden Arbeit als auch der vorangegangenen Veröffentlichungen. Zu guter Letzt gilt der größte Dank meinen Eltern und auch meiner Schwester, ohne deren andauernde Unterstützung in allen Lebenslagen dies alles nicht möglich gewesen wäre.

Erklärung

Hiermit bestätige ich, dass die vorliegende Dissertation, abgesehen von der Beratung durch meinen Betreuer, nach Inhalt und Form meine eigene Arbeit ist. Die Arbeit wurde weder ganz oder zum Teil schon einer anderen Stelle im Rahmen eines Prüfungsverfahrens vorgelegt, ist bisher weder veröffentlicht worden und auch nicht zur Veröffentlichung eingereicht. Die Arbeit entstand unter Einhaltung der Regeln guter wissenschaftlicher Praxis der Deutschen Forschungsgemeinschaft. Ein akademischer Grad wurde mir bisher nicht entzogen.

Kurzfassung

Die vorliegende Arbeit befasst sich mit der Entwicklung und Auswertung von Interferenzunterdrückungsverfahren in Kommunikationssystemen mit mehreren Benutzern und Sendern, sogenannten Mehrbenutzer-MIMO-Systemen, im Bereich des sichtbaren Lichts (visible light communication, VLC). Bei sehr vielen Sendern, wie sie hier angenommen werden, wird auch von einem "Massive MIMO"-System gesprochen. Die einzelnen Komponenten werden unter besonderer Berücksichtigung des benötigten Hardware-Aufwands und geeigneter Modulationsverfahren betrachtet und modelliert. Hierbei wird die Interkanal-Interferenz zwischen den Benutzern als besonders kritisch identifiziert. Um diese zu unterdrücken, werden verschiedene vorhandene Methoden untersucht sowie als Hauptaspekt dieser Arbeit eine neuartige aktive Interferenzunterdrückung eingeführt, welche auf der Verwendung von Flüssigkristallanzeigen (LCD) basiert.

Diese Technologie ermöglicht eine dynamische Anpassung des physikalischen Übertragungskanal. Im Gegensatz zu algorithmischen oder software-basierten Methoden, kann die LCD-basierte Interferenzunterdrückung die einzelnen Übertragungskanäle trennen ohne auf der Sendeseite die Lichtquellen zu beeinflussen, was besonders bei "Dual Use"-Systemen mit Raumbeleuchtung vorteilhaft ist. Auch können fremde Interferenz-Quellen wie natürliches Licht oder Sender benachbarter Zellen unterdrückt werden ohne auf diese direkt einwirken zu müssen. Dafür wird bei jedem Benutzer ein LCD-Filter vor dessen Photodetektor platziert und die Pixel entweder transparent oder undurchlässig geschaltet, sodass die Störeinflüsse abgeschattet werden und nur die gewünschten Lichtquellen vom Detektor aus sichtbar sind. Die Wirksamkeit dieses Vorgehens wird mit derer einer "Zero Forcing"-Vorkodierung für verschiedene Szenarien und Anwendungen simulativ ausgewertet und in einem experimentellen Versuchsaufbau, der im Rahmen dieser Arbeit dafür entwickelt wurde, bestätigt.

Die Zuordnung der Sende-Lichtquellen zu den einzelnen Benutzern ist dabei von großer Bedeutung für die Systemleistung, sodass sich ein Optimierungsproblem ergibt, welche Zuordnung und dementsprechende LCD-Pixelmuster vorteilhaft sind. Dieses Optimierungsproblem wurde hier als "Santa Claus-Problem auf unabhängigen, parallelen Maschinen",

welches aus der Informatik bekannt ist, modelliert. Dabei ist das Ziel der Optimierung die Maximierung des auftretenden minimalen Signal-zu-Interferenz-Verhältnis über alle Benutzer hinweg. Als Lösungsansätze werden in dieser Arbeit eine genetische evolutionäre Optimierung sowie ein neues heuristisches Verfahren angewandt.

Abstract

The focus of this dissertation is on the development and evaluation of methods and principles to mitigate interference in multiuser visible light communication (VLC) systems using several transmitters. All components of such a massive multiple-input multiple-output (MIMO) system are considered and transformed into a communication system model, while also paying particular attention to the hardware requirements of different modulation schemes. By analyzing all steps in the communication process, the interchannel interference between users is identified as the most critical aspect. Several methods of suppressing this kind of interference, i.e. to split the MIMO channel into parallel single channels, are discussed, and a novel active LCD-based interference suppression principle at the receiver side is introduced as main aspect of this work.

This technique enables a dynamic adaption of the physical channel: compared to solely software-based or static approaches, the LCD interference suppression filter achieves adaptive channel separation without altering the characteristics of the transmitter lights. This is especially advantageous in dual-use scenarios with illumination requirements. Additionally, external interferers, like natural light or transmitter light sources of neighboring cells in a multicell setting, can also be suppressed without requiring any control over them. Each user's LCD filter is placed in front of the corresponding photodetector and configured in such a way that only light from desired transmitters can reach the detector by setting only the appropriate pixels to transparent, while light from unwanted transmitters remains blocked. The effectiveness of this method is tested and benchmarked against zero-forcing (ZF) precoding in different scenarios and applications by numerical simulations and also verified experimentally in a large MIMO VLC testbed created specifically for this purpose.

Distributing the transmitter light sources to the users with the help of the LCD filter rises the optimization problem of how to allocate them correctly and how to set the LCD pixels so that the quality of the users' subchannels increases. This problem is modeled as "Santa Claus problem on unrelated parallel machines", known from computer science, and solved by genetic evolutionary optimization and a novel heuristic approach in order to maximize the minimum signal-to-interference ratio across all users.

Contents

1 Introduction **1**

1.1 Problem Statement and Motivation . . . 2
1.2 State of the Art . . . 3
1.3 Author's Contributions . . . 5
1.4 Structure of this Dissertation . . . 7

I Fundamentals **9**

2 VLC Channel Modeling **11**

2.1 SISO Channel Models . . . 12
2.1.1 Indoor Scenario . . . 13
2.1.1.1 Line of Sight . . . 14
2.1.1.2 Diffuse Light . . . 15
2.1.2 LCD Interference Suppression Filter . . . 16
2.2 MIMO Channel Models . . . 17
2.2.1 Massive MIMO Aspects . . . 18
2.2.2 Multiuser Aspects and Precoding . . . 18
2.2.3 Interference . . . 19
2.2.3.1 Performance Metric . . . 19
2.2.3.2 Interchannel Interference . . . 21
2.2.3.3 Multicell Interference . . . 22
2.2.3.4 Ambient Light . . . 23
2.3 Summary . . . 23

3 Signal Design, Modulation and Coding Schemes **25**

3.1 Binary Modulation Schemes . . . 26
3.2 Discrete-Level Modulation Schemes . . . 26
3.2.1 Pulse Amplitude Modulation and Variants . . . 27

3.2.2 Superimposed Intensity Modulation . . . 27
3.3 AMI and Return-to-Zero Variants . . . 27
3.4 Optical OFDM and Variants . . . 31
3.4.1 OFDM Fundamentals . . . 31
3.4.2 Real-Valued and Non-Negative OFDM . . . 31
3.5 Optical CDMA . . . 31
3.6 Color Modulation . . . 32
3.7 Spatial Encoding . . . 33
3.8 Summary . . . 33

II Methodology 35

4 Interference Suppression Methods and Filters 37
4.1 Algorithmic Approaches . . . 38
4.2 Active Optical Suppression . . . 39
4.2.1 Aperture Areas and Patterns . . . 41
4.2.2 Separating Power of the LCD Filter . . . 43
4.2.3 Allocation Schemes . . . 43
4.2.3.1 Santa Claus Problem Modeling . . . 46
4.2.3.2 Heuristic Optimization . . . 46
4.2.3.3 Genetic Evolution Optimization . . . 47
4.2.3.4 Iterative Combining of Approaches . . . 48
4.3 Passive Optical Suppression . . . 51
4.3.1 Camera-based Receiver . . . 52
4.3.2 Imaging Optics . . . 53
4.4 Summary . . . 54

5 Numerical Simulation Model 55
5.1 Simulation Model . . . 55
5.1.1 Modeling of the LCD Filter . . . 57
5.1.2 Modeling of the Photodetector . . . 58
5.1.3 Pre-Calculation of Channel Coefficients . . . 59
5.2 Evaluating of Different Scenarios and Methods . . . 60
5.2.1 Single-User Scenario with Spatial Modulation and Spatial Multiplexing 61
5.2.2 Combination of ZF Precoding and Genetic LCD Optimization . . . 62

5.2.3 Massive MIMO Scenario . . . 67
5.2.4 Multicell Scenario . . . 72
5.3 Summary . . . 72

III Hardware and Experiments 75

6 VLC Transmitter and Receiver Components 77
6.1 Light-Emitting Diodes . . . 77
6.1.1 Electrical Characteristics . . . 77
6.1.1.1 Large-Signal Model . . . 78
6.1.1.2 Small-Signal Model . . . 79
6.1.2 Optical Characteristics . . . 79
6.2 LED Driver Circuits . . . 81
6.2.1 Steady-State Operation . . . 81
6.2.2 Binary Switching . . . 83
6.2.3 Continuous Modulation . . . 84
6.2.3.1 Linear Amplifier with Bias Tee . . . 84
6.2.3.2 Buck Converter . . . 85
6.2.3.3 Analysis of DMT Modulation with Buck Converter . . . 88
6.2.4 Discrete-Step Amplitude Variation . . . 90
6.2.4.1 Experimental Analysis of a Discrete-Step Driver . . . 92
6.2.4.2 Experimental PAM-4 LED-to-Camera Transmission . . . 93
6.3 LCD Filter . . . 95
6.3.1 Physical Composition . . . 95
6.3.2 Optical Characterization . . . 99
6.3.2.1 Single LC Cell . . . 99
6.3.2.2 LCD Color and Monochrome Displays . . . 102
6.3.2.3 Aberration Errors . . . 102
6.3.3 PDLC Foil . . . 106
6.3.3.1 PDLC Technology and Filter Effect . . . 106
6.3.3.2 PDLC Characterization . . . 107
6.4 Photodetectors . . . 108
6.4.1 Optical Characteristics . . . 109
6.4.2 Electrical Characteristics . . . 110
6.5 Receiver Circuits . . . 111

6.6 Summary . . . 113

7 Experimental Testbed **115**
7.1 Conception . . . 115
7.2 Setting . . . 116
7.3 Transmitter Design . . . 117
7.3.1 LED Transmitter Modules . . . 117
7.3.2 Control Unit . . . 119
7.3.3 Bus Design and Control Signals . . . 119
7.3.4 Repeater Modules . . . 121
7.4 Receiver Design . . . 122
7.4.1 Photodiode and TIA . . . 122
7.4.2 LCD, ADC and Raspberry Pi Setup . . . 124
7.4.3 LCD Control . . . 125
7.5 Experimental Results . . . 126
7.6 Summary . . . 127

8 Conclusion **129**

Appendix **133**

A Notation **133**

B LPT-SC-UPM Allocation Algorithm **137**

C LC Cell Color Transmittance Characteristics **141**

D VLC Testbed **143**
D.1 Python Transmitter Example . . . 143
D.2 Arduino Transmitter Firmware . . . 144
D.3 LCD and ADC Example with Bar Search . . . 146
D.4 Transmitter Schematic . . . 150

Bibliography **151**

1

Introduction

Light – this fraction of the electromagnetic spectrum is the key to everything on this planet – without light, life as we know it would not exist. Light is safety, warmth and comfort, a crucial accelerator in human history. When humans first mastered the art of sparking a fire, it marked a point of no return in the development of our civilization. Since then, the excessive usage of natural and artificial light sources can be seen throughout the centuries. Controlling light at our fingertips enables us to be independent of the day-night cycle.

Artificial visible light can be created with various devices and practices, like fire, carbon-arc lamps, incandescent lamps, gas discharge lamps of different types and shapes and the latest newcomer in terms of illumination: solid-state lights like light-emitting diodes (LEDs).

But illumination and warmth are not the only purposes. Since ancient times, light also carries information, from fire or lighthouse beacons to optical semaphores – applications of this kind are used even today. Alexander Graham Bell used sunlight for the first wireless transmission of human speech with his newly invented photophone in 1880 [Bel80]. Here, the sunlight is concentrated on a voice-coupled mirror, and the vibrating mirror modulates the intensity of light while speaking into the transmitter. In the receiver, an early photo-cell was used to convert the light into an electric current in order to drive an earphone. When electric lighting was established in late 19th century, it was also used as reliable carrier for data, e.g. in morse code transmitters for nautical applications.

Speaking more generally, information exchange with the help of visible light is nowadays known as visible light communication (VLC), but the main principle remains the same: data is transmitted wirelessly by modulating light in a free-space medium. Together with the most common application of artificial light – illuminating indoor rooms – these two

applications can be realized simultaneously in an equal manner by the same device.

Nowadays, the most wide-spread device for creating light is the light-emitting diode (LED). Conventional light sources like incandescent or fluorescent lamps can be replaced by LEDs in almost every scenario. There is quite no application, where LEDs are not superior in terms of energy efficiency, costs and quality of light. Because of this, LEDs are widespread in private, commercial and public installations, and their usage still increases – indoors as well as outdoors. Because of the fact that LEDs are relatively small and also limited in power, many of them are grouped together in order to form an array. These can be used in single lamps or can be distributed over a larger space to realize a surface-like emitter. Regarding data communication, LEDs are also quite suitable. They are solid-state light sources – which means semiconductors, consequently, they can be switched or modulated with high frequency without losing lamp lifetime. Hence, this dissertation will focus solely on the use of LEDs for creating light.

1.1 Problem Statement and Motivation

The requirements for illumination and communication differ strongly. Because illumination of rooms demands in general an even level of light and also a consistent color temperature with high a color rendering index (CRI), lamps must be distributed in such a way that there are no dark spots or ones which are too bright. Their emission patterns should be broad and must overlap in order to fulfill this condition. In a data transmission scenario, this is counterproductive because the overlap leads to interference between the emitted light from the light sources. The different intensities emitted by incoherent light sources like LEDs add up constructively [Hoe19; WW$^+$18] compared to laser sources. When many LEDs are present in a wide-spread spatial lighting scenario, this arrangement can be interpreted as a large transmitter array when it comes to data communication. Thus, together with users respectively receivers available, a multiuser multiple-input multiple-output (MU-MIMO) communication system can be established. When the number of transmitters is much higher than the number of receivers, this system can be considered as massive MIMO system. Such a system can unlock its full potential only, when a simultaneous transmission of parallel data streams for all receivers without crosstalk between them is possible. As stated before, this contradicts the illumination aspects, hence, technical solutions for interference suppression are wanted to enable both high-quality illumination and data transmission.

From the communication point of view, this means a diagonalization of the channel matrix while leaving the transmitter emission characteristics unaltered. The channel matrix

combines the influences of all physical components in the transmission system: the transmitter characteristics, the geometry and physical behavior of the indoor or free-space channel and the receiver characteristics. Besides an algorithmic approach, the only component left to modify is the receiver. Therefore, the focus of this dissertation lies on receiver-side measures when it comes to interference suppression. In a multiuser scenario, each receiver should be able to take action in respect of interference of different types. By doing so, it is the receivers' task to modify the formerly rank-deficient channel matrix to a full rank, diagonalized matrix, which enables an interference-free transmission of parallel data streams.

In this dissertation, several methods for interference mitigation are introduced and discussed. Special focus is paid to a novel technique based on a liquid crystal (LC)-based device: An LC array, based on an LC display (LCD), is placed in front of the photodetetor and controlled in such a way that only desired light can reach the detector by setting the pixels to either transparent or opaque. This technique is a promising candidate of receiver-side interference mitigation and evaluated in terms of practicality, effectiveness and limits in the next chapters.

1.2 State of the Art

In order to solve the interference problem, many approaches take inspiration from radio frequency (RF) systems. Here, the available domains for modulation techniques which employ a mitigation of crosstalk between channels are the time domain, the frequency domain, the spatial domain and the coding domain. There are also more general approaches, which try to remove the influence of the physical transmission channel. It should also be mentioned that the well-known water-filling method is not the optimal solution for maximizing the throughput as in RF systems. In intensity-modulated/direct-detection systems like VLC, this power allocation problem is of non-convex nature, so different methods are required [CR$^+$17; CR$^+$18]. Due to the incoherent light, destructive interference cannot be exploited, too, as in laser-based communication systems [Koo18; KG$^+$18]. There are several approaches in various publications of adapting these RF schemes to increase the data rate or robustness or introducing novel schemes. In [Arn15; Sch11; Sch16], the adaption of orthogonal frequency-division multiplexing (OFDM) for incoherent, visible light is presented and discussed. Spatial modulation is done by [OT$^+$18] and spatial multiplexing is evaluated in [LK20]. The optical variant of code-division multiple access is given in [CS$^+$89] and [Hoe19]. Some of these modulation and coding techniques are suggested in the cur-

rently available VLC standards. The IEEE 802.15.7 standard specifies on-off keying (OOK), variable pulse position modulation (VPPM) and also color-shift keying (CSK) as main modulation techniques [IEE19]. Compared to that, the ITU G.9991 standard recommends a real-valued OFDM variant [ITU19]. Zero-forcing (ZF) precoding and successive interference cancellation (SIC) are considered and discussed in [SS$^+$04; HC$^+$13; YB$^+$13; YC$^+$18]. All these methods have in common that they rely purely on an algorithmic approach which cannot remove the interference in a physical way.

Hence, the performance varies greatly dependent on the channel conditions. In high crosstalk scenarios – such as a massive MIMO system, their effectiveness is suffering. In a multicell setting, the complexity increases additionally. Here, the interference of neighboring cells needs to be addressed, too. The presented methods can be extended to a cooperating-cells approach, where interference is mitigated inside the current cell and between neighboring cells in different steps [AM$^+$18; PP19; HY$^+$20].

However, in order to achieve a better performance in high-crosstalk scenarios, a promising approach is to manipulate the physical channel itself in such a way that the interference is eliminated directly. A convenient way of doing so is to adapt the receivers – especially when the interferers are out of reach or cannot be modified. Suitable methods are e.g. to equip users with imaging receivers, where lenses or mirrors are used to image the transmitter array on to a receptor plane. This plane can be a camera-based receptor or an array of individual photodetectors [GC18; JW$^+$18]. In [PO$^+$17], a non-imaging mirror approach is presented and in [CM$^+$16] a geometric pyramid-shaped modification. Together with a software processing, the transmitter light sources can be distinguished and decoded separately. Here, the receivers look only in certain directions, which means their performance is also highly dependent on their orientation. A main drawback of CMOS sensors, as used in cameras, is their low sample rate compared to regular photodetectors although they offer a high number of receive elements (pixels).

To overcome these specific drawbacks of receiver modifications while keeping the ability to separate between light sources, the usage of the introduced, novel LCD filter with its pixel array is suggested in this dissertation. LC filters have been previously used to alter light in a physical way. In [Elr93], a method is presented for steering light in infrared communication systems by placing an LCD filter in front of each transmitter. Obviously, this is not compatible with dual-use illumination applications because of the location of the LCD filter and the resulting spot light when used with visible light. In [WL$^+$12], this principle of steering light is also applied to display applications. Another usage of LC technology is reported in [NN$^+$21b; NN$^+$21a; AM$^+$22; NN$^+$22], where a so-called intelligent-surface LC

device is used for generating a channel gain in VLC systems.

1.3 Author's Contributions

The author's publications focus on LCD interference mitigation as the main topic in various scenarios and applications. In [KH+22], a massive MIMO LED array is assumed and the effectiveness of the LC-based interference mitigation is evaluated in terms of numerical simulation and experimental verification. In [KP+22], a genetic evolutionary optimization of these LC receivers is applied to the LCD interference suppression filter, whereas in [KF+19], the LCD filter is initially introduced and compared to conventional spatial encoding schemes.

Other publications deal with VLC components or special types of VLC channels. In [KH+20], a transmitter for alternate mark inversion and dimming support is presented and experimentally verified. In [KH+18a], a step-down converter is evaluated in terms of LED driver and modulation capability for variants of OFDM. [KH+18b] deals with the special case of LED-to-camera transmission and its limits. In [KF+17], a passive interference mitigation method is presented as predecessor of the above-mentioned LC-based active interference suppression.

Own Contributions

[KF+17] A. Krohn, G. J. M. Forkel, P. A. Hoeher, and S. Pachnicke, "Capacity-increasing 3D spatial demultiplexer design for optical wireless MIMO transmission," presented at the 2017 European Conference on Optical Communication (ECOC), Gothenburg, Sweden, 2017, pp. 1–3. DOI: 10.1109/ECOC.2017.8346021.

[KF+19] A. Krohn, G. J. M. Forkel, P. A. Hoeher, and S. Pachnicke, "LCD-based optical filtering suitable for non-imaging channel decorrelation in VLC applications," *IEEE/OSA Journal of Lightwave Technology*, vol. 37, no. 23, pp. 5892–5898, Dec. 2019. DOI: 10.1109/JLT.2019.2941734.

[KH+18a] A. Krohn, P. A. Hoeher, and S. Pachnicke, "Visible light communication with multicarrier modulation utilizing a buck-converter circuit as efficient LED driver," in *Proc. ITG-Fachtagung Photonische Netze*, Leipzig, Germany, 2018, pp. 48–52.

[KH+18b] A. Krohn, P. A. Hoeher, and S. Pachnicke, "Visible light tricolor LED-to-camera data transmission suitable for internet-of-things and sensor applications," presented at the 2018 European Conference on Optical Communication (ECOC), Rome, 2018, pp. 1–3. DOI: 10.1109/ECOC.2018.8535387.

[KH+20] A. Krohn, P. A. Hoeher, and S. Pachnicke, "Single-LED VLC-transmission with AMI and RZ-OOK for dimming support at fixed data rate," presented at the Advanced Photonics Congress (SPPCom 2020), Montreal, Canada, 2020. DOI: 10.1364/SPPCOM.2020.SpM4I.3.

[KH+22] A. Krohn, A. Harlakin, S. Arms, S. Pachnicke, and P. A. Hoeher, "Impact of liquid crystal based interference mitigation and precoding on the multiuser performance of VLC massive MIMO arrays," *IEEE Photonics Journal*, vol. 14, no. 5, Art. no. 7348112, Oct. 2022. DOI: 10.1109/JPHOT.2022.3199614.

[KP+22] A. Krohn, S. Pachnicke, and P. A. Hoeher, "Genetic optimization of liquid crystal matrix based interference suppression for VLC MIMO transmissions," *IEEE Photonics Journal*, vol. 14, no. 1, Art. no. 7300705, Feb. 2022. DOI: 10.1109/JPHOT.2021.3126211.

Co-Authored Contributions

[FK+19] G. J. M. Forkel, A. Krohn, and P. A. Hoeher, "Optical interference suppression based on LCD-filtering," *Applied Sciences*, vol. 9, no. 15, Art. no. 3134, Aug. 2019. DOI: 10.3390/app9153134.

[HK+22] A. Harlakin, A. Krohn, and P. A. Hoeher, "Liquid crystal display based angle-of-arrival estimation of a single light source," *IEEE Photonics Journal*, vol. 14, no. 3, Art. no. 6829312, Jun. 2022. DOI: 10.1109/JPHOT.2022.3172511.

Patent Applications

Regarding interference mitigation in VLC MIMO systems as part of this dissertation, the following German patent was published. Later, it was extended as EU patent, which was published on 28 October 2020.

[KF+17] A. Krohn, G. J. M. Forkel, P. A. Hoeher, and S. Pachnicke, "Verwendung eines Bildanzeigegeräts, Verfahren für die optische Freiraum-Signalübertragung nebst dazugehöriger Vorrichtung," German Patent DE 10 2017 130 903.9, Dec. 21, 2017.

[KF+20] A. Krohn, G. J. M. Forkel, P. A. Hoeher, and S. Pachnicke, "Use of an image display device, method for optical free-space signal transmission together with associated apparatus," EU Patent EP 3 729 685 A1, Oct. 28, 2020.

1.4 Structure of this Dissertation

This dissertation is divided into three main parts, which are divided in different chapters. Each chapter deals with a specific aspect of a VLC system and is concluded with a brief summary. In Chapter 2, the VLC channel model is derived for the single-input single-input single-output (SISO) case and extended to a MIMO setting. The before-mentioned LCD filter is integrated into the channel model, too. Here, the special case of an indoor scenario is considered and different types of interferers are introduced, followed by a discussion about a suitable performance metric. Chapter 3 deals with modulation techniques, which can be used in VLC systems. Starting from low-complexity variants like OOK, higher-order schemes like OFDM are considered, too.

In the second part – which is the main topic of this dissertation – the methodology and main principles of interference suppression are presented. The LCD filter is evaluated and different optimization strategies for improving the data link are discussed in Chapter 4. Additionally, other methods are also mentioned including passive ones. For evaluation of the presented measures, a numerical simulation based on a ray-tracing model is introduced in Chapter 5, where the channel model from Chapter 2 is integrated. Several different scenarios are taken, and the performance in terms of link quality is calculated and discussed.

Finally, the third part presents the required physical hardware components of a VLC system and introduces a room-sized massive MIMO testbed: Chapter 6 takes the blocks from the channel model in Chapter 2 and suggests real-life components and their characteristics derived from measurements, while Chapter 7 reveals the testbed in detail regarding hardware and software aspects. Measurements of the realized LCD interference suppression filter are presented. In Chapter 8, a summarizing conclusion and directions for future research are given.

Part I

Fundamentals

2

VLC Channel Modeling

Visible light communication (VLC) is a subcategory of optical wireless communication (OWC), in which light is used to transmit data in free space. For this purpose, VLC uses – as the name suggests – light in the visible range of the electromagnetic spectrum (380 nm – 780 nm) [93]. Because of that, a VLC system has different constraints and application scenarios compared to a radio-frequency (RF) communication system: Light can easily be blocked, which not always is a drawback. For example, a high re-use factor can be achieved in indoor scenarios. It can be deployed in lighting systems enabling a dual-use gain, and light does not get disturbed in areas with high electromagnetic interference, like factory halls; and vice versa, light does not interfere with electronic equipment, making it a good choice in sensitive areas like hospitals and aircraft.

But compared to RF, a VLC system is an intensity-modulated/direct-detection (IM/DD) system, which means that there is no phase information available as well as there is no destructive interference between light emitted by different light sources.[1] Thus, the suitable set of modulation schemes is reduced to formats with a real-valued and non-negative signal output [KB97]. Also, different types of drivers are available, which put some constraints on the modulation schemes, which are presented in Chapter 6.2.

In the simplest case, a VLC channel consists only of a single light source for transmitting data via modulated light and a single photodetector for receiving the light. This case will be dealt with in detail for the free-space and indoor scenarios in the next section. Afterwards, it will be extended to multiple light sources and also multiple receivers in order to form a multiple-input multiple-output (MIMO) system with multiuser support, and different kinds

[1] In some cases, when the signal is minimum phase, the phase can be recovered with a Kramers-Kronig receiver even in IM/DD systems [CA+18].

of interference including multicell interference will be discussed. The novel LCD interference suppression filter is presented and included in the introduced channel model, but the main principle and characterization will be given later in Chapter 4.2.

2.1 SISO Channel Models

The free-space VLC model is depicted in Fig. 2.1 as block diagram. Input data symbols $x[k]$ with k as symbol index are used to generate an analog transmit signal $s(t)$. As there is only one light source and one photodetector, this is a single-input single-output (SISO) channel. A driver circuit generates the LED driving current $i_{\mathrm{f,LED}}(t)$ which must be real-valued and non-negative as demanded for an IM/DD system. The fulfillment of these constraints can be achieved by the modulator or by the amplifier, depending on the applied modulation scheme and the type of driver. The LED emits intensity-modulated light, approximately proportional to $i_{\mathrm{f,LED}}(t)$ into free space[2]. At the receiver side, the photodetector detects the light and generates a photocurrent $i_{\mathrm{PD}}(t)$, which is proportional to the intensity of the received light P_{r}.

The photocurrent is usually very weak, consequently an amplifier is needed. A typical amplifier deployed with photodetectors is a trans-impedance amplifier (TIA), which converts the photocurrent into a proportional, amplified output voltage for demodulation.

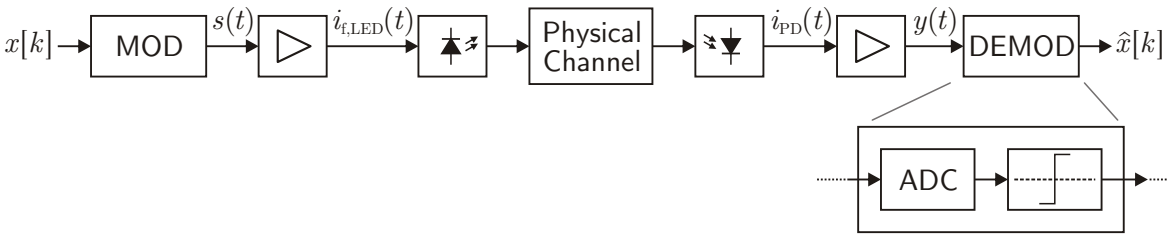

Figure 2.1: Generic block diagram of a VLC system. The modulator (MOD) can be a digital-to-analog converter (DAC) in the simplest case. In the bottom part, a basic realization of the demodulator (DEMOD) is suggested: a sampling analog-to-digital converter (ADC) together with a threshold detector is used to recover the data symbols.

The channel itself can then be described as

$$y(t) = h_0(t) * s(t) + n(t), \tag{2.1}$$

[2]The conditions of this assumption are discussed in Chapter 6.1.

where the receive signal $y(t)$ is given by a convolution between the channel impulse response $h_0(t)$ and the data signal $s(t)$ plus noise $n(t)$. This means that $y(t)$ corresponds to the photocurrent $i_{\mathrm{PD}}(t)$ with noise impact and is therefore also approximately proportional to the optical received power.

The channel impulse response $h_0(t)$ includes all physical effects caused by the LED, the free-space loss, filters, concentrators and also the responsivity of the photodetector. The noise term $n(t)$ represents the sum of all noise sources and is assumed as white. When time variance and the delay caused by the channel and intersymbol interference (ISI) are neglected, $h_0(t)$ can be simplified as the channel gain factor h_0. In this case, the convolution resolves in (2.1) into a multiplication. The equivalent time-discrete channel model after sampling is then as follows:

$$y[k] = h_0 \cdot x[k] + n[k]. \tag{2.2}$$

For convenience, the time index is neglected in the following.

Noise Definition The noise definition used in this work is based on [KB97]. Typical noise sources are amplifiers, which cause thermal noise, and the LED and photodetector themselves, which cause shot noise. Shot noise is dependent on the received power P_{r}, while thermal noise is basically dependent on the absolute temperature T and the value of the assumed amplifier feedback resistor R_{f}, which defines the gain factor. The variance σ_n^2 of n is given by

$$\sigma_n^2 = \underbrace{2e_0 R_\lambda P_{\mathrm{r}} B}_{\text{shot noise}} + \underbrace{4k_{\mathrm{B}} T B R_{\mathrm{f}}^{-1}}_{\text{thermal noise}}, \tag{2.3}$$

where e_0 is the elementary charge, R_λ the wavelength-dependent responsivity of the photodetector, B the bandwidth and k_{B} the Boltzmann constant.

2.1.1 Indoor Scenario

Compared to the free-space scenario sketched above, the indoor scenario is a multipath scenario as shown in the modified Fig. 2.2 for the channel itself. Emitted light is reflected on the walls and objects inside the room, resulting in multiple paths with different gains and delays. The reflections can be multihop reflections, meaning that light is reflected multiple times between the walls and objects before reaching the photodetector. A detailed analysis was performed in [BK+93] and a frequency-domain representation is given in [Sch16]. It

should be noted that the impact of the multihop reflections is low compared to single reflections and the direct paths, which is why they will be neglected in further analyses in this dissertation.

The time-discrete channel model in (2.2) can be extended by the reflections:

$$\begin{aligned} y &= h_0 \cdot x + n \\ &= (h_{\mathrm{LOS}} + \sum_i h_i) \cdot x + n, \end{aligned} \tag{2.4}$$

where h_{LOS} is the direct path and h_i the i-th reflected path. The link budgets of the different paths will be discussed in the next section.

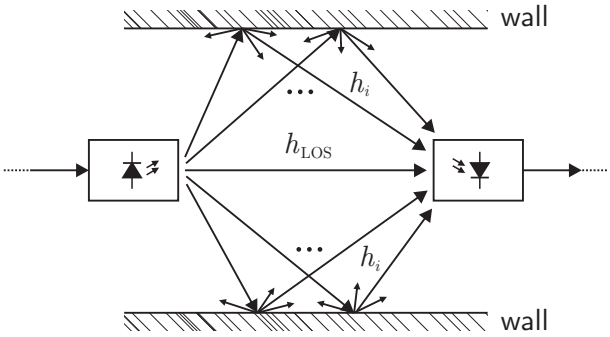

Figure 2.2: VLC indoor channel with diffusely scattered reflections on the walls. The received intensity is a superposition of the mostly dominant line of sight and the individual reflections.

2.1.1.1 Line of Sight

Most of the received light comes via the so-called line of sight (LOS) – if it is not blocked. This is the direct path h_{LOS} between light source and photodetector. It can be calculated with the Lambertian cosine law:

$$h_{\mathrm{LOS}} = P_{\mathrm{Tx}} \cdot \frac{m+1}{2\pi} \cos^m(\vartheta_{\mathrm{out}}) \cdot \frac{A_{\mathrm{PD}}}{d^2} \cos(\theta_{\mathrm{in}}) \cdot g_{\mathrm{PD}} \cdot \kappa \cdot R_\lambda. \tag{2.5}$$

The main parameters of the light source are the transmit power P_{Tx} and the Lambertian mode number m. The mode number defines the directivity – the higher m, the more directive is the light source. The active area of the photodetector is assumed as square and is denoted by $A_{\mathrm{PD}} = a_{\mathrm{PD}}^2$ with its concentrator gain g_{PD} and the edge length of a_{PD}. The concentrator gain is caused by e.g. a lens in front of the photodetector and is directly related to the field-of-view (FOV) φ_{FOV} of the detector, which defines the maximum allowed angle

of incident $\theta_{\text{in}} \leq \varphi_{\text{FOV}}$ for light to be received [KB97]:

$$g_{\text{PD}} = \frac{n_{\text{PD}}^2}{\sin^2(\varphi_{\text{FOV}})}. \tag{2.6}$$

The refraction index of the concentrator lens is denoted by n_{PD}. At the photodetector itself, a pulse-shaping gain κ can be attained because of the optical-to-electric conversion [Sch11; SH22]:

$$\kappa = \frac{\text{E}(i_{\text{PD}}(t)^2)}{\text{E}(i_{\text{PD}}(t))^2}, \tag{2.7}$$

where $\text{E}(\cdot)$ is the expected value. Signals with a high peak-to-average ratio are beneficial regarding this relationship.

It should be noted that the Lambertian cosine law is just an approximation because of the following assumptions: i) the light source is assumed as point source; ii) the distance between light source and photodetector is much greater than the edge length of the photodetector. Otherwise, the area of the photodetector must be expressed as integral in the form of $\iint_A \, dx \, dy$ assuming the detector is oriented in the xy-plane.

2.1.1.2 Diffuse Light

Regarding the multipath propagation, the gain for each path can be calculated similarly to the LOS. As stated previously, only paths of a single reflection will be considered. It is assumed that the walls are split into tiles with an area size of A_{wall} and reflectivity factor δ_λ for calculating the reflections. Then, the gain of a path h_i can be expressed in an approximate way as follows:

$$h_i = \begin{cases} h_{\text{Tx},i} \cdot h_{\text{freespace},i} \cdot h_{\text{wall},i} \cdot h_{i,\text{freespace,PD}} \cdot h_{\text{PD}}, & \text{if } \theta'_{\text{in}} \leq \varphi_{\text{FOV}} \\ 0, & \text{else} \end{cases} \tag{2.8}$$

$$h_{\text{Tx},i} = \frac{m+1}{2\pi} \cos^m(\vartheta'_i) \tag{2.9}$$

$$h_{\text{freespace},i} = \frac{1}{d_{\text{Tx},i}^2} \tag{2.10}$$

$$h_{\text{wall},i} = \delta_\lambda \cdot A_{\text{wall}} \cos(\theta'_{\text{in},i}) \cdot \frac{1}{\pi} \cos(\vartheta'_r) \tag{2.11}$$

$$h_{\text{freespace,PD}} = \frac{1}{d_{i,\text{PD}}^2} \tag{2.12}$$

$$h_{\text{PD}} = A_{\text{PD},r} \cos(\theta'_{\text{in}}) \cdot g_{\text{PD}} \cdot \kappa \cdot R_\lambda. \tag{2.13}$$

2.1.2 LCD Interference Suppression Filter

Now, an additional filter is introduced: an optical filter which is placed in front of the photodiode and which is based on a liquid crystal (LC) display (LCD) with removed backlight as depicted in Fig. 2.3. This filter is an array of single LC cells or pixels, which can be switched to transparent or opaque. The purpose and technology of this type of filter is explained in Chapter 4.2. At this point, only the influence on the channel is of interest. The LCD filter causes a transmission loss $g_{\text{LC,px}} \in [0, 1]$ which depends on the state of the pixels along the optical path and the incident angle θ_{in}. Hence, the total channel factor h is given by

$$h = h_{\text{LOS}} \cdot g_{\text{LC,px}}(\theta_{\text{in}}) + \sum_i h_i \cdot g_{\text{LC,px}}(\theta'_{\text{in}}). \tag{2.14}$$

The overall impact of the LCD filter is now summarized as g_{LC}, so that the channel impulse response can be expressed as

$$h = h_0 \cdot g_{\text{LC}}. \tag{2.15}$$

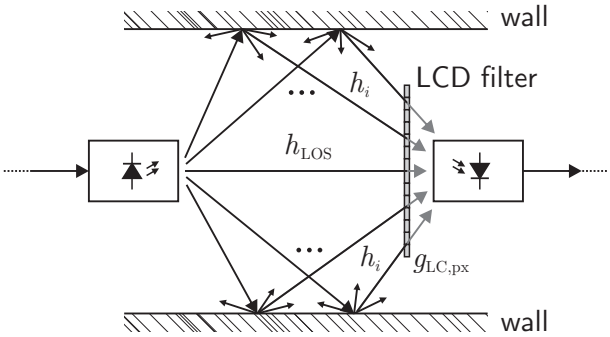

Figure 2.3: LCD filter in front of the photodetector. The line of sight as well as the reflections are weighted with the corresponding pixel loss factor.

2.2 MIMO Channel Models

When more than one transmitter LED and more than one photodetector are deployed, the transmission system can be considered as multiple-input multiple-output (MIMO) system. To model this kind of channel, the SISO channel model in (2.4) is extended: Instead of a single transmission factor h, a matrix $\mathbf{H}$ is used to express the transmission factors between every transmitter LED and every receiver. The number of transmitter LEDs is denoted by N and the number of receivers by K.

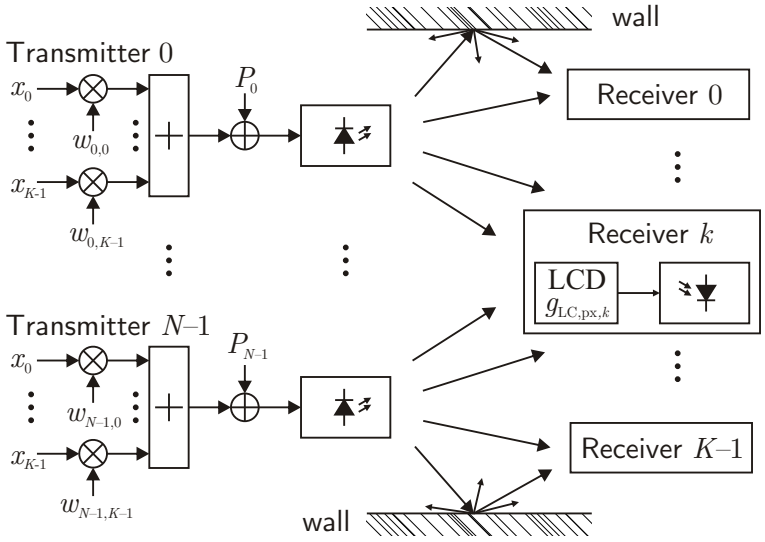

Figure 2.4: Block diagram of a MIMO VLC indoor system. Here, weighting factors $w_{n,k}$ and bias power values P_n are considered.

One matrix element $h_{k,n}$ describes the path between transmitter n and receiver k in a way analog to the SISO case. The channel matrix is given by

$$\begin{aligned}\mathbf{H} &= \mathbf{H}_0 \circ \mathbf{G} \\ &= \begin{bmatrix} h_{0,0} & \cdots & h_{0,N-1} \\ \vdots & \ddots & \vdots \\ h_{K-1,0} & \cdots & h_{K-1,N-1} \end{bmatrix} \end{aligned} \tag{2.16}$$

$$\mathbf{G} = \begin{bmatrix} g_{\mathrm{LC},0,0} & \cdots & g_{\mathrm{LC},0,N-1} \\ \vdots & \ddots & \vdots \\ g_{\mathrm{LC},K-1,0} & \cdots & g_{\mathrm{LC},K-1,N-1} \end{bmatrix}, \tag{2.17}$$

where $\mathbf{G}$ is the filter matrix with its overall LCD gain factors $g_{\mathrm{LC},k,n}$ for the individual

receivers and light sources: The channel gain entries of the original channel matrix H_0 are multiplied element-wise with the corresponding LCD gain. Note that all gains are loss factors here. Additionally, a weighting matrix $\mathbf{W}$ is introduced with

$$\mathbf{W} = \begin{bmatrix} w_{0,0} & \dots & w_{0,K-1} \\ \vdots & \ddots & \vdots \\ w_{N-1,0} & \dots & w_{N-1,K-1} \end{bmatrix}. \tag{2.18}$$

Without loss of generality, the weighting matrix can be assumed to be a scalar weighting factor with $w = 1$ for the SISO case. The channel model can be summarized as follows:

$$\boldsymbol{y} = \mathbf{HW} \cdot \boldsymbol{x} + \boldsymbol{z}, \tag{2.19}$$

where $\boldsymbol{x} = [x_0, \dots, x_{K-1}]^{\mathrm{T}}$ is the transmit data vector, $\boldsymbol{y} = [y_0, \dots, y_{K-1}]^{\mathrm{T}}$ the receive data vector and $\boldsymbol{z}$ is the noise vector.

2.2.1 Massive MIMO Aspects

If N or K are large, the system can be seen as massive MIMO system. Here, the number of transmitters is equal or greater than the number of receivers, so $N \geq K$. Depending on the transmitter LED characteristics and locations, massive MIMO systems are prone to high crosstalk between light of different LEDs.

2.2.2 Multiuser Aspects and Precoding

If more than one user is present in the system, a multiuser aspect has to be considered. For the sake of simplicity, it is assumed here that each user has only one receiver, i.e. the number of users is K. The overall system design can be separated into different levels of user cooperation:

- The users cooperate fully. This means the users can exchange information and decoding schemes can exploit this. Assuming full channel state information, successive interference cancellation (SIC) can be applied, where the information is decoded by subtracting the interference caused by the (known) data of other users.
- The users can only exchange data with direct neighbors. Groups of users can be put together and seen as cluster. Suitable decoding schemes can handle interference inside each cluster by SIC, and also cluster-wise treat the clusters as superusers.

- The users cannot exchange data. Here, the users cannot apply SIC to remove interference. This means that the interference caused by other users is treated as noise. Only at the transmitter side, precoding can be applied to lower the interference, if the transmitter has channel state information.

2.2.3 Interference

In this work, the focus is on the third case, where the users are independent and unable to exchange any data between them. Regarding interference, this case is the most difficult, especially in a massive MIMO system with high channel crosstalk causing inter-channel interference. However, there are also other kinds of interference, namely natural ambient light and light from other non-modulated light sources.

2.2.3.1 Performance Metric

Evaluating the performance in terms of data rates or channel capacity is a delicate topic. The VLC channel is an IM/DD system, which uses incoherent light with certain constraints. Incoherent light cannot have a negative nor complex amplitude, and there is no destructive interference – multiple light sources simply superimpose. Therefore, the well-known Shannon equation (2.20) regarding the analytic channel capacity for additive white Gaussian noise (AWGN) channels cannot be applied here directly [HY$^+$20]

$$C_{\text{Shannon}} = 0.5 \log_2 \left(1 + \frac{S}{N_0}\right). \tag{2.20}$$

The signal power density is given by S and the noise power density by N_0 with variance σ_n^2. For an RF MIMO system, the channel capacity can be achieved by using water filling [Hoe13]. Here, a given total transmit power is distributed over the different subchannels in such a way that each channel has an equal overall power level regarding its individual SNR. Unfortunately, water filling is not the optimal solution for an IM/DD system, as the power distribution problem is of non-convex nature [CR$^+$17; CR$^+$18]. The transmit power cannot be distributed in an arbitrary way to the LEDs since they have a maximum power limit and, to ensure a good illumination quality, usually also an average power constraint.

According to literature [Han22; CT06], an analytic approximation of the channel capacity for unipolar systems, can only be given for low noise variances $\sigma_n^2 \ll 1$ and average amplitude

constraint as:

$$C = \frac{1}{2}\log_2\left(1 + \frac{e}{2\pi\sigma_n^2}\right), \tag{2.21}$$

where the input distribution of data x is assumed as $p_X(x) = \exp(-x)$ for $x \geq 0$, otherwise as zero. To obtain the real capacity, the mutual information between data sink and source needs to be determined for each system individually.

One can calculate several upper and lower bounds, which are valid only under certain more or less restrictive constraints [CR+17; CR+18]. In [FH13], upper bounds for the bit-error rate in spatial modulation (SMOD) and spatial multiplexing (SMUX) settings (cf. Chapter 3.7) with pulse-amplitude modulated (PAM) symbols are presented, which can be calculated as follows:

$$\begin{aligned}\mathrm{BER}_{\mathrm{SMOD}} \leq \frac{1}{MN\log_2(MN)} \sum_{i=0}^{M-1}\sum_{n=0}^{N-1}\sum_{j=0}^{M-1}\sum_{m=0}^{N-1} \mathrm{d_H}(b_{i,n}, b_{j,m}) \cdot \\ \frac{1}{2}\,\mathrm{erfc}\left(\sqrt{\frac{T_s}{8N_0}\sum_{k=0}^{K-1}|I_j h_{k,m} - I_i h_{k,n}|^2}\right),\end{aligned} \tag{2.22}$$

$$\mathrm{BER}_{\mathrm{SMUX}} \leq \frac{1}{M^N\log_2(M^N)} \sum_{i=0}^{M^N-1}\sum_{j=0}^{M^N-1} \mathrm{d_H}(b_i, b_j) \cdot \frac{1}{2}\,\mathrm{erfc}\left(\sqrt{\frac{T_s}{8N_0}||\mathbf{H}(\mathbf{s}_i - \mathbf{s}_j)||_{\mathrm{F}}^2}\right), \tag{2.23}$$

where M denotes the symbol cardinality, $\mathrm{d_H}(\cdot,\cdot)$ the Hamming distance between two bit assignments b_i and b_j of the two symbols $\mathbf{s}_i$ and $\mathbf{s}_j$, $||\cdot||_{\mathrm{F}}$ the Frobenius norm, erfc the complementary error function and I_n the emitted intensity by transmitter n. These bounds are only valid for the mentioned modulation techniques – for other methods, a more general expression is desired. A lower bound for the achievable data rate R for VLC systems with precoding constraints is given in [PK+11; YB+13] as follows:

$$R = \sum_k \log_2\left(1 + \frac{\sqrt{-\log(5\cdot\mathrm{BER})^{-1}}\gamma_k}{\sigma_k}\right), \tag{2.24}$$

where BER is the desired minimum bit error rate, which should be maintained and $\boldsymbol{\gamma} = [\gamma_0, \ldots, \gamma_{K-1}]$ is the power gain vector of the precoding matrix in the form of $\mathbf{W} = \mathbf{C}\,\mathrm{diag}(\boldsymbol{\gamma})$. The matrix $\mathbf{C}$ can be modeled for example as zero-forcing precoding matrix as done in Chapter 4.1.

To be more flexible in system design, a practical and easier performance metric is needed

for evaluating different methods of interference suppression. By looking at the bare light intensities, the signal-to-noise ratio (SNR) is a promising candidate and can be extended to the signal-to-interference-plus-noise ratio (SINR):

$$\mathrm{SNR} = \frac{S}{N_0}, \tag{2.25}$$

$$\mathrm{SINR} = \frac{S}{I + N_0}, \tag{2.26}$$

where I is the interference power density. By assuming that the interference is treated as noise, the SINR is a lower bound and can be applied to every VLC system in a black-box manner. The term "black box" should indicate that if there is no knowledge about the VLC system, one cannot assume that interference is handled in any special way. This corresponds to the third case from Section 2.2.2, where users cannot exchange any data and there is no cooperative interference mitigation. A major drawback of the SNR or SINR metric is that the signal power cannot be measured in isolation when it comes to physical setups – only $S + N$ is measureable as required by the Shannon formula. When the noise power is neglectable, an approximation in the form of the signal-to-interference ratio (SIR) may be more suitable. Here, only the sum of all interference terms is seen as distortion and, if any noise is remaining, it is included in the signal power as well as in the interferer power:

$$\mathrm{SIR} = \frac{S}{I} \approx \frac{S + N_0}{I + N_0}. \tag{2.27}$$

2.2.3.2 Interchannel Interference

A MIMO channel can be separated mathematically into parallel SISO channels by performing e.g. zero-forcing precoding, SIC or QR decomposition. Alternatively, a separation by physical means is possible – for example by using the proposed LCD filter. A more specific explanation of channel separation is given in Chapter 4. The main goal of all mentioned methods is separating the MIMO channel by removing or suppressing interference between the parallel channels.

The interference is caused by crosstalk between the light waves which superimpose at the photodetectors, and consequently resulting in a high cross-correlation between channels. As the assumption states that there is no data exchange between users, the crosstalk is considered as noise. By evaluating $\mathbf{HW}$, the usable signal and interference terms can be derived, and the SINR can be defined in the electrical domain as follows:

$$\mathbf{HW} = \begin{bmatrix} h'_{0,0} & \dots & h'_{0,K-1} \\ \vdots & \ddots & \vdots \\ h'_{K-1,0} & \dots & h'_{K-1,K-1} \end{bmatrix} \tag{2.28}$$

$$\mathrm{SINR}_k = \frac{h'^2_{k,k}}{\left(\sum_{i \neq k} h'_{k,i}\right)^2 + \sigma_k^2}. \tag{2.29}$$

The desired signal can be found on the main diagonal of $\mathbf{HW}$, and the side elements are the remaining interference.

2.2.3.3 Multicell Interference

As, until this point, the channel model takes into account only light sources which can be controlled by the transmission system, the model is now extended to interference caused by other cells. There are options to mitigate also this intercell interference [ML+15; YC+18; PP19], but this increases complexity. In this model it is assumed that only the transmitter light sources in the VLC cell under evaluation can be controlled via the weighting matrix $\mathbf{W}$ and that light sources of neighboring cells are seen as interferers, that is, noise.

Consequently, the matrix of transmission factors by these interferers $\mathbf{H}_\mathrm{I}$ can be defined as follows:

$$\mathbf{H}_\mathrm{I} = \begin{bmatrix} h_{\mathrm{I},0,0} & \dots & h_{\mathrm{I},0,M-1} \\ \vdots & \ddots & \vdots \\ h_{\mathrm{I},K-1,0} & \dots & h_{\mathrm{I},K-1,M-1} \end{bmatrix}, \tag{2.30}$$

where M is the number of interferers. The channel model in (2.19) can be extended by the influence of the neighboring light sources:

$$\boldsymbol{y} = \mathbf{HW}\boldsymbol{d} + \mathbf{H}_\mathrm{I}\mathbf{W}_\mathrm{I}\boldsymbol{d}_\mathrm{I} + \boldsymbol{z}. \tag{2.31}$$

As $\mathbf{W}_\mathrm{I}$ and $\boldsymbol{d}_\mathrm{I}$ are both assumed as unknown, only $\mathbf{H}_\mathrm{I}$ can be considered as worst case. The total inter-cell interference for user k can therefore be expressed as

$$h_{\mathrm{I},k} = \sum_{m=0}^{M-1} h_{\mathrm{I},m,k} \tag{2.32}$$

$$\mathrm{SINR}_{\mathrm{I},k} = \frac{h'^2_{k,k}}{\left(h_{\mathrm{I},k} + \sum_{i \neq k} h'_{k,i}\right)^2 + \sigma_k^2}. \tag{2.33}$$

2.2.3.4 Ambient Light

As ambient light sources are mostly static compared to inter-channel interference, they can be removed quite easily by neglecting the DC part in the electrical domain, but they still increase the noise term through shot noise. So these terms are purely additional and can be modeled by adding a bias to the noise term n in the channel model in (2.4). Removing ambient light in the physical domain requires an adaptation at the receiver front-end. For instance, a shutter or visor can be installed in front of the photodetector, which changes the FOV by decreasing the maximum incident angle. This technique is often used in point-to-point connections with narrow emission beams, where laser transmitters or LED transmitters are employed [PG+12; GP+13].

2.3 Summary

In this chapter, the foundations of the single-input single output VLC channel are derived and investigated. The line of sight is modeled as well as diffuse reflections in an indoor scenario based on the generalized Lambertian emitter model and free-space propagation characteristics. The LCD interference suppression filter is also introduced into the model. Afterwards, this model is extended to a multiple-input multiple-output channel with multiuser access. For doing so, the SISO channel is taken multiple times and the transmission coefficients between them are investigated to form the channel matrix of the MIMO channel. The interference and precoding problems of this specific channel model are discussed for intercell interference as well as multicell interference. Here, additional neighboring transmitter sources are assumed as interferers, which do not belong to the current communication cell as well as other ambient light sources. At last, a suitable metric for the channel performance is requested. Originating from the Shannon capacity formula, several bounds are discussed. Regarding their complexity and limitations, the physical signal-to-interference respectively signal-to-interference-plus-noise ratio is taken because of its general applicability. The SINR is derived for the MIMO scenario as well as the multicell MIMO scenario.

3

Signal Design, Modulation and Coding Schemes

Signals for VLC applications need to comply with the constraints of IM/DD systems and additional illumination requirements. Hence, the modulation schemes known from RF applications cannot be used in an unmodified manner, which is why adaptation is mandatory. The schemes can be divided into groups of waveform complexity like binary modulation, discrete-level modulation, return-to-zero variants and modulation schemes with a nearly arbitrary waveform like orthogonal frequency division multiplexing (OFDM). The more complex the signal waveform, the more complex the modulator and the LED driver. While binary modulation like on-off keying (OOK) is the most simple scheme, using more than two amplitude levels leads to multilevel schemes like pulse amplitude modulation (PAM) or optical code-division multiple access (OCDMA). PAM is the optical variant of amplitude-shift keying (ASK) known from RF applications. Here, different discrete values are used for the transmission of a symbol encoding more than one bit. These kinds of symbols can be generated by a special modulator like the one presented in Chapter 6.2.4 or by using multiple binary modulators simultaneously in order to generate a superimposed multilevel symbol. In the case of more than two levels encoding only one bit per symbol, there are also modulation techniques which employ a neutral level in between – basically a bipolar symbol with a certain bias value. The bias defines the average brightness of the emitted light, and by changing the bias, the brightness changes, too. Modulation schemes of this type are e.g. alternate mark inversion (AMI) and return-to-zero (RZ) variants of binary schemes like OOK. A further extension leads to symbols with an arbitrary waveform which commonly also employs a bias value like some variants of optical orthogonal frequency

division multiplexing (optical OFDM) schemes. In this case, many bits can be encoded in one multicarrier symbol and the average brightness can be set by changing the bias again. When colored LEDs are employed, the color domain can also be used for transmitting data: Either by using the different colors for different data streams or by using color shift keying (CSK) which is mentioned only for the sake of completeness here. A different approach is exploiting the spatial arrangement of the VLC system itself by using spatial multiplexing or spatial modulation. This has some intrinsic advantages compared to regular modulation schemes like the absence of interference.

3.1 Binary Modulation Schemes

Binary modulation schemes are characterized by the fact that they employ only two different amplitude levels: the allowed maximum amplitude and zero level are commonly used for this. Compared to other waveforms, this behavior is hardware-friendly as no complex driver is needed. The amplitude is fixed to two levels, but the switching time can be controlled in a flexible way when e.g. digital output pins on microcontrollers are used for driving an LED. There are several ways to encode data with these limited degrees of freedom. The most simple modulation format is using two different amplitude levels: for encoding "1", the maximum amplitude is used; for encoding "0", the signal amplitude is set to zero for a fixed bit duration. This scheme is commonly known as on-off keying (OOK). For including information for clock recovery, Manchester encoding or other line codes can be applied [19]. It is quite obvious that the average brightness is half of the maximum brightness, equally distributed input data assumed. To change the average brightness, the duty cycle can be adapted (e.g. by changing the pulse length) and the data can be encoded in the position of the pulses. This results in the pulse position modulation (PPM) scheme. Examples of OOK and PPM modulation are shown in Fig. 3.1 a)-b). Another method of adjusting the average brightness is to introduce compensation sequences, which do not bear any data [Hoe19].

3.2 Discrete-Level Modulation Schemes

Compared to binary modulation schemes with only two distinguishable, discrete amplitude levels, there are also modulation techniques, which employ more than two levels but also at discrete levels. These techniques keep the hardware effort still quite small while enabling higher-order data symbols, consequently a better spectral efficiency.

3.2.1 Pulse Amplitude Modulation and Variants

Pulse amplitude modulation (PAM) uses a rectangular pulse as base waveform where the amplitude is varied in discrete steps as shown in Fig. 3.1 d). So PAM-2 corresponds to OOK, while PAM-4 offers four different amplitude levels and can encode two bits per symbol. There are different ways of mapping. Mostly Gray mapping is used, where neighboring symbols only differ in one bit.

3.2.2 Superimposed Intensity Modulation

Another way to create a PAM-like modulated signal is using superimposed intensity modulation (SIM). The resulting multilevel signal is achieved by employing many individual light sources, each of which is modulated with a binary scheme. At the photodetector, the sum of all signals is generated intrinsically by the superimposing phenomenon of incoherent light. In order to create a PAM-4 signal, three different light sources are needed. It is important to ensure that the channel gain of each light source is the same by e.g. placing them next to each other. By doing so, the non-linear impact of LEDs is neglected in contrast to generating different intensity levels with only a single LED, as explained in Chapter 6.2.4. The major drawback of this method is the increased hardware effort, especially with higher-order modulation. This inefficiency exists even in the case of the minimum set of two identical LEDs, as only three distinguishable intensity levels can be created with this configuration.

An extension of SIM, is the constrained SIM (CSIM) presented in [FH18], which increases the hardware-friendly properties of the SIM modulation scheme even more but requires a more complex computation. The switching times of the LEDs are taken into account and so it is ensured that a certain interval of being switched on or off is maintained for each LED until its state changes again. A state diagram is used to keep track of the different LED states and to model the possible transitions depending on the desired switching behavior.

3.3 AMI and Return-to-Zero Variants

As shown experimentally in [KH$^+$20] and in Chapter 6.2.4.1, alternate mark inversion (AMI) and return-to-zero OOK (RZ-OOK) are suitable modulation schemes, but higher-order PAM symbols are suitable, too. For the return-to-zero variants, the "zero" value needs to be biased to half of the maximum amplitude, which means that the bias a_0 is the average amplitude as indicated in Fig. 3.2. To control the brightness in terms of dimming, this bias can be adapted within a certain range. When $x[k] \in \{0, 1\}$ is the data bit to be

transmitted, it is mapped to the symbol $s_{\mathrm{AMI}}[k]$ respectively $s_{\mathrm{RZ\text{-}OOK}}[k]$ as follows:

$$s_{\mathrm{AMI}}[k] = a_0 \pm \begin{cases} 0, & \text{if } x[k] \text{ is zero,} \\ b_+, & \text{if } x[k] \text{ is 1 and } b_- \text{ was chosen last time,} \\ b_-, & \text{if } x[k] \text{ is 1 and } b_+ \text{ was chosen last time,} \end{cases} \tag{3.1}$$

$$s_{\mathrm{RZ\text{-}OOK}}[k] = a_0 \pm \begin{cases} [b_+, 0], & \text{if } x[k] \text{ is 1} \\ [b_-, 0], & \text{if } x[k] \text{ is 0} \end{cases}. \tag{3.2}$$

The values of b_+ and b_- must be chosen in such a way that they cause the same level of change in light intensity to maintain the average bias a_0. A hardware realization of this modulation scheme can be found in Chapter 6.2.4.1.

For e.g. PAM, b_+ and b_- are the appropriate PAM levels with alternating sign.

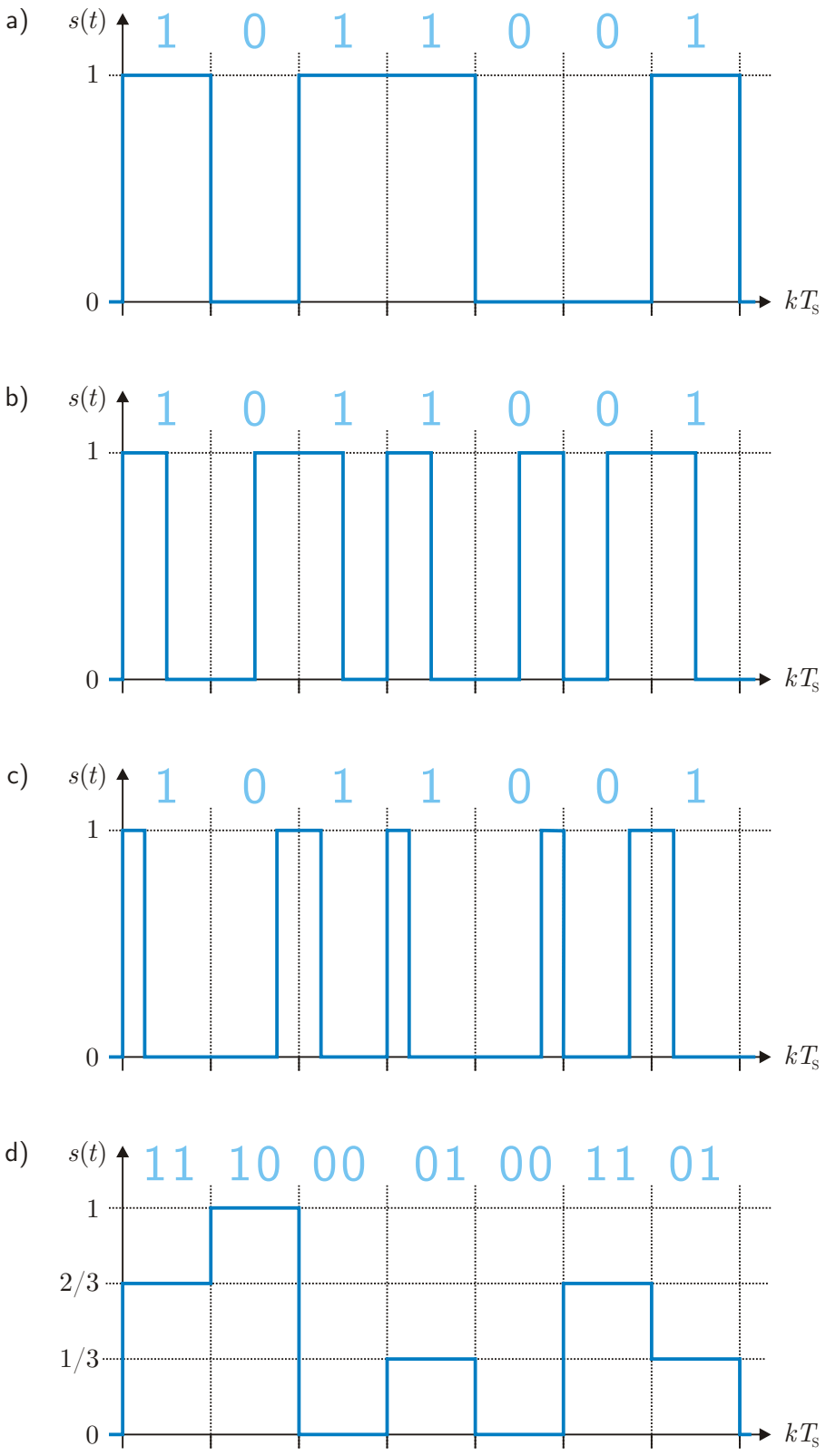

Figure 3.1: Schematic illustration of a) OOK, b) PPM with 50 % duty cycle, c) PPM with 25 % duty cycle and d) PAM-4 with Gray coding.

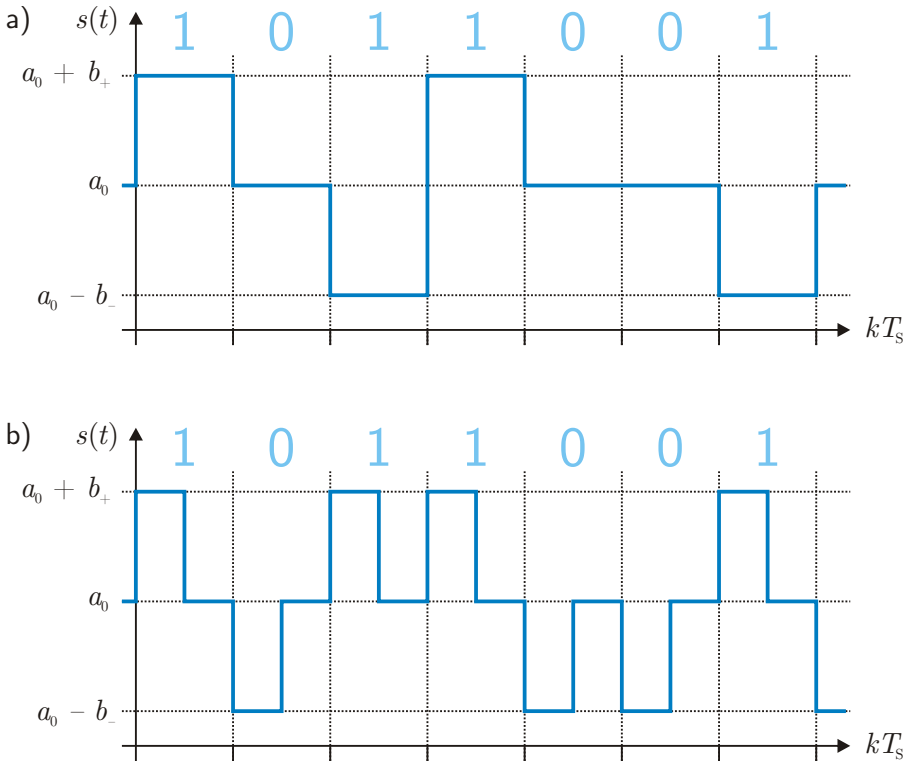

Figure 3.2: Schematic illustration of a) AMI, b) RZ-OOK with 50 % duty cycle.

3.4 Optical OFDM and Variants

Optical orthogonal frequency division multiplexing (optical OFDM) is the adaptation of RF-based OFDM, where the constraints of optical communications are considered. The transmit signal has a nearly arbitrary waveform and also a high peak-to-average ratio (PAPR) compared to the previous schemes. This makes the transmission of these signals quite challenging, which is why not every driver type is suitable. A numerical analysis of a modulated buck converter with optical OFDM can be found in Section 6.2.3.3.

3.4.1 OFDM Fundamentals

In OFDM, the spectrum is split into subchannels and each of which is modulated individually (power and bit loading [Hoe19]). Typically this is done by using an inverse fast Fourier transform (IFFT) as modulator, where, on the input side (frequency domain) the data streams for the subchannels are entered, and, on the output side, a corresponding time-domain signal is gained, as indicated in Fig. 3.3.

3.4.2 Real-Valued and Non-Negative OFDM

To ensure non-negativity and real-valued signals, special precautions are needed. In wire-based electrical transmission systems like digital subscriber lines (DSL), the real-valued output signal is achieved by employing Hermitian symmetry. By doing so, the behavior of the Fourier transform is exploited, so that a real-valued time-domain signal corresponds to a complex-conjugated frequency-domain signal. Consequently, only half of the available spectrum can be used for data transmission. Half of the subcarriers are used for the complex-conjugated data, as shown in the extension in red in Fig. 3.3. By clipping the signal and adding a bias, the non-negativity can be achieved, which results in DC-offset OFDM (DCO-OFDM). There are also other methods for achieving this, like asymmetrical clipped offset OFDM (ACO-OFDM), etc. [Arn15]. The ITU standard G.9991 recommends apart from ACO-OFDM creating complex valued time-domain samples, of which only the real part is transmitted [ITU19].

3.5 Optical CDMA

Another popular modulation technique known from RF is code-division multiple access (CDMA). Orthogonal codes are used to single out a particular data stream among other

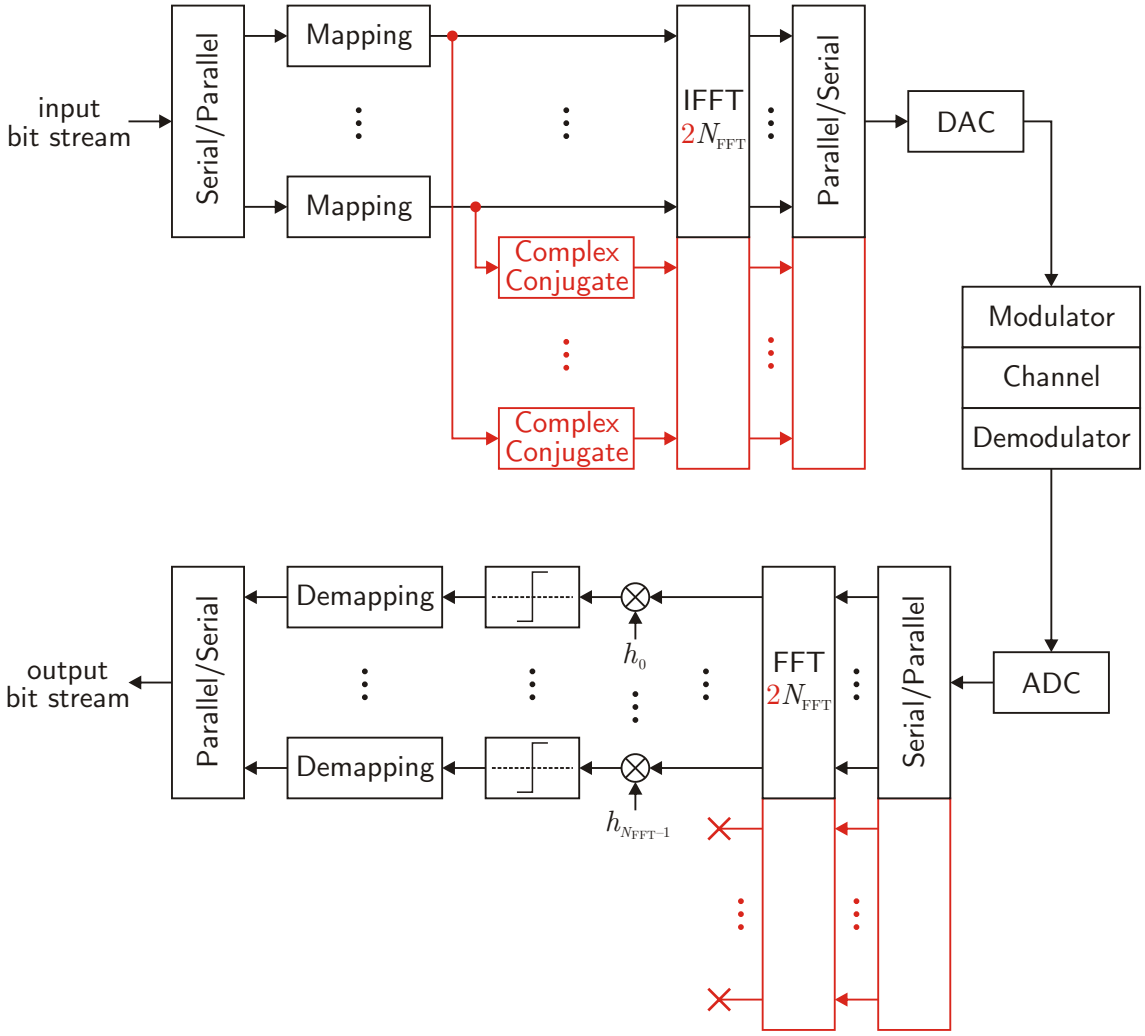

Figure 3.3: Block diagram of an OFDM transmission system and DMT extension in red, based on [Kam04].

parallel ones at the receiver side. For each stream, a unique code, or chip sequence, is used. The orthogonality in RF is achieved by positive and negative amplitude values which cancel out when two different codes are multiplied. As there are no negative amplitudes in VLC, the orthogonality must be achieved by codes that have only positive amplitudes distributed quite sparsely along the zero-gaps in the other codes [CS+89; Hoe19].

3.6 Color Modulation

When differently colored LEDs are used, the color space can also be exploited for data transmission. Each color can be modulated individually by a separate data stream, or the

available colors can be used for forming a data symbol in terms of color shift keying (CSK). In either case, neither the average color perceived by the naked eye nor the brightness level should change. At the receiver side, a color sensitive receptor is needed in order to distinguish between different color intensities. This can be e.g. multiple photodetectors with color filters, or a camera-based receiver as described in Chapter 4.3.1. An experimental setup and characterization is presented in [KH+18b].

3.7 Spatial Encoding

In addition to the time or frequency domain, the spatial domain can also be used to encode data in order to increase the robustness or throughput [FH13]. In spatial multiplexing (SMUX), the user data is modulated and spread equally over all available light sources. In contrast, spatial modulation (SMOD) uses only part of the user data to form the modulated transmit signal and utilizes the remaining data to determine a specific individual light sources or group of light sources which will transmit the before-generated modulated signal. This means that the selection of the chosen transmitter bears also user data and that interference between light from different sources is completely avoided. The robustness depends highly on the channel conditions, i.e. all lines of sight must be present in order to be able to detect modulated light from all light sources. This problem increases with growing spatial dimensions which should be exploited: when the light sources are located far away from each other, they can be easily distinguished – when visible – with a suitable receiver. However, when they are close to each other, their positions, and therefore their signals, become more and more correlated. Consequently, a separation is more challenging. Expressions for the bit-error rate are given in (2.22) and (2.23) in Section 2.2.3.1. The proposed receiver type in Chapter 4.2 is suited to decode spatial multiplexed signals as it can separate light sources in the physical domain as shown by the numerical simulation results in Section 5.2.1.

3.8 Summary

In this chapter, modulation formats for VLC applications are discussed. The available degrees of freedom for modulating incoherent, visible light are taken into account and suitable modulation techniques are introduced. Starting with binary schemes with one bit per symbol, on-off keying is introduced together with pulse-position modulation. The range of applicable methods is then extended in terms of amplitude and hardware complexity.

Pulse-amplitude modulation, the optical variant of amplitude-shift keying, is discussed and how it can be realized with multiple LEDs. As extension to these fixed-amplitude schemes, alternate mark inversion and return-to-zero OOK are introduced, where the average brightness is adjusted via a bias value as neutral level. Next, multicarrier schemes are introduced briefly and the basics of optical orthogonal frequency division multiplexing are presented. Subsequently, the requirements of code-division multiple access in the optical domain conclude the range of RF-adapted schemes. Finally, color-shift keying and spatial encoding are discussed. For all presented modulation schemes, focus is also drawn on the hardware complexity when realizing them as LED modulator or driver circuits.

Part II

Methodology

4

Interference Suppression Methods and Filters

In a multiuser MIMO VLC system, the interference between light emitted by different transmitters and different users is quite challenging. Usually, the light is of the same color and its intensity adds up at the photodetectors. Additionally, when the light serves also for illumination purposes, the single distribution of each light source overlaps with neighboring ones in most cases since an even level of light is desired. A separation at a single point in space for a single user with one receiver is therefore not easily achievable.There are different approaches to this problem: One could use an algorithmic scheme, where the intensity of interfering light is simply turned down. This works quite well when there are not many nearby users and sufficient less-correlated light sources. However, when the overall light intensity is lowered, signal recovery might be harder at the receiver side. Pushing this to the limit leads to zero-forcing (ZF) precoding, where the channel matrix gets inverted in order to suppress interference. Due to the mentioned limitations, the performance might suffer in harsher settings.

But the main idea – adaptation of the channel weights – can be transferred to a different, hardware-based approach. Instead of regulating the transmit power, the physical channel itself can be altered by using a physical object which is placed in the paths of light between light sources and photodetectors. This way, the physical path loss is modified while the transmit power remains unaltered. This dissertation presents some feasible ways to achieve this and explores novel active blocking and passive blocking technologies. For completeness, existing methods like imaging or mirror-based techniques are also mentioned.

4.1 Algorithmic Approaches

As mentioned in Chapter 3.7, some modulation schemes inherently avoid interference between light from different transmitter sources at the cost of available channels or usable lamps. To be more independent of the modulation format and to obtain a better channel usage, the influence of the channel – the cause for interference – can be suppressed by mathematical operations. The most basic approach is using the inversion of the channel matrix in (2.19) as precoding matrix. The overall result will be an identity matrix, so that no interference remains:

$$\begin{aligned}\mathbf{y} &= \mathbf{H}_0\mathbf{W}\boldsymbol{x} + \boldsymbol{z} \\ &= \mathbf{H}_0\mathbf{H}_0^{-1}\boldsymbol{x} + \boldsymbol{z} = \mathbf{I}\boldsymbol{x} + \boldsymbol{z}.\end{aligned} \tag{4.1}$$

If the channel matrix cannot be inverted, the pseudo inverse $\mathbf{H}_0^T(\mathbf{H}_0\mathbf{H}_0^T)^{-1}$ is used instead. This is the optimum solution when no constraints are present. Unfortunately, in an IM/DD system like in VLC, there are some very important constraints: The individual light sources have an upper power limit, there are only positive amplitudes, and no constructive or destructive interference can be exploited because of the non-coherent nature of regular light sources.

In RF-based communication systems, the optimum solution to this problem is to apply waterfilling. Here, the available transmit power is "poured" over the noise floor and by doing so, good channels with less noise gets more signal power while distorted channels get less [CT06]. This optimization problem manifests itself as a non-convex problem when the solution for IM/DD systems is desired [CR+17; CR+18]. So, a quick and optimal solution is not easily achieved. By introducing constraints like an average or peak power limit, the problem can be simplified and with approximating algorithms, a power distribution can be calculated. This difficulty can even be transformed into a convex problem like in [PK+11; YB+13], so that a solution can be achieved with a conventional optimizer approach. By doing so, the precoding matrix is extended by a diagonal matrix composed of the power vector $\boldsymbol{\gamma}$ as described in Chapter 2.2.3.1:

$$\begin{aligned}\mathbf{y} &= \mathbf{H}_0\mathbf{W}\boldsymbol{x} + \boldsymbol{z} \\ &= \mathbf{H}_0[\mathbf{H}_0^T(\mathbf{H}_0\mathbf{H}_0^T)^{-1}\mathrm{diag}(\boldsymbol{\gamma})]\boldsymbol{x} + \boldsymbol{z}.\end{aligned} \tag{4.2}$$

The power vector $\boldsymbol{\gamma}$ can be calculated by solving this optimization problem given the

expression for the achievable rate R in (2.24):

$$R = \sum_k \log_2 \left(1 + \frac{\sqrt{-\log(5 \cdot \mathrm{BER})^{-1}}\gamma_k}{\sigma_k} \right),$$

$$\begin{aligned} \max_{\boldsymbol{\gamma}} \quad & R \\ \text{s.t.} \quad & \mathrm{abs}(\mathbf{H}^T(\mathbf{H}\mathbf{H}^T)^{-1})\boldsymbol{\gamma} \leq \mathbf{p}, \end{aligned} \tag{4.3}$$

where $\mathbf{p}$ is the power constraint vector, and BER the bit-error rate limit. ZF precoding can be applied to a multiuser scenario, where the users are within one cell but also to a multiuser multicell scenario. In this case, ZF precoding eliminates the interference inside a cell and also, in a separate step, the interference between multiple neighboring cells [PP19].

There are adaptations of ZF precoding like zero-forcing "dirty paper coding" (ZF-DPC) or QR channel decomposition [YB+13; CR+18; Par80]. Here, some actions are required additionally at the receiver side. A full receiver-side scheme would be successive interference cancellation where a user decodes the different data streams successively. By decoding the strongest stream, the interference caused by the former can be subtracted from the overall sum signal, so that the next stream can be decoded.

In a multiuser scenario, this means that every receiver needs to decode all streams by itself or a cooperating structure is required. Both variants demand additional effort when only one data stream is of interest.

4.2 Active Optical Suppression

A different approach is removing the interference in a physical way by altering the path of the light rays directly instead of employing a purely algorithmic method. Thus, crosstalk between light from different sources and users can be prevented in advance. As altering the physical setting also impacts the illumination characteristics when done at the light source itself, the most convenient way is to do this at the receiver side. An adaptive filter is mounted in front of the photodetector in order to cast specific shadows. Light from unwanted sources should not reach the photodetector any longer, while light from desired sources should be able to pass. The principle is illustrated in Fig. 4.1: The available transmitter light sources are assigned to the present users and each user configures their individual LC filter in such a way that only the desired light can reach the photodetector – influences by other transmitters or by any other light sources are blocked. Assuming a far-field scenario, the shape and area of the photodetector can be projected onto the LC

plane for each assigned light source in good approximation. Similar to software-defined radio in RF applications, the characteristics of the LC interference suppression filter are configured only by software without the need of changing the physical setup in any way. This method is discussed in more detail in the next chapter.

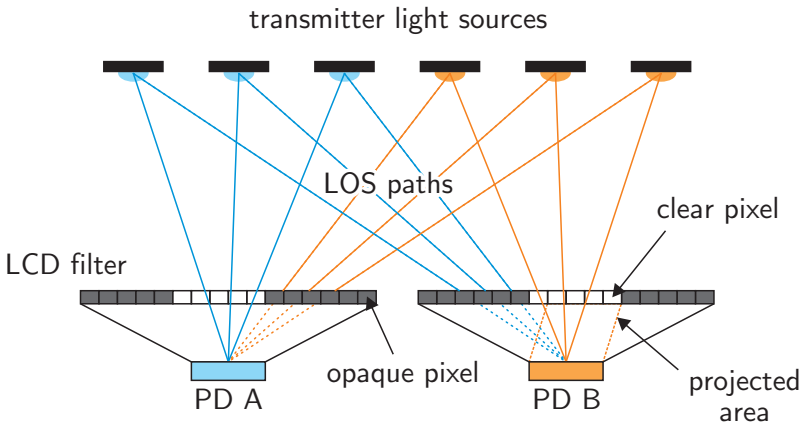

Figure 4.1: Active receiver-side optical suppression.

A suitable technology for this adaptive filter is a liquid crystal (LC) matrix as used in an LC display (LCD) with removed backlight. The display itself can be set in terms of individual pixels that can be switched between transparent and opaque. This way, a pixel-wise setting of the filter can be achieved by forming an adaptive aperture for the photodetector. In this case, the precoding matrix $\mathbf{W}$ is a binary matrix where the assignments of the light sources to their corresponding users are stored. For the generation of these assignments, given the system draft in Fig. 4.2, the structure of a possible VLC system model is presented: The users localize the transmitter light sources and measure the intensity received from each one. Assuming a given uplink, this information is uploaded to a central processor, which generates the channel matrix from the user data. Afterwards, the central processor assigns the transmitter lights to the users in such a way that the signal-to-interference ratio (SIR) is maximized. This can be the overall SIR or the occurring minimum SIR of a specific user. The allocation information is distributed to the users, e.g. with a scheme, which does not need interference cancellation like time-division multiple access (TDMA). The users configure their LCD filters based on the allocation, and then the transmission of individual data streams can start. Instead of the illustrated star topology for the transmitter LEDs, the central computer could also use a bus topology for controlling the LEDs. Doing so requires less cabling effort but reduces the maximum transmission rate, if each LED should transmit individual data as they all share the same supply bus.

In more detail:

1. All users switch their LCD filter to transparent.
2. The central processor switches on all available light sources, so that the users can locate the light sources and measure the channel gain factors.
3. The users transmit their channel gain vector via an uplink channel back to the central processor.
4. The central processor merges all channel gain vectors to a single channel matrix and allocates the light sources to the users in such a way that the SINR is maximized.
5. The central processor broadcasts the allocation scheme to all users.
6. The users configure their LCD filter in such a way that they can only see the assigned light sources.
7. The central processor starts transmission of individual data streams.

One should note that a calculated allocation scheme is only valid for specific, fixed positions of users. If the users change their position or orientation, the channel gain factors and incident angles will also change. By allowing a less strict interference suppression pattern on the LCD filters, this situation can be eased, but with the cost of not so effective interference mitigation in most circumstances.

4.2.1 Aperture Areas and Patterns

At first, the light sources are treated as Lambertian point sources which are located far away in relation to the distance between LCD and photodetector inside the receiver. With this assumption, the incident light rays can be seen as parallel, which means that the area of the photodetector is also a parallel projection along the direction of rays onto the LCD plane. Thus, the aperture size and form should be the same as the photosensitive area of the photodetector. As a result, the FOV is narrowed in such a way that only light from the light source, whose rays are parallel to the projection direction, can reach the detector. If a smaller aperture is chosen, the photodetector is not fully illuminated; and if the aperture is chosen larger, undesired light coming from other sources can reach the detector. When the LCD filter is used for estimating the direction of arrival of light of one of the light sources, this is also the optimum size as presented in [HK$^+$22]. Here, either the aperture is moved

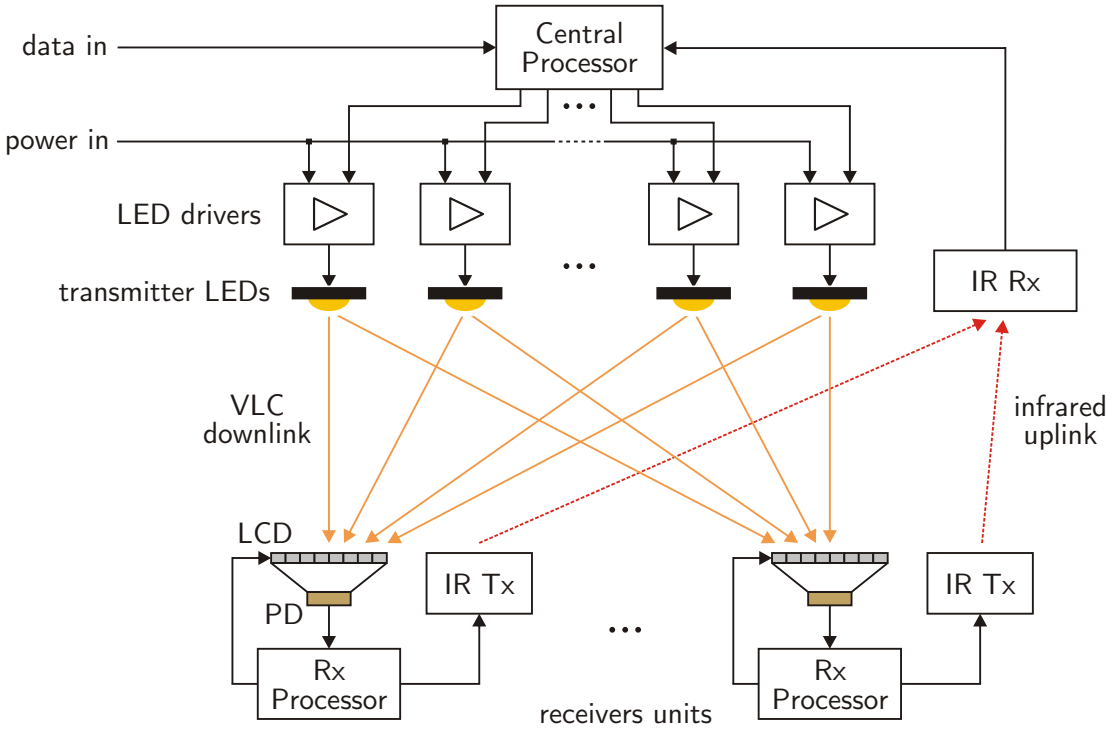

Figure 4.2: Draft for a system design.

pixel-wise in order to find the light source, or bars with the width of the photodetector edge length are moved along the x- and y-axis in the case of the bar search algorithm published in the before-mentioned paper [HK+22]. In both cases, the result is a convolution-like behavior where the highest accuracy in form of a triangle output signal is achieved when the sizes are equal.

By rotating or tilting the receiver, so that the surface normal is not aligned to the z-axis any more, this relation still holds as the photodetector and the LCD filter are connected in a fixed way. For spatially extended light sources, this analysis must be done individually based on the exact dimension and shape of the light source. In this case, the projection of the light source shape onto the photodetector plane can be done and, depending on the actual requirements like full illumination of the detector or keeping the FOV at a minimum, the resulting aperture shape can be derived.

Assuming ideal transmittance factors, ambient light without any specific origin direction is attenuated by the percentage of pixels in blocking mode, i.e. the ratio between pixels in blocking mode and the total number of pixels.

4.2.2 Separating Power of the LCD Filter

The masking of the undesired light sources by applying the mentioned scheme works only well, if the light sources are located far away so that the projected areas are not overlapping. If two neighboring lights are too close, parts of the neighbor can also reach the detector when one of them is selected with the detector-sized aperture. Consequently, when full illumination is desired, there is a lower bound for the light source distances and also for the separating power of the LCD filter. For practical reasons, a distance of one pixel between the projections should be kept on the LCD plane. The minimum distance $d_{\min}$ of two light sources at a height of d_z can be calculated for the point source model via the required minimum angle difference $\Delta\theta_{\min}$ as indicated in Fig. 4.3 a):

$$\Delta\theta_{\min} = \theta_2 - \theta_1 = \arctan\left(\frac{d_1 + a_{\mathrm{px}} + a_{\mathrm{PD}}}{h}\right) - \arctan\left(\frac{d_1}{h}\right) \tag{4.4}$$

$$\Rightarrow \Delta\theta_{\min}(\theta_1) = \arctan\left(\tan(\theta_1) + \frac{a_{\mathrm{px}} + a_{\mathrm{PD}}}{h}\right) - \arctan(\tan(\theta_1)) \tag{4.5}$$

$$\text{with } \frac{d_1}{h} = \tan(\theta_1)$$

$$d_{\min} = d_z\left(\tan(\theta_2) - \tan(\theta_1)\right) \tag{4.6}$$

It should be noted that the perceived pixel size is cosine-dependent as the LCD is planar.

When full illumination of the detector is less important than the suppression of other light sources, the minimum distance can be reduced by making the aperture smaller. A convenient method to do so is the following: first, the apertures are created as described above for the desired light; then, for all other (unwanted) light sources, an additional aperture is created, but all affected pixels are set to blocking mode. Pixels in pass mode are overwritten by the blocking mode pixels resulting in a new overall aperture. This can, of course, lead to a receive signal of zero, if two rival light sources are located directly next to each other. Depending on the system settings and components, there is a break-even point for the optimum aperture where the SINR is maximized.

4.2.3 Allocation Schemes

The following section is based on publication [KH+22].

With ZF precoding, the weighting matrix $\mathbf{W}$ consists of floating point values, which are derived by some channel inversion optimization. The signal for each light source is the sum of different fractions of the individual user data, which is why a driver is needed that can handle arbitrary signal waveforms.

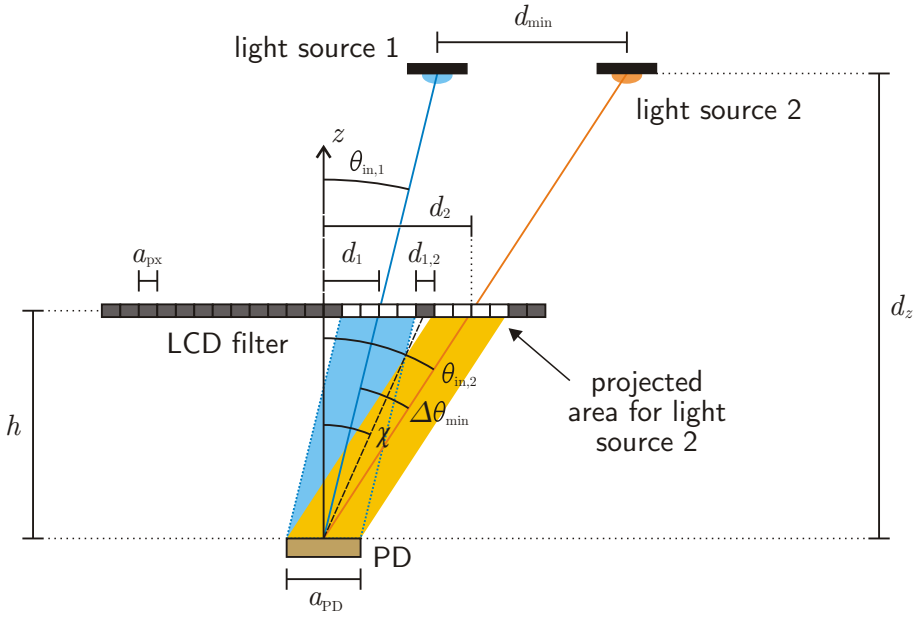

Figure 4.3: Separation capabilities of LCD filter, based on [KH+22].

A simpler approach is using a binary weighting, where data signals are either transmitted by a light source or not. Hence, a less complex driver is needed, especially when binary modulation schemes are deployed since the signal waveform features only discrete amplitude levels. To reduce the complexity further, one can assign a single data stream only to a single light source, that is, assigning the light source to a specific user. This results in a weighting matrix with only a single "1" in each row.

The assignment is a crucial step towards system performance. The interference between users should be kept as low as possible – analog to ZF precoding. In order to derive a formulation of a suitable optimization problem, the following constraints are assumed:

- Each transmitter can be assigned only to a single receiver.
- Each transmitter must be assigned to a receiver.
- The assignment factor between LED n and receiver k can only be "1" or "0".
- Each user is only equipped with one receiver with a single PD.

With ideal interference suppression, the filter matrix $\mathbf{G}$ is the transpose of the resulting weighting matrix $\mathbf{W}$. This matrix is called the allocation matrix $\mathbf{G}_{\text{opt}} = \mathbf{W}^T$ with the assignment factors $g_{\text{opt},k,n}$ as matrix elements:

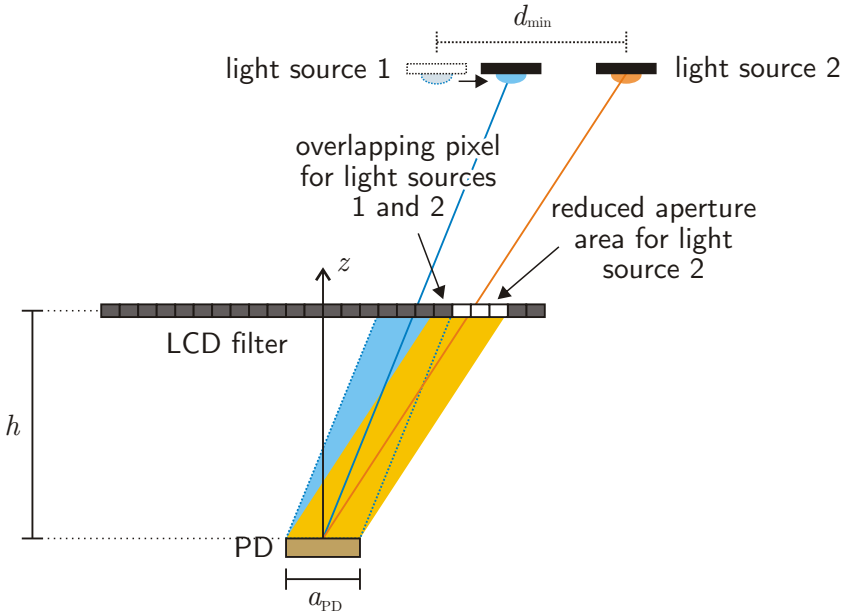

Figure 4.4: Reduced aperture size when the distance between light sources to be separated is smaller than $d_{\min}$.

$$\mathbf{G}_{\mathrm{opt}} = \begin{bmatrix} g_{\mathrm{opt},0,0} & \cdots & g_{\mathrm{opt},0,N-1} \\ \vdots & \ddots & \vdots \\ g_{\mathrm{opt},K-1,0} & \cdots & g_{\mathrm{opt},K-1,N-1} \end{bmatrix}, \tag{4.7}$$

where – given the constraints – only a single "1" is allowed in each column.

The assignment should be done in a way that the minimum SINR of the users is maximized and a suitable interference suppression scheme should aim to set the filter matrix $\mathbf{G}$ as close as possible to the allocation matrix $\mathbf{G}_{\mathrm{opt}}$. The better this task is fulfilled, the more closely the resulting minimum SINR approaches the theoretical one.

The optimization problem can be condensed to the question of how to allocate the light sources to the users. Therefore, the presented problem can be modeled as "Santa Claus problem on unrelated parallel machines", known from computer science [BS06; JM17]. Different approaches are suitable for solving these kinds of problems. In this dissertation, a deterministic approach is developed, and a genetic evolutionary process is taken.

4.2.3.1 Santa Claus Problem Modeling

The Santa Claus problem on unrelated parallel machines (SC-UPM) is a scheduling problem of assigning different tasks to unrelated parallel machines. This means that the machines are not related or influenced by each other and that every task causes a different workload on each machine. The main purpose is to distribute the tasks in such a way that the workload of the machine with the least load is maximized. The name of the problem is based on the analogy with Santa Claus, who gives presents to children. Each present has a different happiness value for the individual child and the goal of Santa Claus is to distribute the presents in such a way that the happiness of the unhappiest child is maximized. Consequently, an equally distributed happiness is inherently aimed for.

Applied to the above-mentioned allocation problem of light sources and users, the K users are the children and the N transmitter lights are the presents. The happiness values are the channel coefficients $h_{k,n}$, which are given by channel matrix $\mathbf{H}$. This means that the allocation problem is modeled as SC-UPM, a user fairness criterion is already considered. The desired maximization of the minimum SINR is yielded from the allocation in an indirect way as the target value for SC-UPM is the combined channel gain.

An optimal solution cannot be computed in a reasonable time due to the fact that the SC-UPM problem is NP-hard [BS06]. In [JM17; FG$^+$22], approximating and exact algorithms are presented, however, they still take long processing times which make the proposed solutions not suited for a VLC system.

4.2.3.2 Heuristic Optimization

To solve the SC-UPM problem, a heuristic approach is presented here. For this reason, the well-known longest-processing time (LPT) algorithm [GI$^+$77; Lee91; CV97] is modified. The LPT algorithm minimizes the longest processing time of all machines in its original design, where all tasks have also equal running time on each machine. The LPT algorithm offers a fast and good approximated solution to this problem and is therefore the basis of a modified variant for the related SC-UPM problem, which is introduced as LPT-SC-UPM in this dissertation and presented as 1 in Appendix B.

The basic idea is to iterate over the N light sources. In each iteration, the receiver with the lowest sum of allocated signal power is selected. Then, the light source, which provides the highest channel gain and which is not already taken, is assigned to the receiver. As in the beginning, the assigned sum power of each user is zero, a prioritization is calculated in advance. Based on the original channel matrix $\mathbf{H}_0$, all users who have zero-valued entries

are collected. The one with the most zeros is handled first in the start round and its priority is reduced by 1. In the next round, the user who now has the top priority is selected and processed in the same way. This procedure is repeated until all priorities are reduced to zero and the regular allocation in terms of the SC-UPM problem begins. Doing this priority handling beforehand increases user fairness as it may happen that a specific user has only a single LOS by a single light source available, which could get assigned to a different user in a previous step. This would lead to an undesired minimum SINR of zero.

4.2.3.3 Genetic Evolution Optimization

The following section is based on publication [KP+22].

The principle of genetic evolution, as depicted in Fig. 4.5, can be applied to many different kinds of optimization problems. Instead of using a deterministic algorithm for solving the problem, randomly initialized solution candidates – so-called individuals – are generated to form a pool – the so-called population. Each individual delivers a result – the so-called fitness – when applied to the problem and the individuals with the best results are picked and combined in order to form the new generation of offspring individuals. The fitness value of each individual is evaluated, so that the selection process is done in a survival-of-the-fittest manner. After a predefined number of generations, the evolution process is stopped and the fittest surviving individual represents the best solution for solving the problem.

An individual could be an allocation set for the SC-UPM problem or e.g. directly a pixel pattern for the LCD filter depending on the VLC system.

4.2.3.3.1 Fitness Evaluation The performance of a VLC system can be used as fitness value. This could be the SINR value, an achieved data rate or channel capacity expressions. For every individual in the population, the fitness value is determined and stored. Next, a tournament selection is used to obtain the best individuals. The tournament randomly chooses a fixed number – the tournament size – of individuals from the current population and selects the one with the highest fitness value. For creation of the next generation, this process is repeated until the required number of individuals has been reached.

4.2.3.3.2 Combining Individuals For the creation of two child individuals, two parent individuals are needed. There are many different ways to combine two individuals, but only the two-point crossover method is discussed here. Assuming an individual is represented by a vector or a list, all individuals in the population are combined with a given probability. As

shown in Fig. 4.6, by selecting two random index points of the parent vector/list entries, the two offspring vectors/lists are created by taking the slices of the parent vectors in an alternating manner: The first part of parent A is given to child A, the second part of parent B is given to child A and finally the third part of parent A is given to child A. For child B the order is inverted: the first part of parent B, the second part of parent A and the third part of parent B are combined. Then the new individuals are mutated, i.e. the entries of the vector/list are bit-flipped or exchanged with a random number with a given probability.

4.2.3.3.3 Solving the SC-UPM Problem with Genetic Evolution To apply genetic evolution optimization to the SC-UPM, the individual type as well as the fitness function must be defined. Compared to the LPT-SC-UPM algorithm, which derives an allocation set, an individual is a randomly defined set. Considering the constraints in Chapter 4.2.3, a suitable representation of an individual is a vector of length N, the number of available light sources. The entries of the vectors are chosen from the set $0, \ldots, K-1$, representing the assigned user for each lamp. Then, the resulting minimum SINR can be determined and used as fitness value for this specific allocation set.

When the LCD pattern should be optimized pixel-wise in a direct way, an individual can be modeled as vector of the length of all available pixels over all users. For evaluation, this large vector is split up in parts for the individual LCDs and reshaped in matrix form whose entries represent the pixel states – either "0" or "1".

4.2.3.4 Iterative Combining of Approaches

A different approach for modeling the allocation problem is combining the LCD filter with ZF precoding. In an iterative manner, the LCDs are optimized by genetic evolution as described in the previous paragraph, and then ZF precoding is used to calculate the optimal weighting matrix $\mathbf{W}$ and the resulting sum rate or minimum SINR. The idea is that the optimization of the LCD pattern directly supports ZF precoding by delivering a less correlated channel.

The main advantage of doing this is that all interference components are considered instead of only taking into account the LOS. If diffuse reflections are the main contributors to the interference, the genetic optimization tries to find the optimum pixel-wise pattern in order to suppress the interference. This, however, comes at a rather large cost as in each iteration and for each individual the channel matrix has to be determined individually.

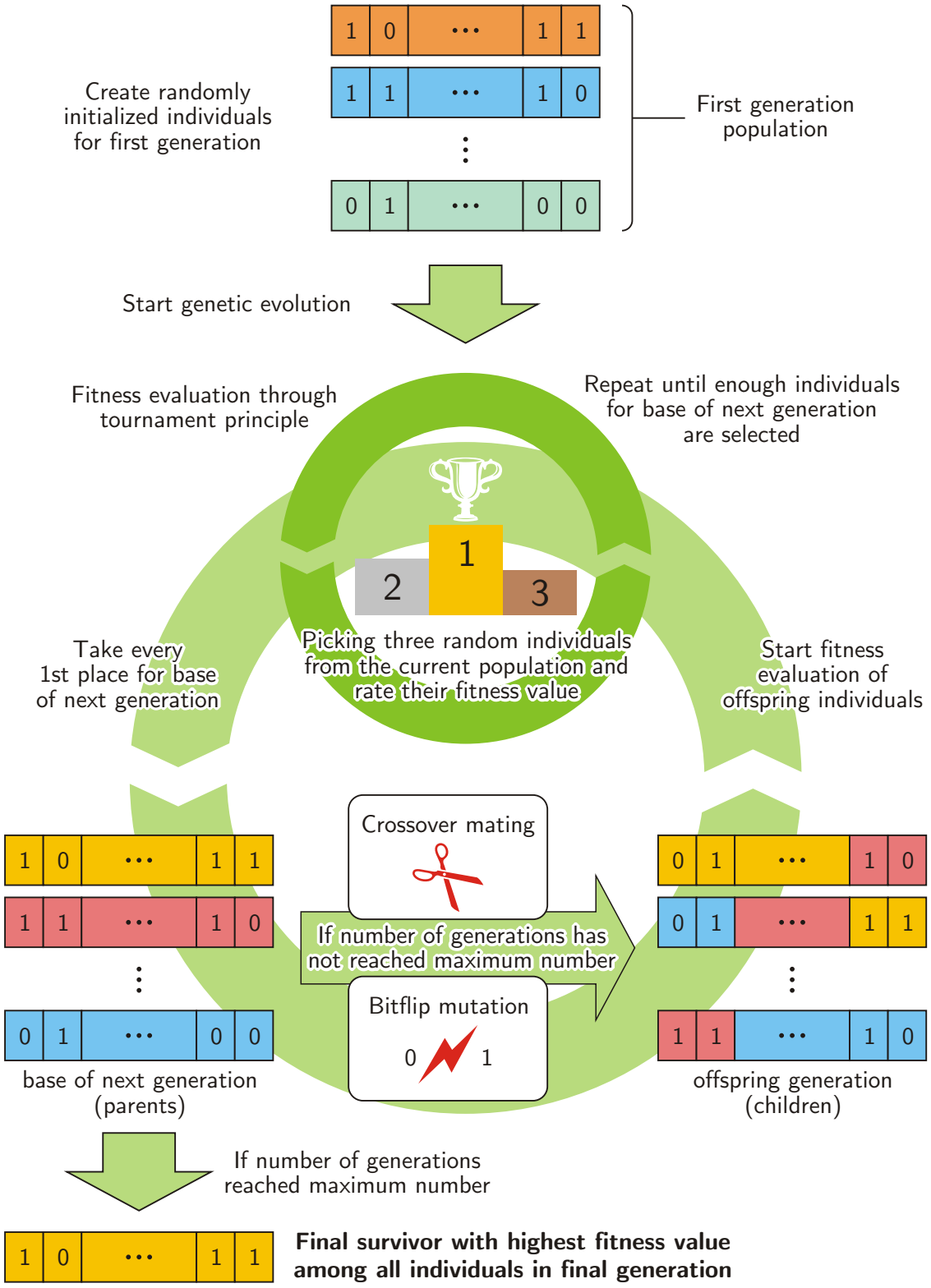

Figure 4.5: Principle of genetic evolutionary optimization.

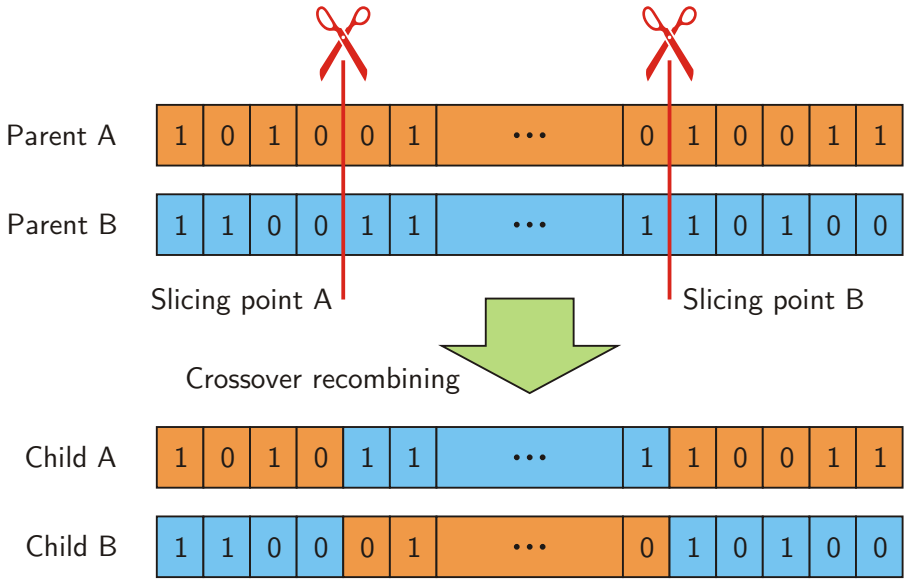

Figure 4.6: Combining two individuals with two-point crossover method.

4.3 Passive Optical Suppression

The following section is based on publication [KF+17].

For receivers with multiple photodetectors, a passive filter might also be suitable. Here, a physical structure is used in order to separate the light sources. This structure should ensure that the light sources, which are receptable by one photodetector, are not seen by others. The physical structure can be of different types, e.g. a pyramid-like receptor [NH+15] or a mirror-based one [PO+17].

Another possibility is using an alternating spherical structure, which is placed over each photodetector, as shown in Fig. 4.7. The slotted sphere blocks half of the FOV of one photodetector, while exactly the other portion of the FOV is blocked in the counterpart. This enables a division of the light sources into two groups. Additionally, this principle can be applied to the orthogonal axis. Hence, the separation is two-dimensional. A practical realization is presented in [KF+17], which is shown in Fig. 4.8 a). It must be noted that the two lower spheres should also be aligned at one axis. This could be achieved, if e.g. all four spheres were rotated by 45° as indicated in Fig. 4.8 b). The spherical form ensures that the size of the blocking and pass areas are independent of the incident angle compared to the planar LCD filter. If this form is not possible in an application, a checkerboard or strip filter will be the planar equivalent.

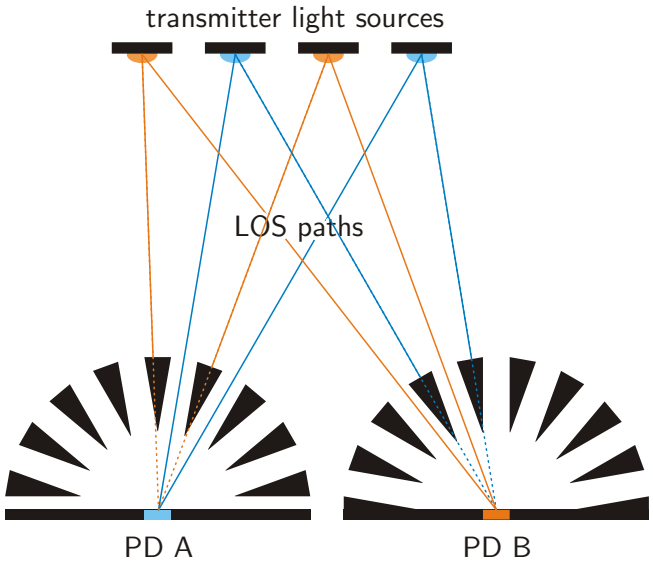

Figure 4.7: Principle of passive interference suppression filter.

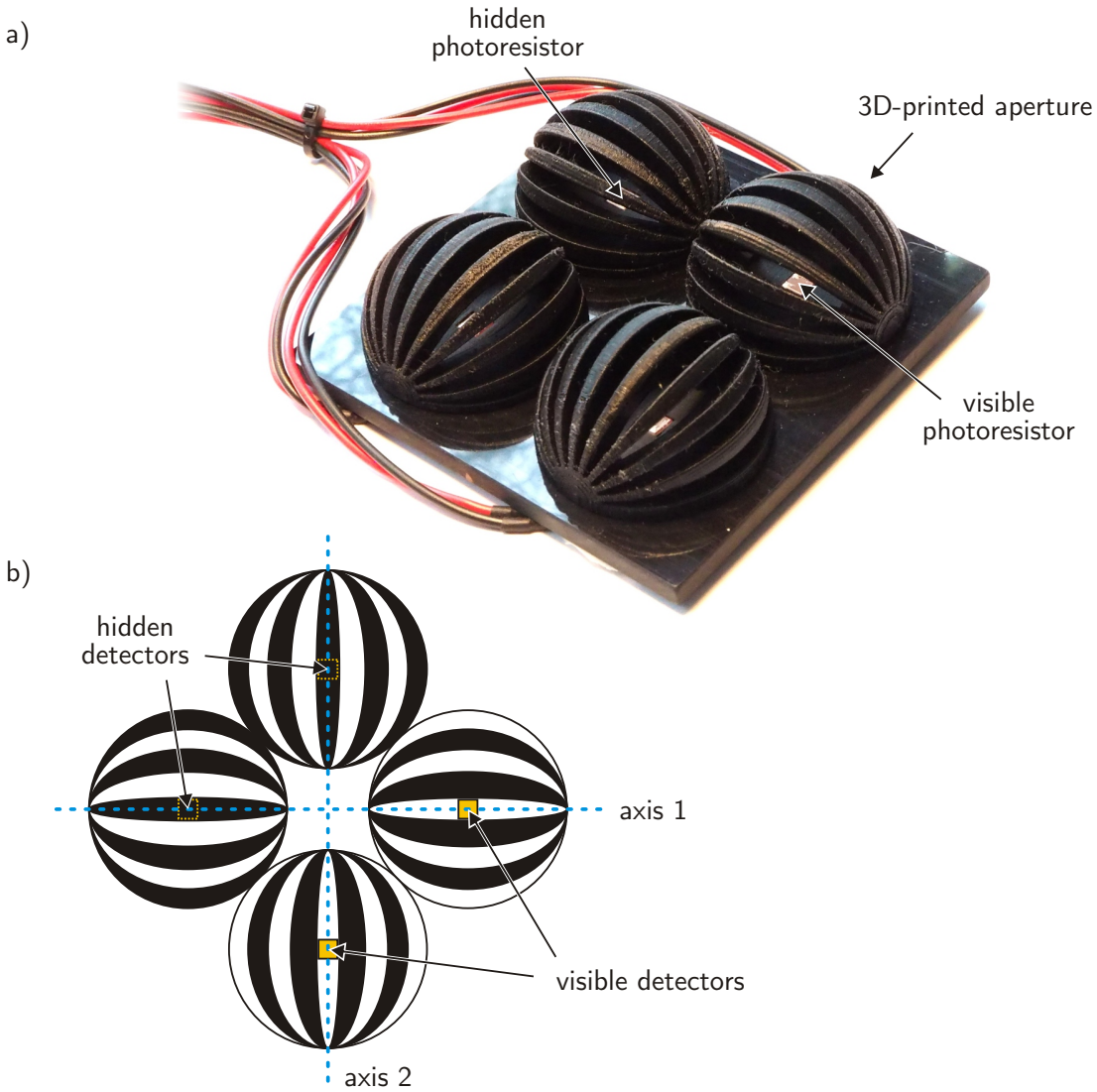

Figure 4.8: a) 3D-printed interference suppression filters for a receiver using four photoresistors as detectors, presented in [KF+17]. b) Ideal rotation of filters for each axis (top view).

4.3.1 Camera-based Receiver

The following section is based on publication [KH+18b].

A completely different type of receiver is a camera-based one, also known as LED-to-Camera transmission. When a color camera is used, three channels (red, green and blue) can be used independently with LEDs that are also colored. Today, the light-sensitive module is manufactured in the complementary metal-oxide semiconductor (CMOS) technology for most applications – commonly known as CMOS camera. A camera can separate all

light sources in its FOV in terms of image pixels, so that a separation is possible without further actions in the physical domain [LC+16]. The separation and decoding are done by video/image software processing. Possible applications are near field communication (NFC) scenarios with smartphone-based receivers [LH+19], health applications [RA+17] as well as data extractions with e.g. hijacked surveillance cameras [GZ+17].

A major drawback of camera-based receivers is the low frame rate of the cameras compared to photodetectors, which leads to low data transmission rates. One could either exploit the rolling shutter effect [CC+15] or employ higher-order modulation schemes as done in the mentioned publication [KH+18b]. Furthermore, the crosstalk between colors needs to be considered when parallel color channels should be used as the spectral response of the camera and the LEDs might not be identical [LC+16]. High brightness values like a point-source-like LED can locally saturate the camera sensor, which results in white pixels only irrespective of the actual color. As countermeasure, blurring the image or averaging over multiple pixels could lower the saturation effect, spreading the light intensity over a greater area, as shown in Fig. 4.9.

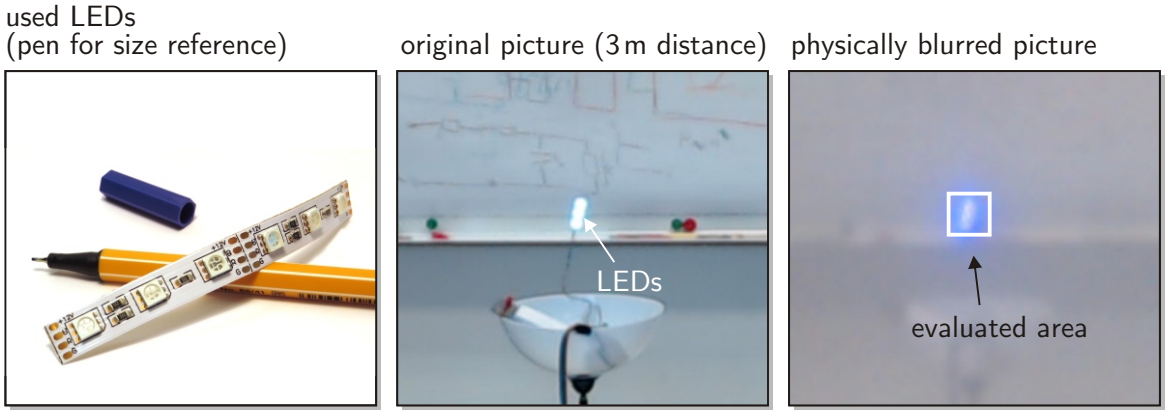

Figure 4.9: Blurring the picture of the LED stripe (shown left) with metallic anti-static foil in front of the camera: saturated white pixels (middle) become blue pixels (left) – the original color of the LEDs. Only the indicated white square is evaluated for data recovery [KH+18b].

An experimental transmission with PAM-4 over 3 m is shown in Chapter 6.2.4.2.

4.3.2 Imaging Optics

Related to camera-based systems, there are also receivers with imaging optics. In this case, lenses are used to project the light sources onto a receiver plane. For covering a large FOV,

e.g. fish-eye or hemispherical lenses are suitable [JW+18; GC18]. The receiver plane can be realized as a photodetector array or a CMOS array.

4.4 Summary

In this chapter, interference mitigation methods for VLC MIMO scenarios are discussed. At first, algorithmic approaches such as zero-forcing precoding are considered and their possibilities and limitations are shown. Afterwards, physical interference mitigation methods are presented. Beginning with active methods, the novel LCD interference suppression filter is introduced. The basic principle and geometric construction is shown and how the LCD filter can be described mathematically and integrated into the previously presented MIMO channel model from Chapter 2.2. Regarding the applicability, the limitations are also derived and a draft for a VLC system using this type of filter is suggested. The resulting optimization problem of how to distribute the transmitter light sources to the receivers with the help of the LCD filters is explained and different solution approaches are given. The optimization problem is modeled as "Santa Claus problem on unrelated, parallel machines", where the maximizing of the minimum SINR among all users is the target. For solving this problem, several suitable methods are presented. At first, a non-deterministic genetic evolutionary optimization is introduced and explained in detail. Afterwards, a deterministic heuristic allocation algorithm for solving the "Santa Claus" problem is presented. Combined approaches with conventional methods are considered, too. Here, an alternative problem modeling is also performed: genetic optimization sets directly the pixel pattern for each user, while ZF precoding iteratively calculates the achievable rates for each pattern setting. The resulting rates are used as feedback for the genetic algorithm.

Moreover, different methods for special VLC applications are considered. LED-to-camera data transmission methods are discussed, which are especially suitable for internet-of-things applications, and also passive interference mitigation techniques are presented.

5

Numerical Simulation Model

For evaluating the presented VLC channel model in Chapter 2.2 including the LCD interference suppression filter, a numerical simulation tool was developed. This tool should be able to carry out performance evaluations with high physical accuracy while being flexible in its configuration. The core is a numerical ray-tracer based on [BK+93]. Here, generalized Lambertian light sources are assumed and geometric light ray calculations are done for estimating the resulting light intensity at specific receiver locations. The LOS paths as well as reflections on the walls are determined and superimposed. In [BK+93] it is shown that the LOS bears most of the received intensity, followed by the first reflections on the walls. Further reflections can be neglected without great loss and by doing so, the computational complexity is drastically reduced. Another way to calculate the received intensity is to transform the scenario into the frequency domain as shown in [Sch16].

Different scenarios are investigated in order to test the impact of the LCD filter and to evaluate different optimization strategies and behaviors of massive MIMO systems. Consequently, some of the principles presented in Chapter 4 are implemented in the simulation model.

5.1 Simulation Model

The simulation model consists of different parts: the light sources, the walls, the LCD filters and the photodetectors. The light sources are modeled as Lambertian sources with mode number m and transmit power P_{Tx}. Spatially extended light sources can be modeled as spatially distributed point sources followed by processing each sub-light source on its own. Depending on the positions of transmitters and receivers, the distances and directions in

the form of vectors are calculated for all paths of the light rays and then (2.19) is evaluated.

The reflections are calculated by dividing the walls into tiles, which are then treated as Lambertian point sources as indicated in Fig 5.1.

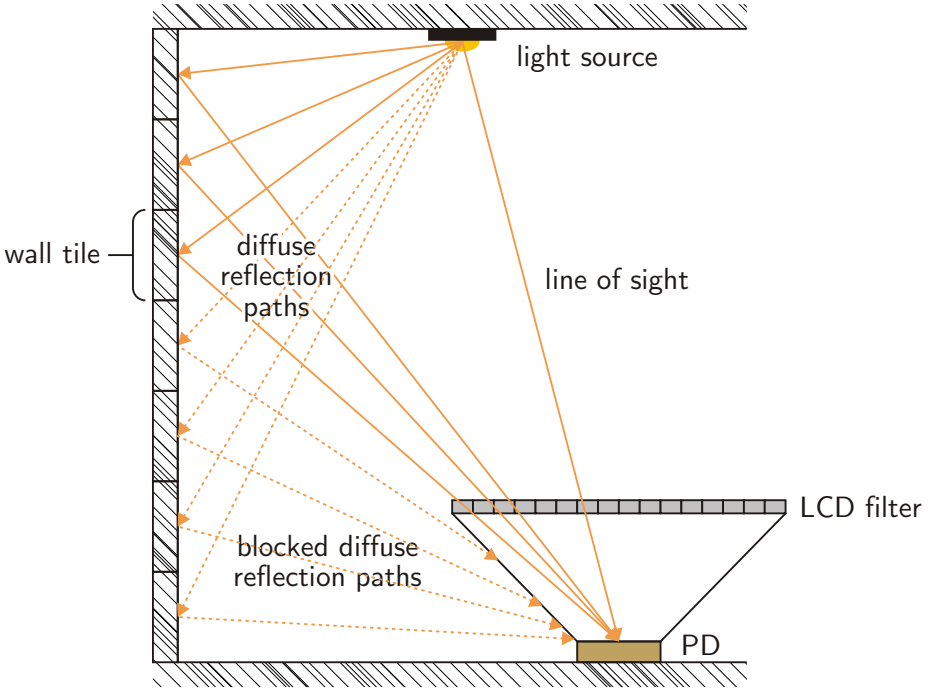

Figure 5.1: Schematic visualization of light rays.

Regarding the performance indicator, the minimum SINR is used as well as the minimum signal power. The minimum SINR is the SINR value of the user with the lowest SINR. The same applies for the minimum signal power. It should be noted that the signal power bears only the power of the desired signal in contrast to the total received power.

Additional performance measures are the sum-rate expression given in (2.24), when ZF precoding is applied in the scenario. Because the (constrained) ZF precoding optimization can be transformed in a convex problem [PK+11; YB+13] as mentioned in Section 2.2.3.1, the python library "CVXPY" is used in the simulation for solving this optimization problem [DB16; AV+18]. When genetic evolutionary optimization is applied, the python library "deap" is used for modeling the problem structure [FD+12]. In the special case of spatial encoding scenario, the bit-error rate expressions given in (2.22) and (2.23) are used.

5.1.1 Modeling of the LCD Filter

The LCD filter is modeled as a square grid of $n_{\mathrm{px}} \times n_{\mathrm{px}}$ pixels, which have a transmission factor $g_{\mathrm{LC,px}} \in [0, 1]$ and an area of $a_{\mathrm{px}} \times a_{\mathrm{px}}$. This filter is assumed to be located at a distance h, centered above the photodetector. The edge length a_{px} is an integer divisor of the photodetector edge length a_{PD}. For a full coverage of the FOV, and thus a better approximation of the paths of rays, the LCD needs to be extended as shown in Fig. 5.2. The required number of pixels along one axis can be calculated by

$$\begin{aligned} \left(\frac{n_{\mathrm{px}}}{2} a_{\mathrm{px}} - \frac{a_{\mathrm{PD}}}{2}\right) \frac{1}{h} &= \tan(\theta_{\mathrm{FOV}}) \\ \Rightarrow n_{\mathrm{px}} &= \left(\tan(\theta_{\mathrm{FOV}}) h + \frac{a_{\mathrm{PD}}}{2}\right) \frac{2}{a_{\mathrm{px}}}. \end{aligned} \tag{5.1}$$

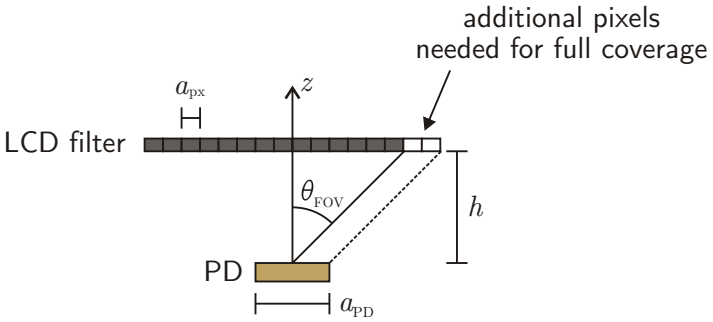

Figure 5.2: Additional pixels for full FOV coverage, based on [KH+22].

Based on the optical characterization of a real LC cell in Section 6.3.2, a numerical model of the transmission characteristics is created. The measurements were done for differently colored LEDs, but here the results for the blue LED are used as they form the basis for white light phosphor LEDs. The individual transmission factors for pass mode and blocking mode were measured at different rotations from 0° to 75° in steps of 10° in one direction, and from 0° to 90° in three steps for the orthogonal direction. By doing so, the incident angle of the light changes, and its influence on the LC cell can be seen. Then, linear interpolation is used to derive the transmission factor for the in-between angles in both directions.

For checking the basic behavior of the VLC scenario, an ideal model is also available, which means that the LCD filter has no losses in pass mode – regardless of the incident angle – and blocks perfectly in blocking mode. Consequently, the transmission factor is either “1” or “0”.

To determine the appropriate pixel, which gets hit by a simulated ray of light, vector operations are used. The LCD is modeled as a plane located at the specified distance d above the photodetector. Knowing the origin of the light source – either a wall tile or a light source – and the destination, namely the photodetector with position $\boldsymbol{p} = [x, y, z]^T$, the intersection i of the light vector $\boldsymbol{v}$ with the LCD plane A can be calculated by

$$\boldsymbol{i} = \boldsymbol{p} - \boldsymbol{v}\frac{((\boldsymbol{p} - \boldsymbol{p} + [0, 0, d]^T) \cdot [0, 0, 1]^T)}{\boldsymbol{v} \cdot [0, 0, 1]}. \tag{5.2}$$

With the intersection point $\boldsymbol{i}$, the position on the LCD is determined. The distances d_x and d_y along the x and y axes between intersection and center on the LCD plane are calculated as follows:

$$[d_x, d_y, d_z]^T = \boldsymbol{p} + [0, 0, d]^T - \boldsymbol{i}, \tag{5.3}$$

where d_z is always zero. Given d_x, d_y and the pixel edge length a_{px}, the corresponding pixel indices $i_{\mathrm{px},x}$ and $i_{\mathrm{px},y}$ from the center point can be retrieved by

$$i_{\mathrm{px},x} = \left\lfloor \frac{d_x}{a_{\mathrm{px}}} \right\rfloor, \tag{5.4}$$

$$i_{\mathrm{px},y} = \left\lfloor \frac{d_y}{a_{\mathrm{px}}} \right\rfloor, \tag{5.5}$$

where $\lfloor \cdot \rfloor$ is the floor operation. With the pixel gain matrix defined as

$$\mathbf{G}_{\mathrm{LC}} = \begin{bmatrix} g_{\mathrm{LC},0,0} & \cdots & g_{\mathrm{LC},0,n_{\mathrm{px}}-1} \\ \vdots & \ddots & \vdots \\ g_{\mathrm{LC},n_{\mathrm{px}}-1,0} & \cdots & g_{\mathrm{LC},n_{\mathrm{px}}-1,n_{\mathrm{px}}-1} \end{bmatrix}, \tag{5.6}$$

the entry $g_{\mathrm{LC},(i_{\mathrm{px},x}+n_p x/2),(i_{\mathrm{px},y}+n_{\mathrm{px}}/2)}$ is the desired gain factor for this specific ray of light, if $i_{\mathrm{px},x}$ and $i_{\mathrm{px},y}$ are not greater than $\frac{n_{\mathrm{px}}}{2}$. Otherwise, the gain is zero because the incident angle is greater than the FOV.

5.1.2 Modeling of the Photodetector

As the LCD filter is placed within short distance above the photodetector in relation to the room dimensions, it cannot be assumed as point sink any longer – otherwise the pixel pattern of the LCD would create an inaccurate received intensity. Hence, the area of the photodetector is divided into pixel-sized sub-areas of $a_{\mathrm{px}} \times a_{\mathrm{px}}$ and each sub-area

is evaluated individually by calculating all rays, given the correct physical location of the sub-areas (Fig. 5.3). Finally, all portions of the sub-detectors are summed up in order to obtain the total received value.

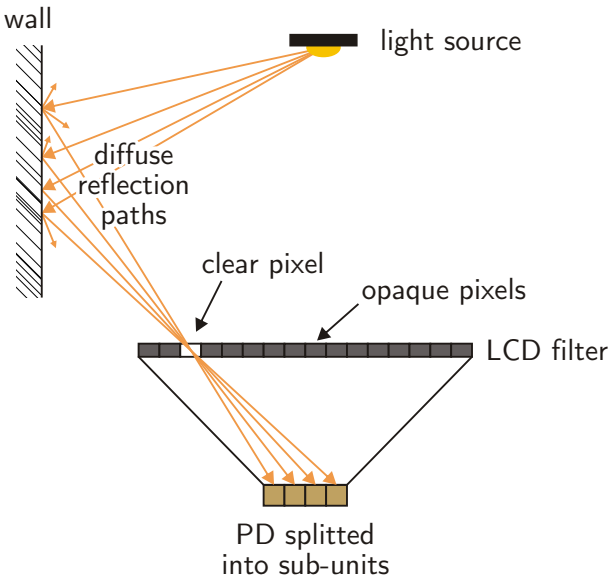

Figure 5.3: Arrangement of sub-detectors, based on [KH+22].

5.1.3 Pre-Calculation of Channel Coefficients

If many hundred or thousand different pixel settings should be optimized, the process would be very time consuming as every little change necessitates a new full simulation run. With n_{px}^2 pixels per receiver, there are $2^{(K \cdot n_{\mathrm{px}}^2)}$ different possible combinations for the pixel states. Using exhaustive search is not feasible when the optimal pixel settings for the K users are at stake. The number of combinations doubles with every additional pixel. But there is a possibility to reduce the number of required simulations for the desired channel setting to a more linear growth by calculating the influence of each pixel on the channel individually and store the value in a look-up table. To be more precise, all pixels are set to a transmission factor of zero, except for one pixel, which is either set to the appropriate blocking mode or pass mode factor. Then the channel matrix is calculated and stored for both cases. This is done for every pixel, so that there are $K \cdot n_{\mathrm{px}}^2$ simulation runs in total.

Regarding a simulation run of a certain pixel pattern, the corresponding pre-calculated channel matrices $\mathbf{H}_{\mathrm{px}}$ are retrieved from the look-up table and superimposed to obtain the

total channel matrix:

$$\mathbf{H} = \sum_{(K \cdot n_{\mathrm{px}}^2)} \mathbf{H}_{\mathrm{px}}, \tag{5.7}$$

where $\mathbf{H}_{\mathrm{px}}$ includes all rays h_{LOS} and h_i for every receiver which pass through the corresponding pixel.

This procedure is beneficial for simulations in which more than $K \cdot n_{\mathrm{px}}^2$ different pixel patterns should be evaluated as e.g. with genetic evolutionary optimization described in Section 4.2.3.4. It should be noted that the pre-calculation can only be applied when all receivers have fixed positions and orientations.

5.2 Evaluating of Different Scenarios and Methods

In the previous section, different methods are presented which employ the LCD filter in order to increase the performance. The presented numerical simulation system is now used for testing these methods in different scenarios. All indoor scenarios are modeled according to the Barry-A room in [BK+93]. The dimensions are 5 m $\times$ 5 m $\times$ 3 m (length $\times$ width $\times$ height). For free-space or multicell settings, the dimensions of the cell size and ceiling height are also derived from this basic structure.

At first, a 4×4 MIMO single-user scenario is taken, where spatial multiplexing and spatial modulation are employed together with the LCD filter. Here, the receiver consists of four independent photodetectors with a single LCD filter. Secondly, a 4×2 multiuser setting is evaluated, where conventional zero-forcing precoding is combined in an iterative manner with a genetically optimized pixel-pattern for LCD filters, as described in Chapter 4.2.3.4. In contrast to the first scenario, each user, respectively receiver, has only a single photodetector with an individual LCD filter. Afterwards, a massive MIMO system is considered, where the novel kind of binary precoding and allocation method with jointly set LCD patterns presented in Chapter 4.2.3 is used in order to increase the minimum SINR. Compared to the first scenario, the amount of transmitter light sources is increased to simulate the massive MIMO impact. Based on this, the influence of the wall reflections on the performance is evaluated, which means that the scenario is basically transformed into free-space transmission. In the last scenario, multiple neighboring cells are introduced for the analysis of interference terms that are not in control of the allocation process. The simulations are performed with the ideal LCD filter model and the realistic one, based on the characterization in Section 6.3.2.1.

5.2.1 Single-User Scenario with Spatial Modulation and Spatial Multiplexing

This part is based on publication [KF+19].

The setting is modeled after [FH13], where an upper bound for the bit-error rate is used as performance index. The transmitter and receiver positions are indicated in Fig 5.4 b). For performance evaluation, the BER upper bounds (2.22) and (2.23) are used as in the reference setup. The receiver is placed at positions A-C 0.5 m above ground level, which should represent three typical cases, motivated by [GC18]: At position A, the receiver is placed at the center of the room and is equally illuminated by all four light sources. At position B, the receiver is placed directly below a light source, which makes it the dominant one, and finally, at position C, the receiver is placed near a reflecting wall between two light sources. The simulation parameters can be found in Table 5.1. Each light source is assigned to one photodetector of the receiver, which means that the aperture of the LCD is also set to the line of sight of the assigned light source.

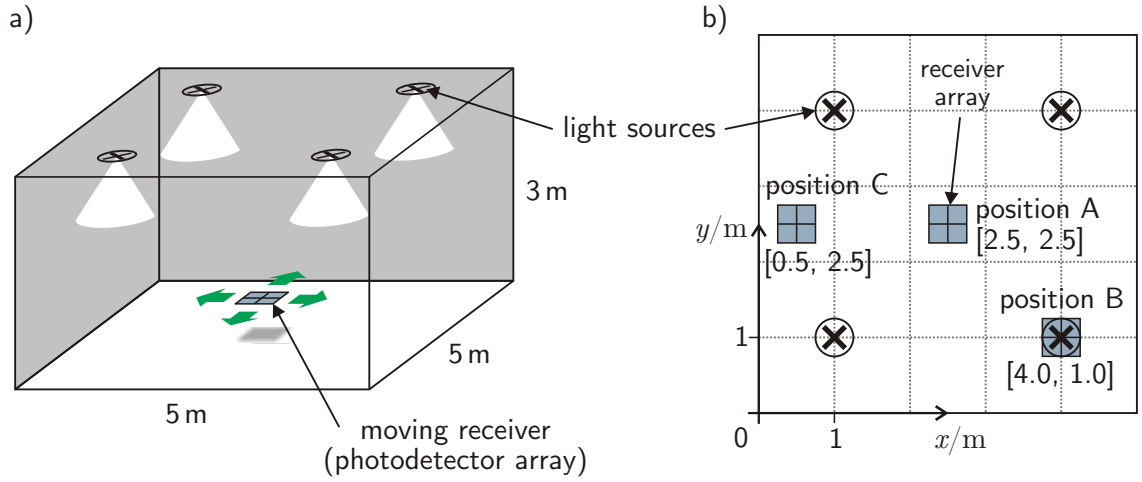

Figure 5.4: a) VLC setting with four light sources. One receiver consisted of four photodetectors; b) positions of light sources and receiver (top view of room), based on [KF+19].

The BER performance results are plotted in Fig. 5.5 and Fig. 5.6. For comparison, the performance is also calculated for a reference receiver without LCD filter. At position A (center of the room), spatial modulation benefits the most from the LCD channel decorrelation with an improvement of 27 dB at a BER level of 10^{-3} compared to spatial multiplexing, which shows only a gain of 7 dB. In case of a higher spectral efficiency with $R = 8$ bit/s/Hz, the behavior is similar. Moving the receiver to position B (directly below

Table 5.1: Parameters for Spatial Modulation and Multiplexing Simulation

Positions of light sources $[x, y, z]$/m	$[1.0, 1.0, 3.0]$, $[4.0, 1.0, 3.0]$, $[1.0, 4.0, 3.0]$, $[4.0, 4.0, 3.0]$
Positions of receiver $[x, y, z]$/m	$\mathrm{A} = [2.5, 2.5, 0.5]$, $\mathrm{B} = [4.0, 1.0, 0.5]$, $\mathrm{C} = [0.5, 2.5, 0.5]$
FOV of photodetectors	$\pm 85^\circ$
Photodetector/aperture size A_{PD}	1 cm^2
LCD distance h	1 cm
Wall reflectivity h_{Wall}	0.8
Wall tile size	1 cm^2
Spectral efficiency R	4 bit/s/Hz and 8 bit/s/Hz

a light source) does not show an improvement to the reference case, due do the strong impact of the overhead light source. At position C (near the wall), there is a performance gain of approximately 10 dB for spatial modulation regardless of the spectral efficiency. Spatial multiplexing benefits only for $R = 4$ bit/s/Hz.

5.2.2 Combination of ZF Precoding and Genetic LCD Optimization

This part is based on publication [KP+22].

In this scenario, two receivers with one photodetector each are deployed at different positions in the room. There are two different cases of position sets: First, the receivers are placed far away from each other, and second, the receivers are placed near to each other to simulate a highly correlated channel. Four light sources are suspended from the ceiling with a distance of 0.5 m illuminating the room. At the transmitter side, ZF precoding is applied as explained in Section 4.1, and at the receiver side, a genetic evolutionary optimization of the pixel patterns of each receiver is performed. Because of the high complexity due to the massive amount of pixels and therefore the high number of possible states to evaluate, genetic optimization is a promising method for finding good pixel patterns, which help to de-correlate the channel. In this scenario, the pre-calculation of channel coefficients as mentioned in Section 5.1.3 is done before the optimization process. The transmitter and receiver positions are given in Table 5.2 as well as the parameters for the genetic evolution.

In a first simulation, the achievable data rate is evaluated dependent on the transmit power. Here, the realistic LCD model from the previous simulation scenario is taken, and,

for reference, an ideal LCD as well as a receiver without LCD filter is used. The numerical results are shown in Fig. 5.7. A second simulation evaluates the influence of the parameters for the genetic optimization, namely the number of individuals per population and the number of generations, which is shown in Fig 5.8.

By comparing case 1 and 2, it can be seen that the LCD filter is able to effectively remove the cross-channel interference: When the receivers are separated by a large distance, as in case 1, the cross-correlation between their channel coefficients is very low. Hence, ZF precoding at the transmitter is sufficient to separate the channels. In case 2, where the receivers are close together, ZF precoding delivers only poor performance. However, when offered a less correlated channel by the LCD filter, ZF precoding is able to reach a performance similar to case 1 – even with a non-ideal LCD filter that causes additional losses.

Regarding the genetic optimization parameters, non-optimal settings improve the transmission performance, too, which can be exploited to reduce time effort and computational complexity of the optimization process. With a fixed population size, small numbers of generations produce an improved result because there is a chance that even a randomly generated LCD pixel pattern achieves a better performance than the reference setup – especially with a large population size. In the other case, a fixed number of generations, only a small population size is required to outperform the reference, although the gain can vary due to the small sample size for the case of less allowed generations.

Table 5.2: Parameters for ZF precoding and Genetic Optimization Simulation

Simulation Parameters	
Lamp positions	$[1.25, 1.25, 2.5]$, $[1.25, 3.75, 2.5]$, $[3.75, 1.25, 2.5]$, $[3.75, 3.75, 2.5]$
Receiver positions (Case 1)	$[2.05, 1.6, 0.85]$, $[3.2, 3.9, 0.85]$
Receiver positions (Case 2)	$[2.05, 1.6, 0.85]$, $[2.05, 1.4, 0.85]$
FOV of photodetector	$\pm 62^\circ$
LCD filter dimensions	4 cm $\times$ 4 cm with 16×16 pixels, $h = 4$ cm above PD
Target BER	1e-3
Genetic Algorithm Parameters	
Generations	20
Number of individuals	100
Mutation probability	0.2
Crossing probability	0.5
Tournament sample size	3

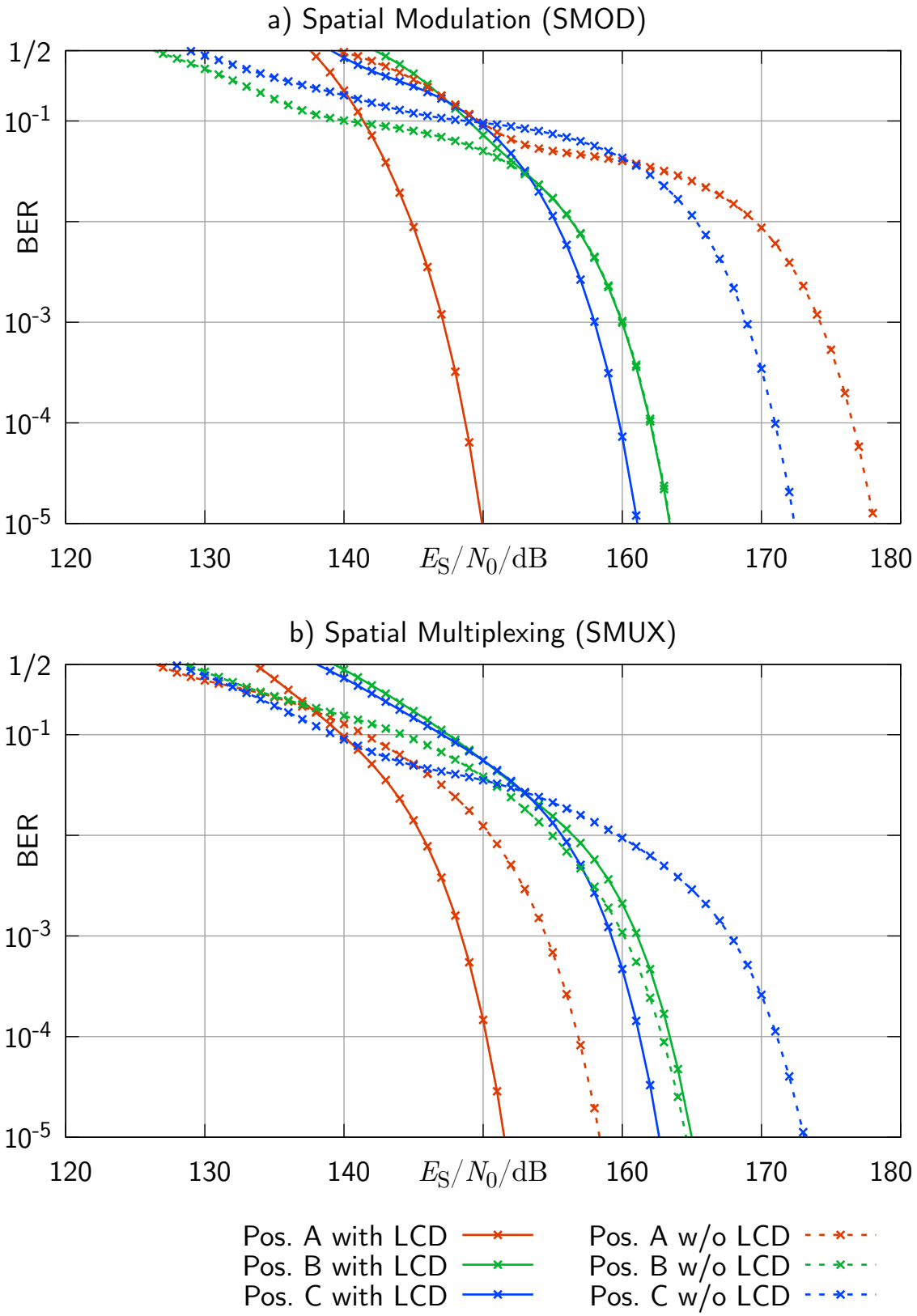

Figure 5.5: BER performance of scenario in Sec. 5.2.1 for a) spatial modulation and b) spatial multiplexing; $R = 4$ bit/s/Hz.

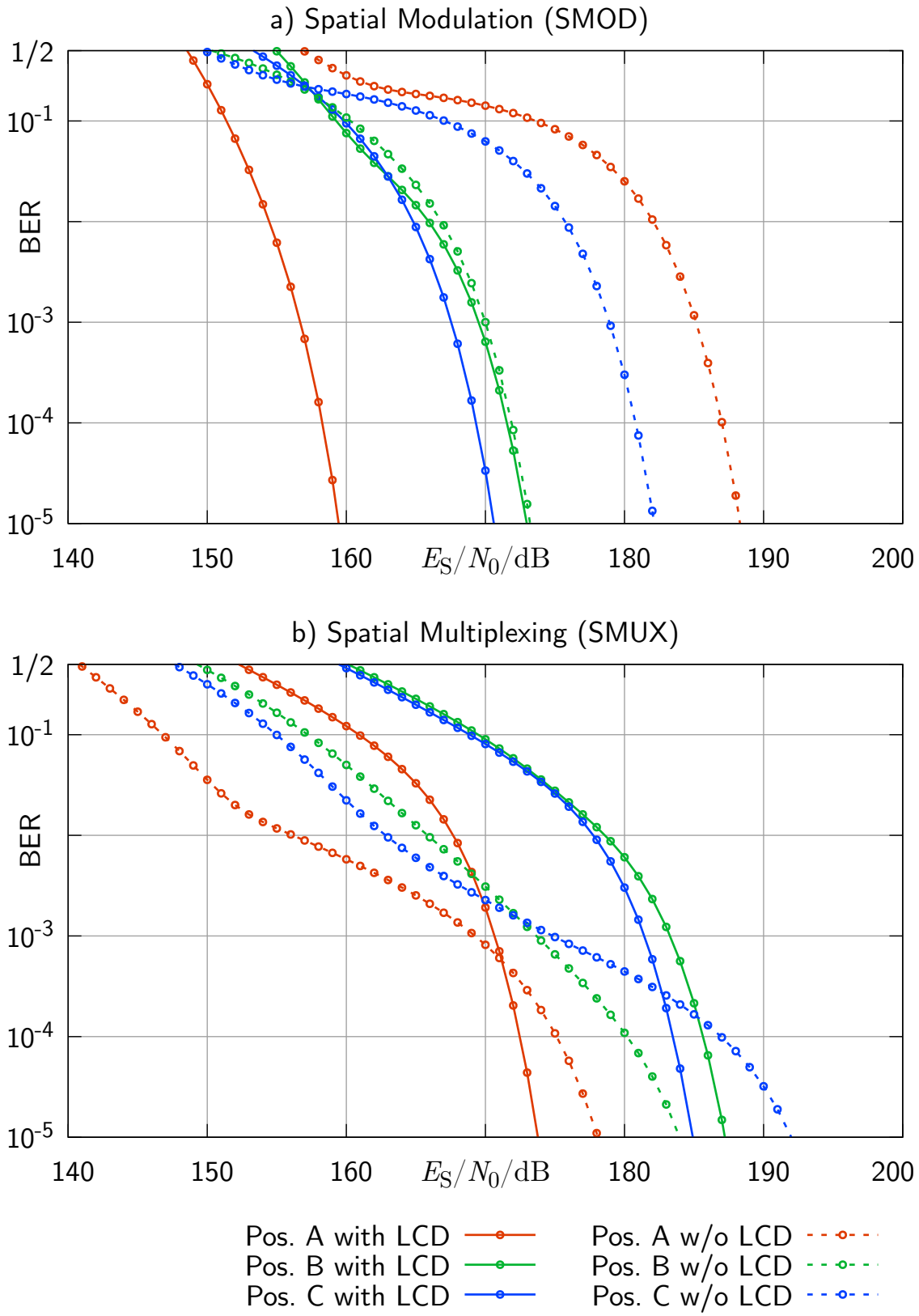

Figure 5.6: BER performance of scenario in Sec. 5.2.1 for a) spatial modulation and b) spatial multiplexing; $R = 8$ bit/s/Hz.

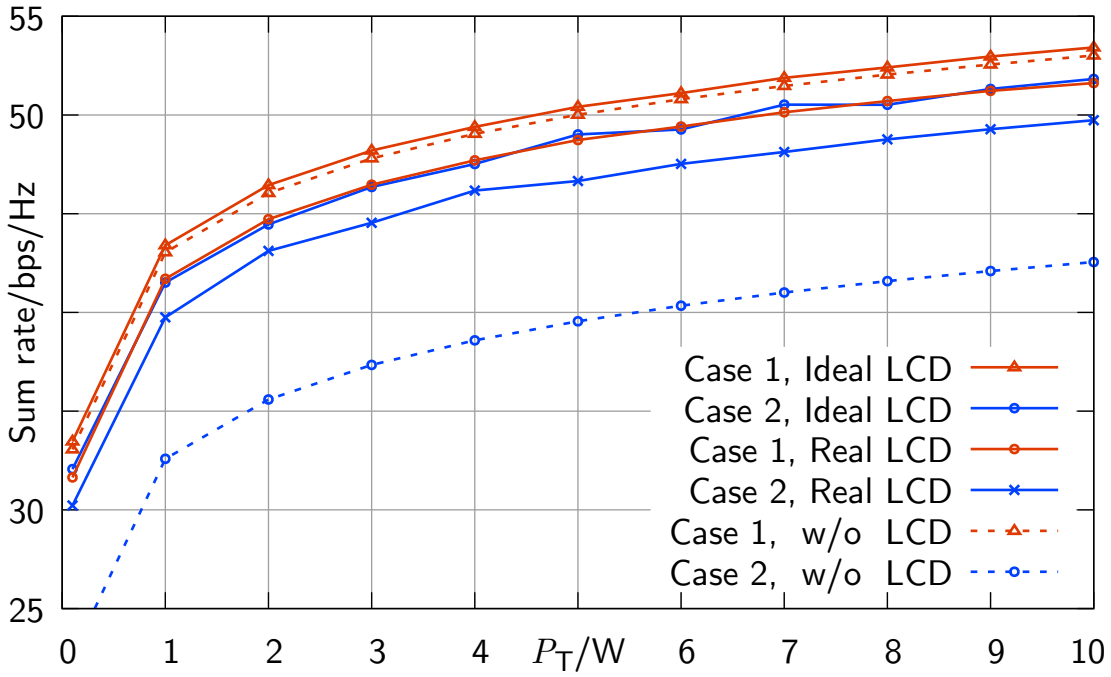

Figure 5.7: Sum rate performance of scenario in Sec. 5.2.2 for position cases 1 and 2, depending on the transmit power.

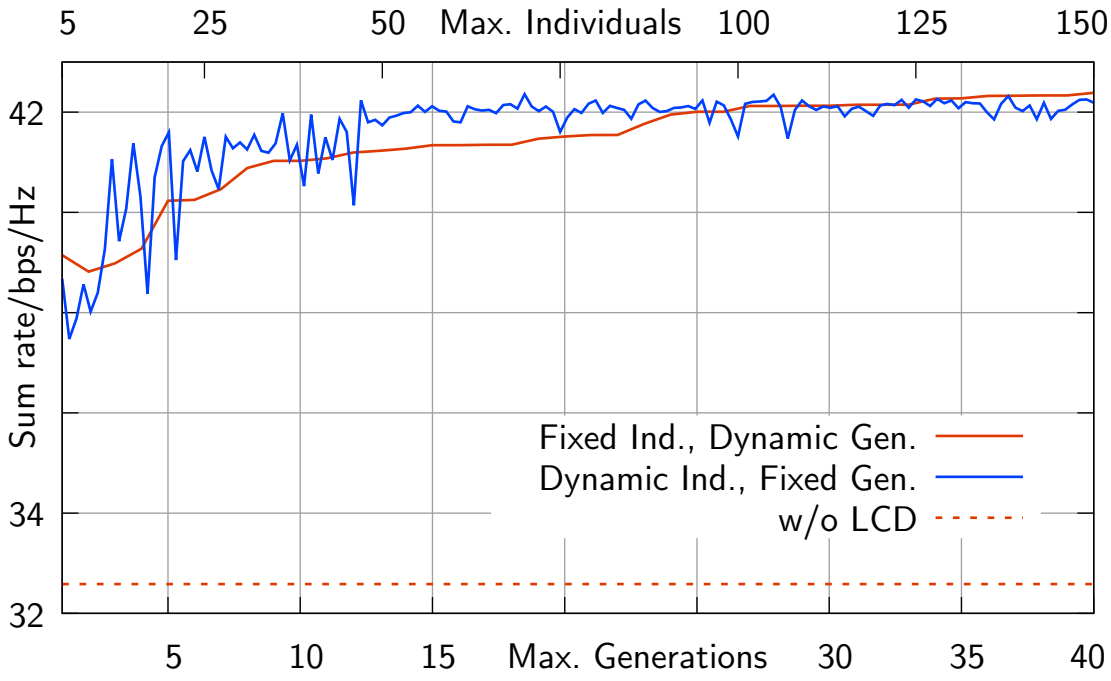

Figure 5.8: Sum rate performance of scenario in Sec. 5.2.2 for variation of genetic optimization parameters in position case 2 with $P_T = 1\,W$.

5.2.3 Massive MIMO Scenario

In contrast to the previous scenarios, subsequently several transmitter lights are attached in a grid form to the ceiling to form a massive transmitter array. The number of transmitters is varied from $2 \times 2 = 4$ to $15 \times 15 = 225$. Four receivers with one photodetector each are roaming at a height of 0.85 m above floor level inside the room. An additional change compared to the previous settings is that more plausible receiver dimensions are assumed with the physical testbed presented in Chapter 7 in mind. All parameters are given in Table 5.3.

For evaluating the influence of the reflections, different settings were tested: First, a scenario with reflections is simulated, and second, the same scenario without reflections, i.e. assuming a wall reflectivity factor of zero. When there are no reflections present, the scenario can be considered as equivalent to a free-space scenario with a bounded area for the receivers, where only the LOS paths are evaluated. Since they bear most of the received intensity, a good approximation is achieved while keeping the computational complexity in a reasonable limit. Hence, for different settings, where the distances between photodetectors and LCD filters are varied, only the LOS paths are simulated. In order to keep the FOV constant, the sizes, respectively the amount of pixels of the LCD filters, are adapted, too. The applied pattern style is given in Sec. 4.2.1 with additional reduction of the aperture size as described in Sec. 4.2.2.

To reduce the influence of the position of the receivers, they are placed randomly in the room and several simulation runs are carried out and averaged then. The x and y coordinates for the receivers are drawn from the interval $[0\,\mathrm{m}, 5\,\mathrm{m})$. Each set of positions will give a minimum SINR for the weakest of the four receivers and the corresponding received signal power. The resulting final minimum SINR value is an average of these minimum values of each simulation run. The allocation problem is modeled as "Santa Claus problem on unrelated parallel machines", which is described for this specific case in Sec. 4.2.3.1, and solved with genetic evolutionary optimization as well as with the heuristic approach presented in Sec. 4.2.3.2.

In Fig. 5.9 a), the minimum SINR with ideal LCD filters is given for different distances between LCD and photodetector, ranging from 20 cm to 5 cm, and different precoding and allocation schemes, while Fig. 5.9 b) presents the results for the realistic LCD filter. For reference, ZF precoding is used as well as the results, if any inference is absence. The received signal powers for the different scenarios are given in Fig. 5.10.

Compared to pure ZF precoding, the ideal LCD filter provides a gain ranging from 22 dB to 49 dB, which is at the same level as the reference case without interference. When

Table 5.3: Parameters for Massive MIMO Scenario

Simulation Parameters	
Room dimensions	L: 5 m, W: 5 m, H: 3 m
No. of LEDs N	4x4 to 15x15 array
Wall reflectivity factor	0.8
Wall tile size	0.0625 m^2
LED transmit power/watt	$1/N$
No. of users K	4 users randomly positioned at 0.85 m above floor
No. of simulation runs	3000; 300 (scen. with refl.)
PD active area	$2.5 \times 2.5\ \mathrm{mm}^2$
PD field of view	$\pm 45^\circ$
LC pixel size	$0.15625 \times 0.15625\ \mathrm{mm}^2$
LC distance	1.25 mm to 20 mm above PD
Target BER for constr. ZF precoding	1e-3
Genetic Algorithm Parameters	
Generations	$N \cdot K$
Number of individuals	100
Mutation probability	0.2
Crossing probability	0.5
Tournament sample size	3

the distances between the light sources get smaller than the allowed minimum separation distance, as defined in Sec. 4.2.2, the achieved minimum SINR drops below the ZF precoding performance, even with reduced aperture size. Increasing the distance between LCD and photodetector ($h = 20\,\mathrm{mm}$) results in a more reliable gain when the transmitter distances are decreased, even for a 15×15 array. Regarding the influence of the reflections, the performance drop starts much earlier, but with a less steep slope. With the realistic LCD model, the performance is similar to ZF precoding, while providing a much higher minimum receive power and a steady performance. Thus, it outperforms ZF precoding for larger array sizes, which decreases continuously. Another remarkable effect is the zig-zag behavior of the SINR performance. This phenomenon is caused by the ratio of N transmitters and $K = 4$ receivers. Because the number of transmitters is rising, an equal distribution of the transmitters to a fixed number of receivers is not possible. This occurs in every second case, when $N \mod K = 1$, due to the geometric growth of the transmitter array. Hence, the receiver with the minimum SINR has one transmitter assigned less than the three other ones in these cases. The LPT-SC-UPM algorithm performs similar to the genetic

optimization in less complex scenarios and outperforms it, when channel conditions are getting tough, while keeping the computational complexity low. In Fig. 5.11, the runtime for the different approaches is shown for the LOS scenario with an LCD distance of 10 mm.

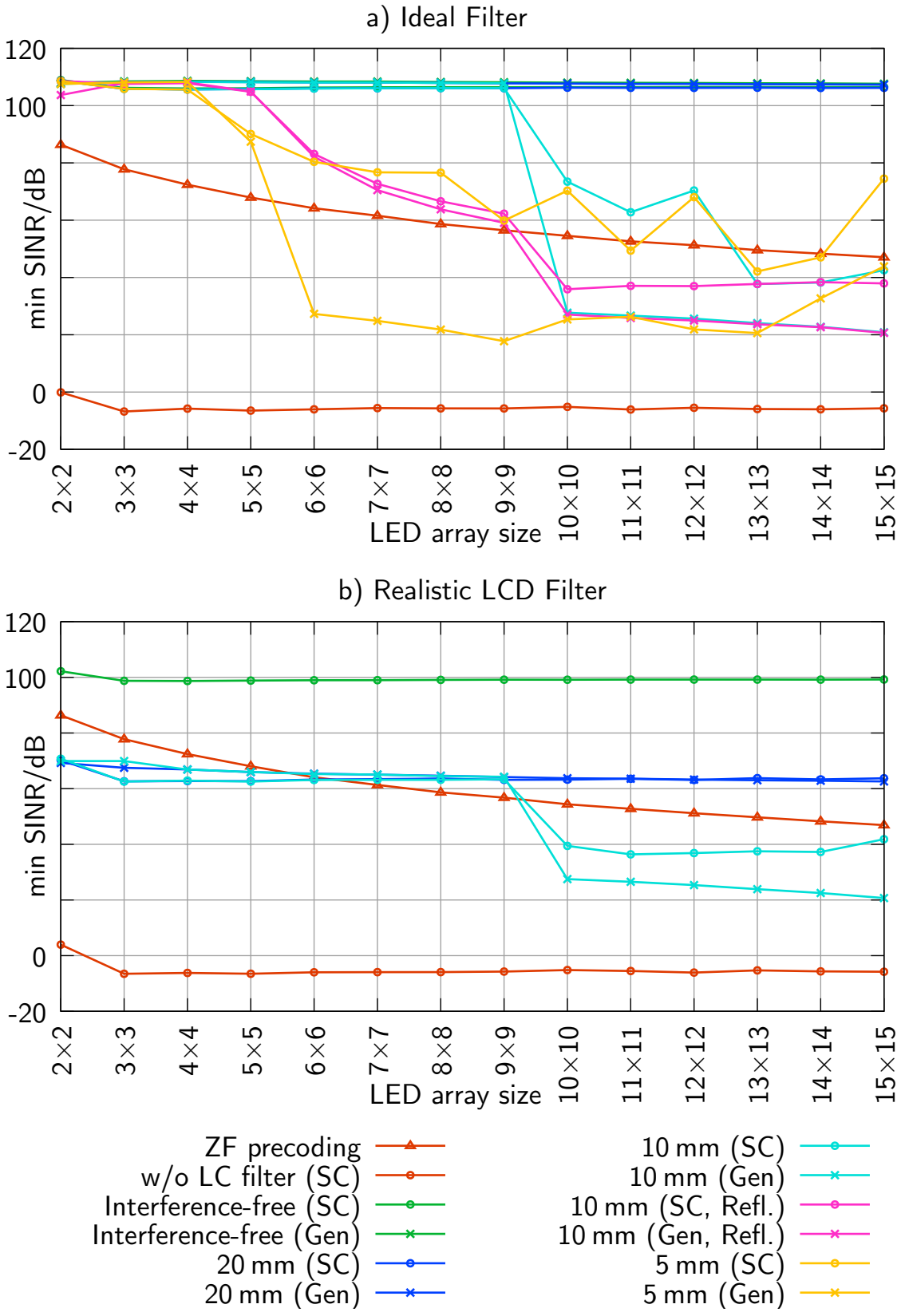

Figure 5.9: Minimum SINR performance for various parameters.

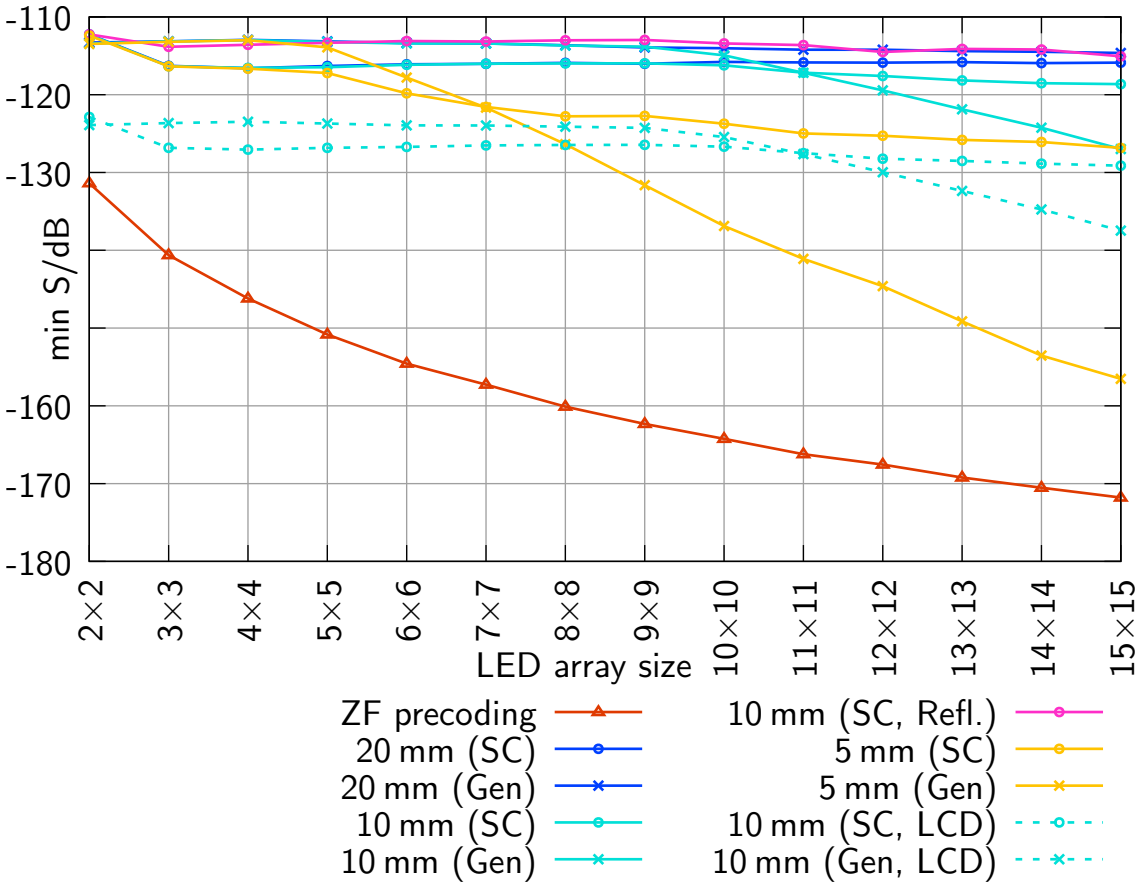

Figure 5.10: Minimum signal power performance for various parameters.

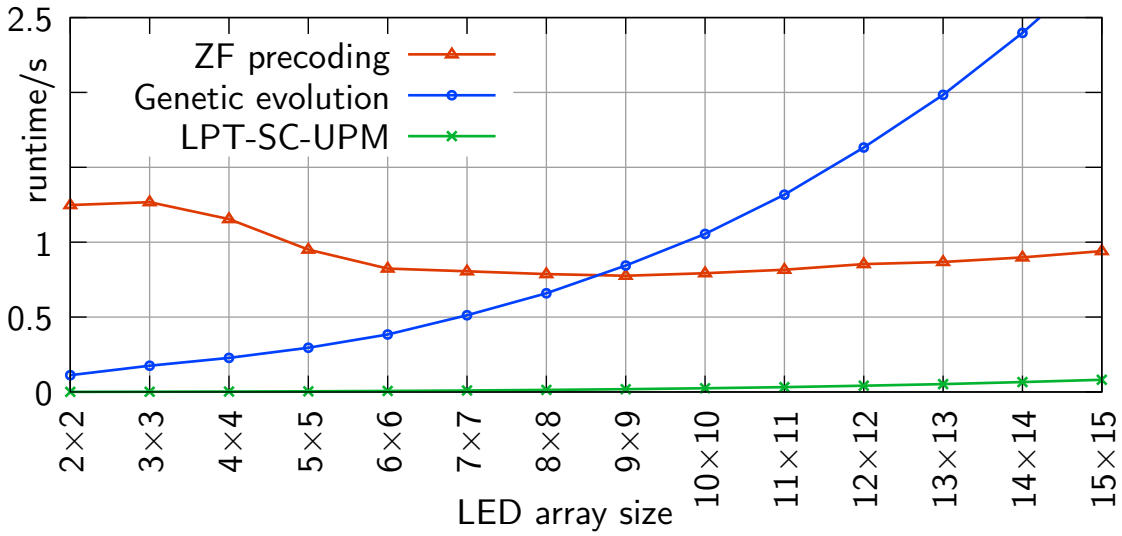

Figure 5.11: Averaged runtimes for ZF precoding, LPT-SC-UPM and genetic evolutionary optimization.

5.2.4 Multicell Scenario

In the multicell scenario, the edges of neighboring cells are modeled next to the borders of the test room, which is taken as "cell under evaluation", as indicated in Fig. 5.12. Similar to the free-space assumption, there are no reflections – only the LOS paths of transmitters and interfering light sources are present. The optimizing algorithms have access only to the weighting matrix $\mathbf{W}$ of the cell under evaluation.

In Fig. 5.13 it is clearly visible that ZF precoding fails with foreign interferers present, where the LCD filter shows a performance better than ZF precoding in the single-cell reference. Even the realistic LCD model can preserve approximately the single-cell performance.

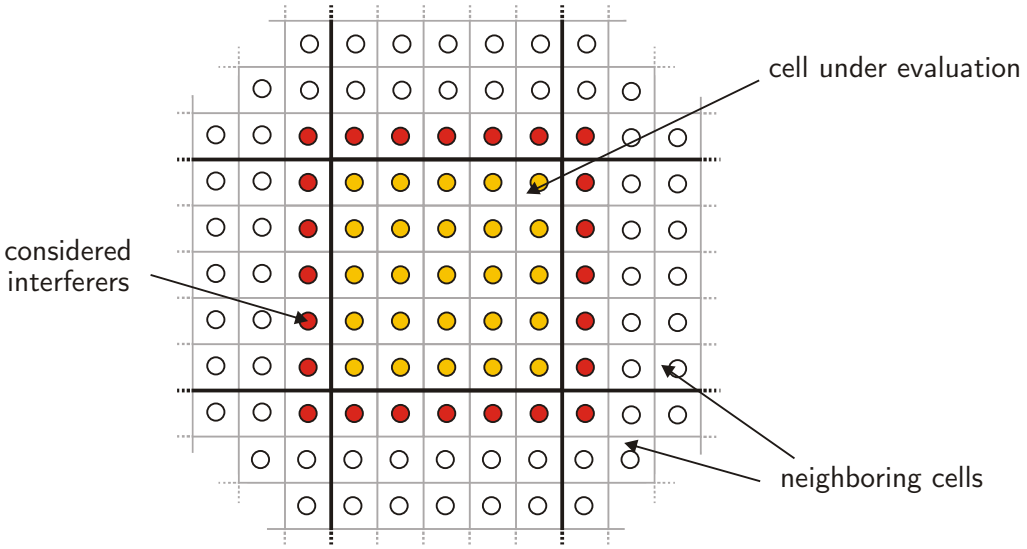

Figure 5.12: Multi-cell setting, based on [KH+22].

5.3 Summary

This chapter introduces the numerical simulation model, which was developed within this dissertation in order to gain insight into the performance of the LCD interference suppression filter in various scenarios. At first, the overall simulation principle is described. The LOS paths as well as the reflections on the walls are calculated according to the previously presented channel model. Subsequently, the geometric model of the LCD filter is explained in detail and how the impact of each pixel is evaluated. The angle-dependent transmission factors of the LCD pixels are interpolated by measured values of a real LC cell shown

in Chapter 6.3. For a higher accuracy, the photodetectors are also modeled spatially to ensure that their geometric dimensions are taken into account. Regarding the high number of degrees of freedom when all possible pixel state combinations should be considered, a time-saving method of precalculation of the channel coefficients is suggested. For doing so, the superimposing ability of light is exploited. By storing the influence of each pixel in a look-up table, the complexity can be reduced to a linear behavior instead of an exponential behavior.

The presented simulation model is taken and different scenarios are created. Starting with a single-user setup, the LCD filter is benchmarked against spatial modulation and spatial multiplexing. In the next scenario, the performance of the LCD filter is tested in comparision with sole ZF precoding. Here, a pixel-wise genetic evolutionary optimization is used to separate the subchannels and to support the ZF precoding in a jointly approach. The next two scenarios evaluate the effects of a massive MIMO setting, where the number of transmitters is increased steadily, while the second scenario also introduces neighboring cells as interferers. For these two scenarios, the light source distribution problem is modeled as “Santa Claus” problem and genetic evolutionary optimization is applied as well as the deterministic, heuristic approach presented in Chapter 4.2.3.2.

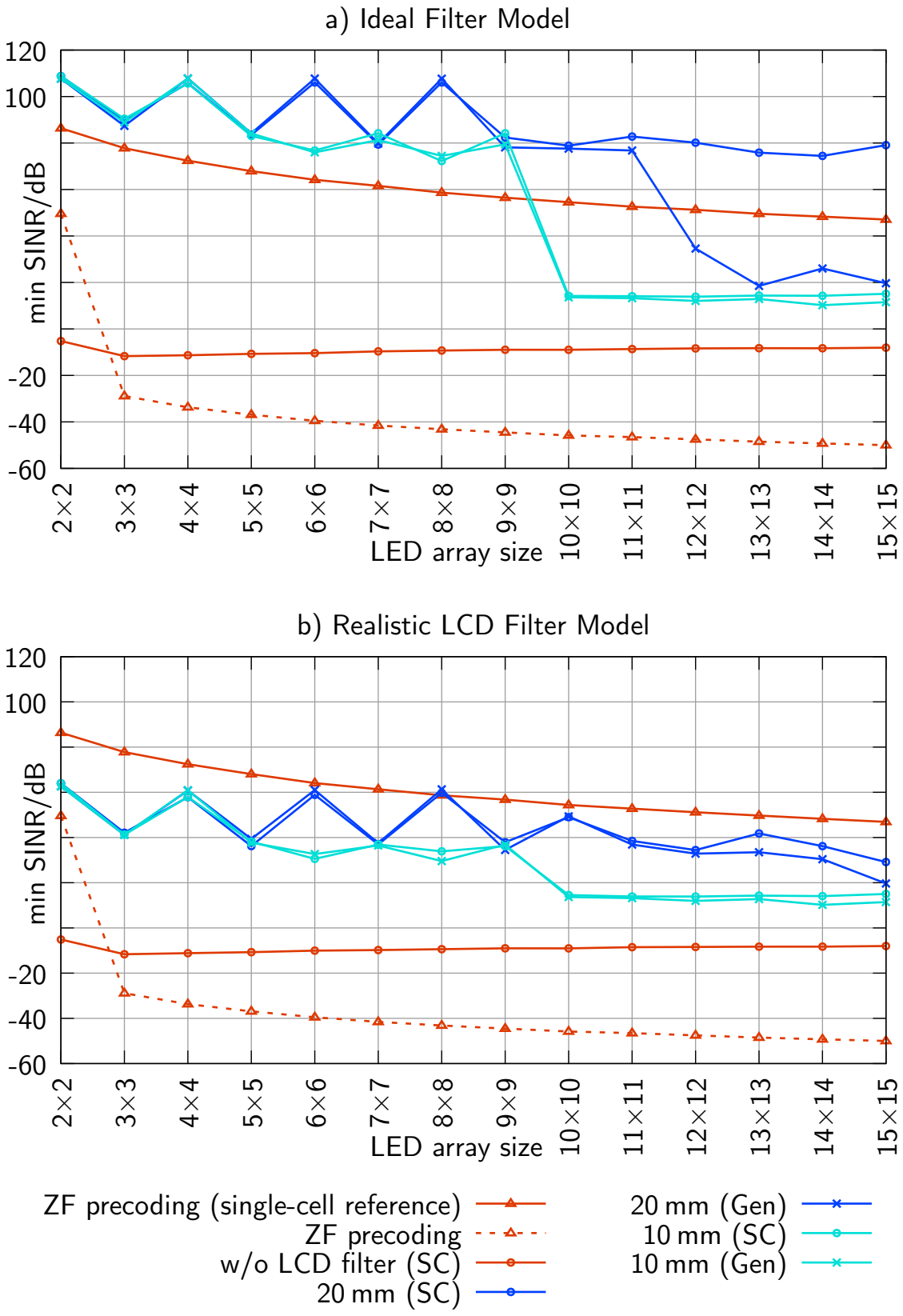

Figure 5.13: Minimum SINR performance for various parameters in the multicell scenario.

Part III

Hardware and Experiments

6

VLC Transmitter and Receiver Components

Nowadays, the light-emitting diode is the most prominent light source and consequently the one which is investigated here. It is energy-efficient, cost-effective, durable, compact, relatively high-speed switchable and creates a pleasant light, which is suitable for most applications. There are many ways to drive an LED dependent on the application. From simple binary switching to complex signal patterns, the driving circuits offer great variety in capability and complexity.

However, with a light transmitter alone, a communication system is not complete – a receiver is needed. There are many obsolete receptor devices for light, like photo tubes, selenium detectors, light-dependent resistors, etc., which will be left aside. State-of-the art light receptors are semiconductor-based – mostly silicon – either in the form of a photovoltaic cell for energy harvesting or a photodetector for signal applications. For the latter, a suitable amplifier type is also needed in order to reconstruct the data signals.

The following sections focus on these components, as the physical foundation of an up-to-date VLC system. All necessary components will be presented in adequate detail to enable further system modeling.

6.1 Light-Emitting Diodes

6.1.1 Electrical Characteristics

An LED is a semiconductor which consists of a pn junction as the term "diode" suggests. The photon emission is caused by recombination of electrons at the pn junction, where the

semiconductor material and its doping determine the energy of the photon and therefore the color of the emitted light. The achievable range reaches from infrared to ultraviolet light.

The electrical behavior can be modeled in two different ways, depending on the application. The direct current (DC) and low-frequency behavior are described by the large-signal model and the high-frequency behavior by the small-signal model [Hoe19].

6.1.1.1 Large-Signal Model

As an LED is a diode, the large-signal behavior can be modeled by the Shockley equation and its approximation [Wag31]

$$I_{\mathrm{f}} = I_{\mathrm{S}}(T) \cdot \left(\exp\left(\frac{V_{\mathrm{F}}}{n \cdot V_{\mathrm{T}}} \right) - 1 \right) \tag{6.1}$$

$$\approx I_{\mathrm{S}}(T) \cdot \exp\left(\frac{V_{\mathrm{F}}}{n \cdot V_{\mathrm{T}}} \right). \tag{6.2}$$

Compared to regular diodes, LEDs have a smaller reverse breakthrough voltage. A simpler model is depicted in Fig. 6.1 a), where a series circuit of a resistor $R_{\mathrm{S,D}}$, an ideal voltage source V_{D} for the forward voltage drop and an ideal diode is formed. In Fig. 6.1 b), the I-V diagram is given for the approximated Shockley model and the equivalent circuit model.

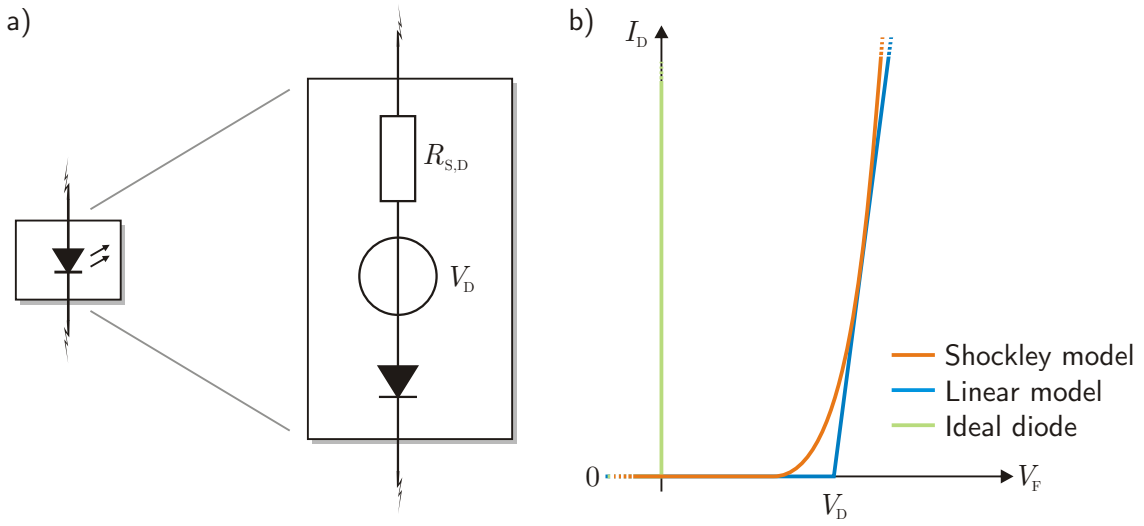

Figure 6.1: a) Linear equivalent circuit diagram; b) qualitative I-V diagrams.

6.1.1.2 Small-Signal Model

The dynamic small-signal model of a diode can be modeled as low-pass circuit. The main impact is caused by the junction capacitance C_{J}, which forms, together with the differential resistance R_{J}, a first-order low-pass circuit. The differential resistance $R_{\mathrm{S,D}}$ can be derived from the slope of the large-signal model at the desired working point.

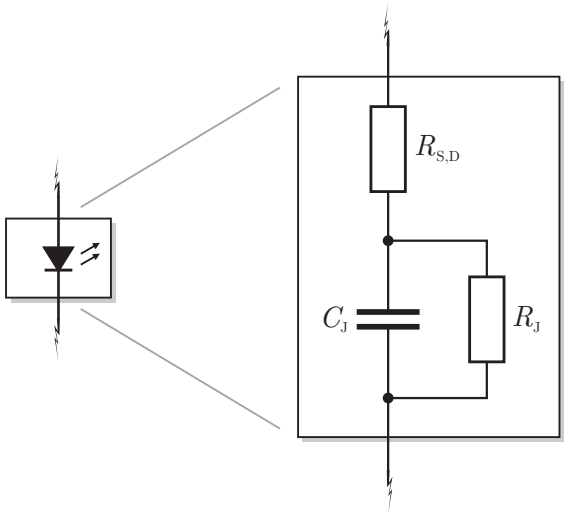

Figure 6.2: Equivalent circuit diagram for small-signal model.

6.1.2 Optical Characteristics

The radiation pattern of an LED depends mainly on its housing. There are two main types: i) LEDs with a lens-like plastic housing and ii) chip-on-board (COB) LEDs with a flat emitter surface. Hybrid types, such as COB LEDs with a lens mounted on top, also exist. The latest generation are chip-on-glass (COG) LED filaments, where many LEDs are mounted in series on a transparent glass or similar carrier and then coated with phosphor. Examples are shown in Fig. 6.3. LEDs with a plastic housing were the first commercially available LEDs. They were used for optical signaling and data transmission applications, mostly in the infrared region. In contrast, COB LEDs are used mainly for illumination purposes and are technically high efficient blue LEDs with a phosphor coating, which gets exited by the blue light and emits yellow light with a nearly continuous spectrum. Together with the blue light of the underlying LED, white light is created in total. In VLC applications, it might be beneficial to use a blue shortpass filter at the receiver because the phosphor produces an afterglow for flicker mitigation, which dramatically reduces the modulation

bandwidth [GL+07]. In most cases. they are consisted of many internal single LEDs to achieve a sufficient output power.

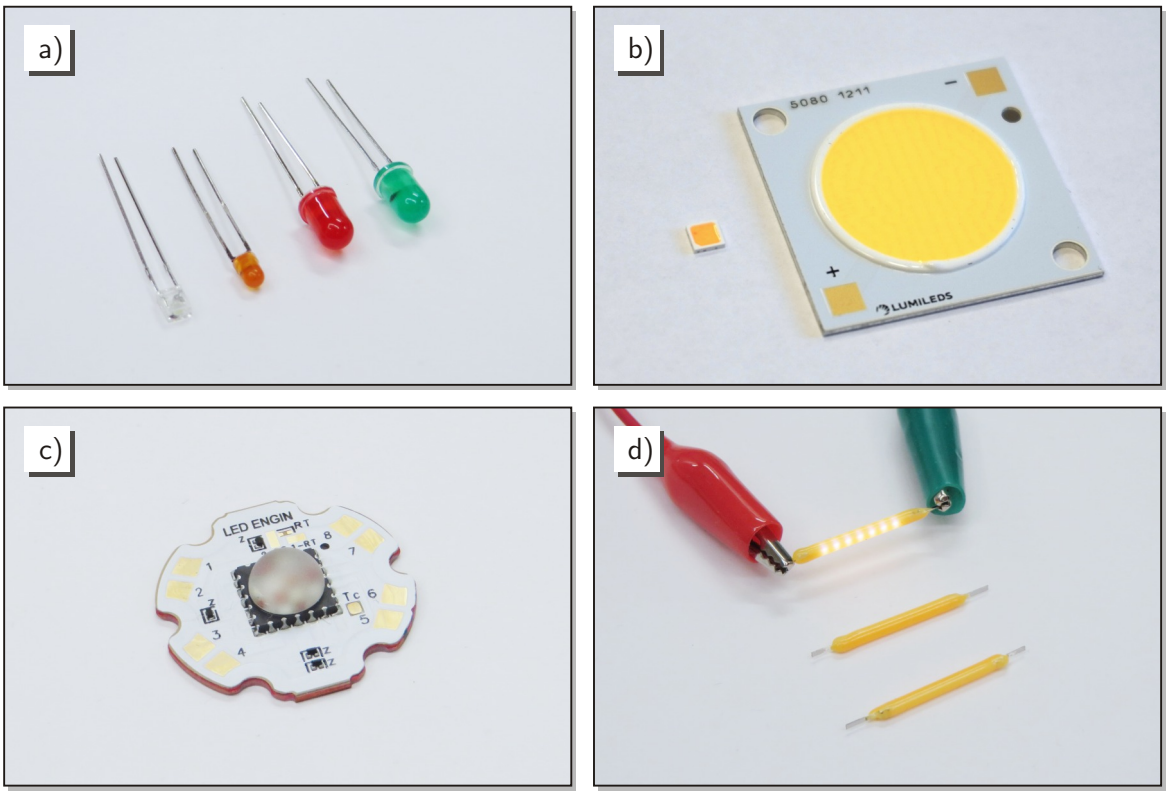

Figure 6.3: LED types: a) LEDs of different sizes and colors with plastic housing for signaling purposes, b) white-light COB LEDs of different sizes – the small LED emits warm-white light, while the large-area LED cold-white light. c) Multicolor COB LED with diffusor lens and star PCB for cooling and mounting, d) warm-white COG filament LEDs.

The angle of radiation is determined by the type of the housing and the internal structure, where phosphor COB LEDs have typically the widest angle of $\pm 60^\circ$ compared to other types with directed emittance. The radiation pattern can be modeled as generalized Lambertian emitter [GB79]. LED filaments have a cylindrical radiation pattern along their center axes.

Colored LEDs without phosphor emitter have a relatively narrow emission spectrum with spectral linewidths of about 20 nm to 35 nm. White light can be generated by mixing red, green and blue LEDs or by using a blue LED with phosphor coating, as mentioned before. In Fig. 6.4, examples are given for a multicolored LED and for a phosphorous one.

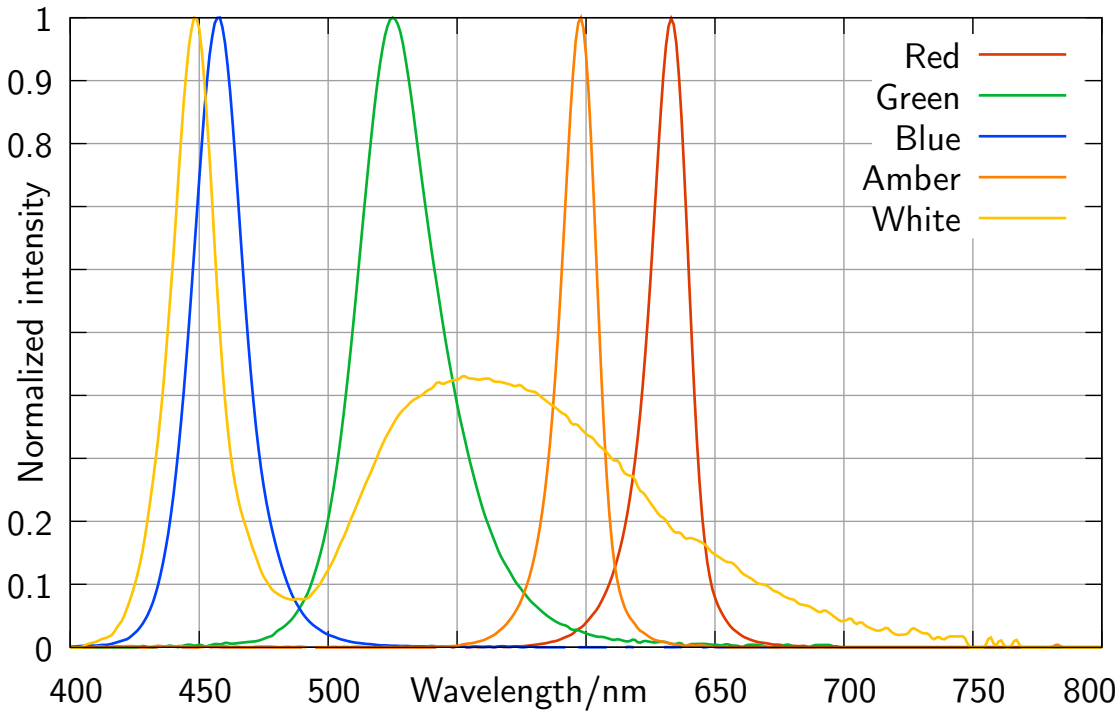

Figure 6.4: Normalized LED spectra of an Osram LED Engin LZC-B3MA07 (red, green, blue, amber) and Osram LED Engin LZC-03MD07 (white).

6.2 LED Driver Circuits

The non-linear I-V characteristics described in Part 6.1 require a suitable driving technology to achieve the desired light intensity emission.

As the LED characteristics indicate that a small voltage difference results in a large current change, the driver needs to limit the current. There are different ways of achieving this. Depending on the chosen solution, trade-offs exists between energy efficiency and other parameters like light quality. When there are additional requirements, such as varying the intensity of the light for data transmissions, trade-off effects increase. Adjusting the light intensity is required for dimming as well as for modulating the light source. So it is best to choose an adequate driver technology for the specific target application as the multiple driving circuits differ in complexity, efficiency and versatility.

6.2.1 Steady-State Operation

When it comes to lighting or signaling applications, the simplest way to drive an LED is using a series resistor as depicted in Fig. 6.5 a). This component works as current limiter,

so that the circuit can be used with common voltage sources like batteries or regular power supplies as long as they can deliver at least the required LED forward current. The principle is quite simple: As the LED forward voltage drop is limited to some material-defined value, the remaining voltage difference drops across the resistor. This results in a limited current defined by Ohm's law. The current that passes through the resistor is the same as the LED forward current because of the nature of the series circuit.

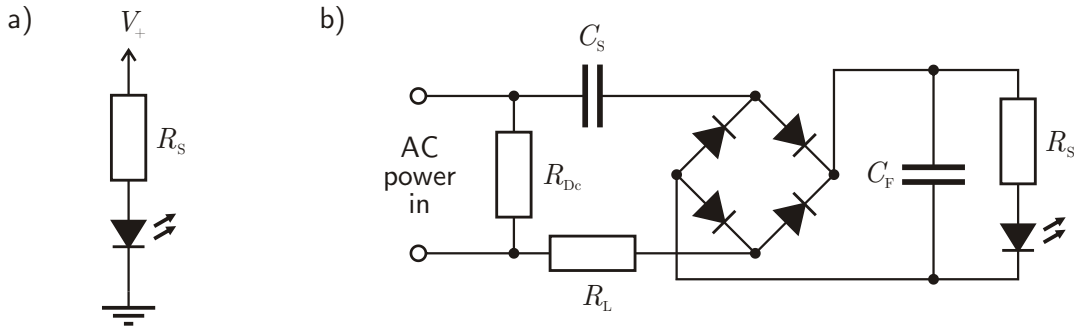

Figure 6.5: Steady-state LED drivers: a) Series circuit with resistor for DC power; b) Circuit with current-limiting capacitor for AC power.

Inherently, there is also a self-limiting control mechanism: When the LED voltage increases (and, consequently the forward current), the voltage over the resistor becomes smaller, which results in a lower series current. In other words, the LED is pinned to a fixed working point – effects like thermal drift ignored.

In terms of energy efficiency, the voltage drop over the resistor should be as small as possible because the current through the resistor causes thermal loss. This may not be so important in low-power applications like signaling LEDs with a few milli-Amperes in current, but in illumination applications, this loss is not negligible. The voltage of the power supply should be very close to the LED forward voltage, or multiple LEDs should be connected in a series circuit with only one common resistor to approach a given high supply voltage. For lighting-only applications without dimming, a current-limiting device with fewer loss could also be a capacitor C_S in combination with a full-bridge rectifier in alternating current (AC) circuits as shown in Fig. 6.5 b). Compared to DC, some additional components are needed: a filter capacitor C_F for smoothing the rectified current, a series resistor R_L for limiting the initial starting current caused by both capacitors and a high-resistance discharge resistor R_Dc for safety reasons [Reh03].

Another possibility would be using a current-limiting power supply instead of a voltage supply, so that no resistor is needed – but this would usually mean a more complex circuit for the power supply and, dependent on the type of the current-limiting circuit, the thermal

losses are shifted, yet not avoided. Parallel LEDs would need a dedicated current supply each.

6.2.2 Binary Switching

To extend the steady-state operation with intensity variation, a switch can be included in the circuit, so that the LED can be switched on and off in a fast, but controlled way. This can be achieved e.g. by a single transistor. Together with the series resistor, a simple and also dimmable LED driver is constructed as shown in Fig. 6.6 a). The average intensity can be changed by applying a binary control signal like a pulse-width modulated (PWM) signal, where the duty cycle, namely, the ratio between on and off state durations, defines the intensity [Hoe19].

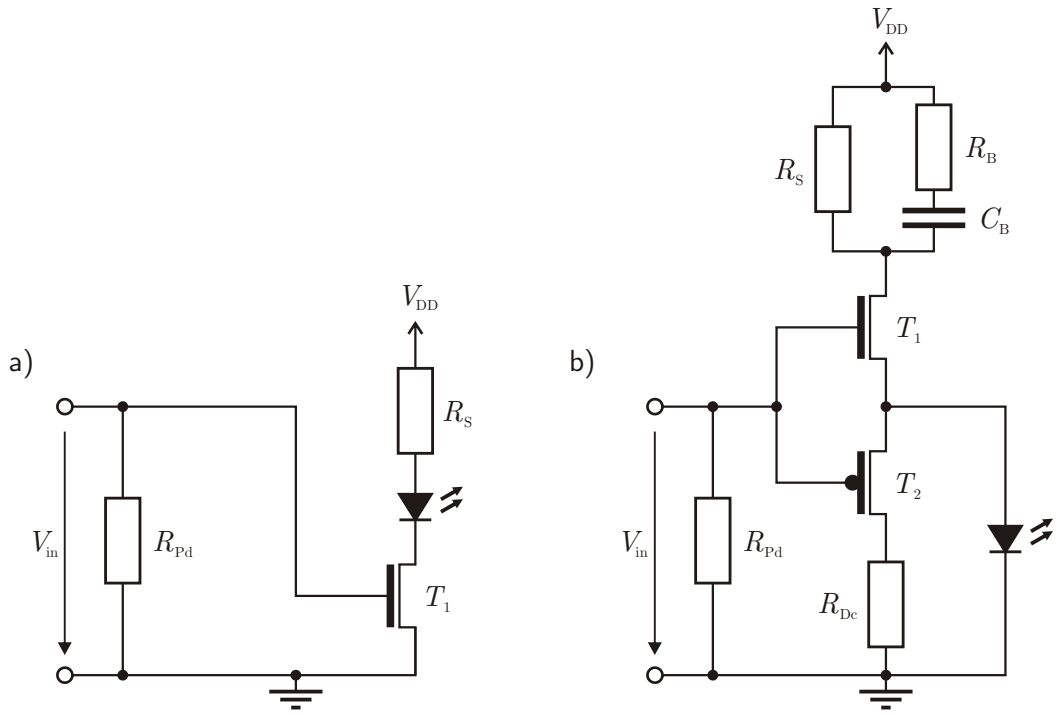

Figure 6.6: a) Single transistor; b) half bridge with optional boost circuit.

The switching frequency needs to be high enough to perceive the average light as flicker-free when used for illumination purposes. As the human eye recognizes flicker depending on different parameters like frequency, brightness, etc. [RR+12], the signal design is crucial here. Regarding energy efficiency, additional losses caused by the transistor add up: the higher the switching frequency, the higher the switching losses. While this loss can be

lowered by choosing high-quality fast transistors like MOSFETs or GaN transistors, there is an upper limit to the frequency caused by the internal junction capacitance C_{J} of the LED: the LED acts as low-pass filter and the capacity increases with the power of the LED.

When the LED is switched off, this capacitance discharges through the LED, which results in a slow decaying slope. In order to improve this behavior, the LED can be discharged actively by using a half-bridge circuit with two transistors as illustrated in Fig. 6.6 b). The discharge transistor is controlled by the inverted binary control signal and connects the LED actively to ground potential via R_{Dc}, so that the internal capacitance can discharge quickly. For a better switch-on slope, an additional boost capacitor C_{B} can be used.[1]

For data transmission, binary modulation schemes are suitable. Examples of these are OOK, also with Manchester coding, PWM, PPM and OCDMA.

6.2.3 Continuous Modulation

In some cases, analog-style modulation is desired which means that the signal amplitude can be changed continuously. As examples two methods are discussed: the most basic one, a linear amplifier, and the more advanced, a modulated buck converter, which promises a better efficiency in terms of power consumption. For the latter, a detailed parameter analysis is given.

6.2.3.1 Linear Amplifier with Bias Tee

A common approach is utilizing a linear amplifier with a bias tee when nearly arbitrary waveforms should be transmitted. Nearly arbitrary means that the non-negativity and real-value constraints for the overall driving current must kept in mind.

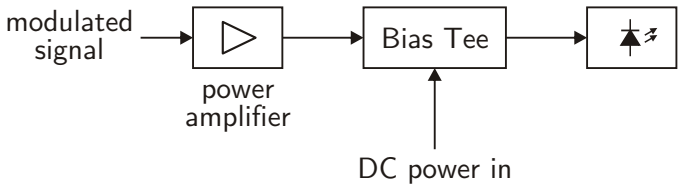

Figure 6.7: Schematic diagram of an LED driver consisting of a linear amplifier with bias tee.

In Fig. 6.7, the basic structure of this driver is sketched. The desired data signal is modulated, amplified, and added on top of a constant bias and then fed to the LED. This

[1] Regarding the energy efficiency and further applications of this circuit, see [FH18].

means that the absolute value of the amplified current needs to be smaller than the bias at all times to ensure that the driving current stays positive. Additionally, the allowed maximum current of the LED must also be respected.

With this type of driver, high modulation speeds can be achieved, but only with low modulation depths and the typical losses of linear amplifiers [VK+10]. In illumination systems, this can be seen as an advantage towards the light quality. When the data signal is equally distributed, i.e. with zero-mean, the average brightness of the light is not affected. Dimming could be realized quite easily, too – for changing the brightness, only the bias value needs to be adjusted, which does not effect the data signal. But regarding data transmission, a low modulation index results in a weak receive signal, while the bias itself causes at least shot noise. At the receiver end, the bias needs to be removed in order to get the data signal back. This can be done by choosing a suitable modulation scheme like an optical variant of OFDM, where the DC carrier can be neglected, or by using an additional high-pass filter.

6.2.3.2 Buck Converter

This part is based on publication [KH+18a].

To achieve a mostly continuous DC output signal from a varying voltage source, so-called buck converters (step-down converters) can be used, which are widely known in power electronics [Reh03]. A buck converter is a DC-DC power converter that transforms an input voltage V_{in} to a lower output voltage V_{out}. The output voltage can be set by an external signal. Therefore, a binary high-frequency control signal, e.g. a PWM signal, is used for operating the switching element in the circuit, which repetitively recharges an energy-storage component like an inductance or a capacitor. The output signal is basically averaged as they are working as a low-pass filter, similar to a highly efficient class-D amplifier. The switching transistor of the converter ideally avoids semi-conductive states during operation, and hence the overall efficiency is significantly improved compared to linear amplifiers. A bias tee is not necessary.

This principle can also be used for driving an LED as proposed in [Gon+16]: The former single transistor switch is replaced with a buck converter, and the binary control signal is generated based on the desired dimming level or data signal, which should be transmitted. The cut-off frequency of the low-pass filter design needs to be higher than the data signal bandwidth, but lower than the switching frequency of the control signal. The main drawback of this circuit is obvious: The switching frequency needs to be much higher than the bandwidth of the data signal in terms of oversampling, which is why expensive

high-speed components are required for realizing this driver. As stated before, switching losses also increase as stated before.

In some scenarios, it may be possible to use the internal capacitance of the LED as part of the intended low-pass filter, but this is beyond of scope in this work. For the interested reader, an extensive performance analysis of an LED buck driver is done in [Den18].

In addition to binary modulation techniques as in [SS+19], schemes with an analog-style signal can be used in such a system, as shown in [KH+18a]. Transmitting a multicarrier signal like DMT or other real-valued OFDM variants is therefore possible. Using a buck converter as modulator is a pure transmitter-side technique. Consequently, a conventional optical receiver and demodulator can be used.

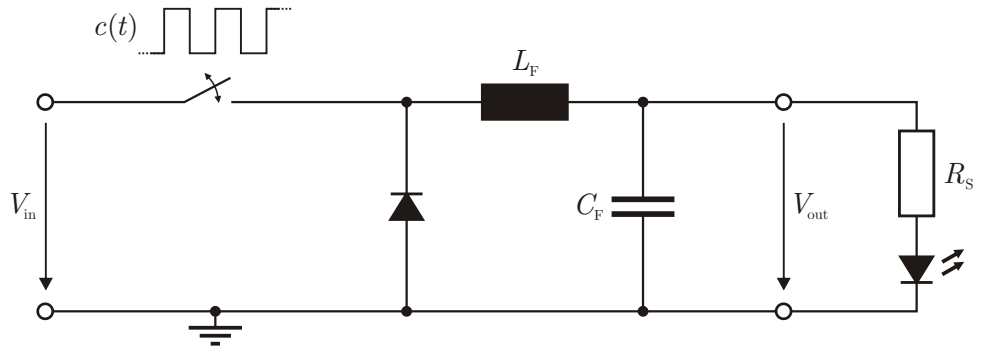

Figure 6.8: Schematic of a basic buck converter circuit.

To understand how the circuit can be used for modulating an LED, the working principle is briefly covered here. Since a buck converter is a kind of charge pump, it is a combination of active and passive parts as shown in Fig. 6.8. There is a switching device – usually a transistor – a series inductance L_F, a parallel capacitor C_F and a valve, which can be realized either by a diode or another anti-cyclic switched transistor for a faster circuit response [Gon+16]. The main transistor permits or interrupts a current flow from the power supply to the load. The average output voltage is controlled by the duty cycle D of the switching signal by means of $V_\mathrm{out} = D \cdot V_\mathrm{in}$. Depending on the switch state, two different ways of current flow can be distinguished: i) When the switch is closed, the current flowing to the load is limited by the inductance, which is being charged. The output voltage and consequently the voltage over the capacitor increases over time until both elements are fully charged or the switch state will change. ii) When the switch opens, the inductance as well as the capacitance discharge over the load as the diode is now in forward direction. The output voltage decreases until both elements are depleted or the switch closes again.

These alternating charge and discharge processes result in a more or less constant output voltage. In power applications, D is usually fixed, but can be changed to other (constant) values when dimming is demanded for e.g. lighting applications. The emitted light is of high quality. No flicker (neglecting remaining ripple) nor any other discontinuity is present.

In order to modulate the output voltage, the duty cycle D is transformed into a time-varying duty cycle $D(t)$, where the data is encoded within in the time domain. A suitable method for doing so is using PWM, where the amplitude of an arbitrary (data) signal is encoded into pulses with different duration but constant amplitude. The maximum data rate is determined by the oversampling factor and the cut-off frequency of the filter circuit f_c, which is given by Thomson's equation

$$f_c = \frac{1}{2\pi\sqrt{L_\mathrm{F} C_\mathrm{F}}}. \tag{6.3}$$

6.2.3.2.1 Pre-Distortion Current Control So far, the buck converter has been used as voltage source, which is why a current control needs to be established. For driving an LED, a series resistor can be used like before, but with high modulation depths, the LED non-linearity needs to be handled in this case, too. The output voltage depends directly on the control signal, so that a pre-distortion can be used. As an LED needs to be current-driven, the control signal must be pre-distorted with the inverse I-V curve of the specific LED. Some constraints of the buck converter itself need to be taken into account to ensure a continuous current mode (CCM) with the aim that the output current is never zero.

6.2.3.2.2 PWM Control Signal Generation For generating the control signal $c(t)$, the data signal $s(t)$ needs to be biased in order to remove negative amplitudes and is then normalized. This signal is called $s(t)_\mathrm{Bias}$ and compared to a saw-tooth signal $s(t)_\mathrm{Sawtooth}$ in terms of a 1-bit conversion. The amplitude of $c(t)$ is either 1, if $s(t)_\mathrm{Bias}$ is larger than $s(t)_\mathrm{Sawtooth}$ or otherwise 0. By doing so, the amplitude information is now stored in the pulse lengths. Fig. 6.9 illustrates this procedure.

$$c(t) = \begin{cases} 1 & : s(t)_\mathrm{Bias} > s(t)_\mathrm{Sawtooth} \\ 0 & : \text{else} \end{cases} \tag{6.4}$$

$$s(t)_\mathrm{Sawtooth} = [t \cdot f_\mathrm{Sawtooth}] \mod 1, \tag{6.5}$$

For a numerical simulation of a modulated buck converter circuit, the PWM signal in

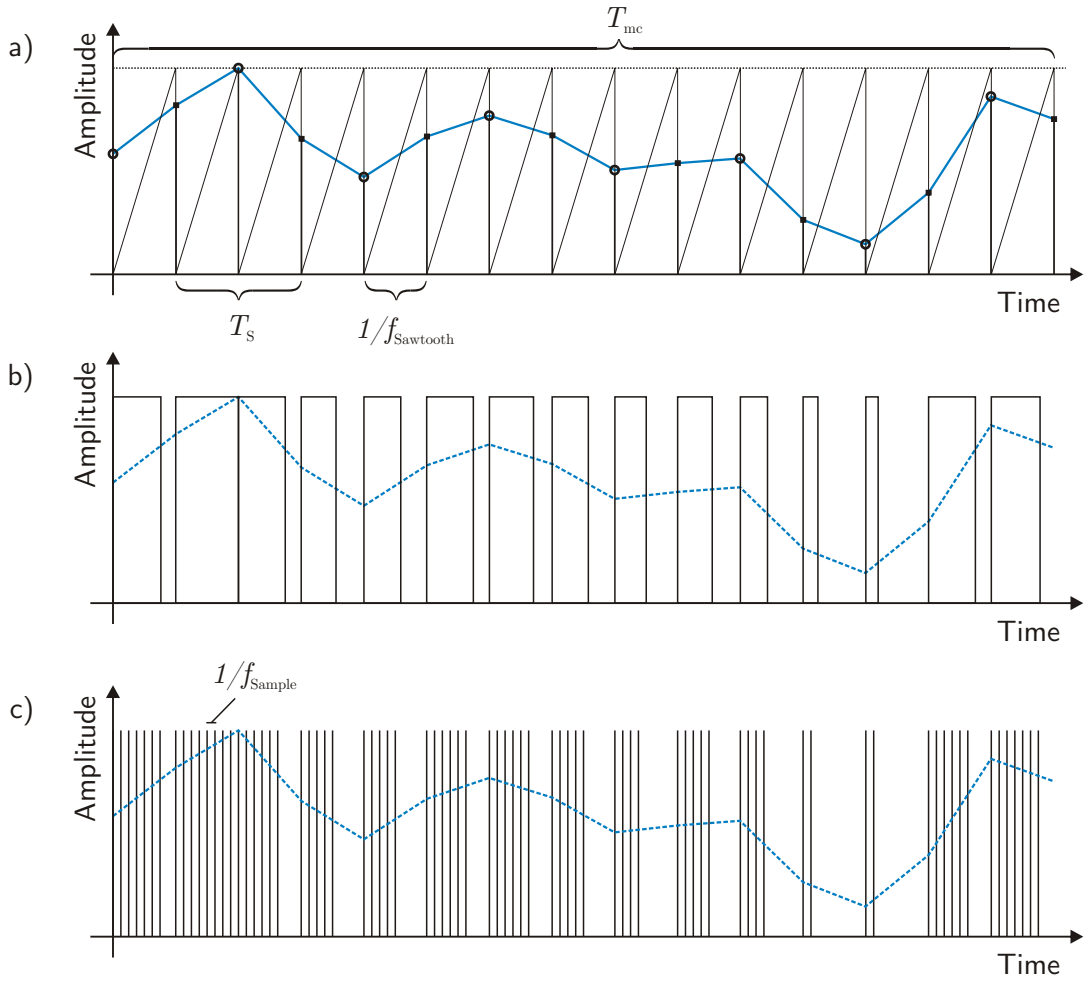

Figure 6.9: PWM oversampling: The blue signal in a) gets sampled to the PWM signal in b). In c), the oversampled version is shown [KH+18a].

Fig. 6.9 b) needs to be quantized in terms of oversampling as shown in Fig. 6.9 c). Thus, the oversampling factor and therefore the time resolution, too, impact directly the amplitude resolution of the source signal representation. With an oversampling factor of e.g. 32, the achievable amplitude resolution is limited to 5 bit.

6.2.3.3 Analysis of DMT Modulation with Buck Converter

This part is based on publication [KH+18a].

For further analysis of this circuit, a numerical simulation is performed with discrete-multitone transmission (DMT) as chosen modulation scheme. It is used here to illustrate the transmission process of (nearly) arbitrary waveforms. DMT is a real-valued variant of the well-known orthogonal-frequency division multiplexing (OFDM) scheme, which is

why the amplitude quality of the output signal is crucial. Distortions and noise are caused by several effects: clipping, PWM transformation, pulse quantization and the load itself [EM+10].

6.2.3.3.1 Simulation Model Overview The effect of the system parameters as the oversampling factor of DMT, symbol duration T_{mc} and different types of load on the BER is analyzed. The oversampling factor is varied between 32, 64 and 128. An LED load is assumed with and without predistortion as decribed above, while an Ohmic load is used as reference. The complete block diagram of the simulation with all modifications to the buck converter circuit is given in Fig. 6.10. As stated before, using a transistor instead of a diode as valve, the circuit becomes more responsive. This modification is therefore adapted here.

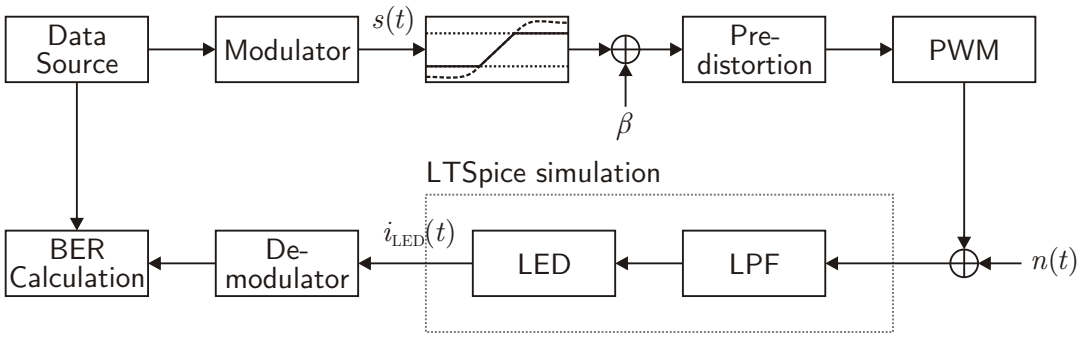

Figure 6.10: Numerical simulation and evaluation model of the LED buck driver, based on [KH+18a].

The test data is generated by a pseudo-random bit source implemented in Python and then DMT-modulated as described in the next paragraph. The modulated signal is clipped and biased to fulfill the requirements of limited power and non-negativity. Afterwards, the V-I predistortion is applied and the PWM control signal with the embedded data signal is generated. A buck converter circuit with load is simulated in *LTSpice* – a circuit simulation software – and the previously generated PWM signal is imported into the circuit. The resulting output current through the load is read by a Python script in order to demodulate the signal and to compute the BER.

6.2.3.3.2 DMT with Bias and Clipping DMT is realized by using the inverse fast Fourier transform (IFFT) with the order $N_{\mathrm{IFFT}} = 128$, resulting in $N_{\mathrm{IFFT}}/2 - 1 = 63$ usable subcarriers due to Hermitian symmetry and DC biasing. The modulation format is

16-QAM for the active subcarriers. Seven subcarriers are used for pilot tones for channel estimation, which are equally distributed among the subcarriers. The receiver uses the information of the pilot carriers to calculate the correction factors – the inverse of the estimated channel gain – over all carriers. This results in non-white noise when looking at the multicarrier symbol, as subcarriers near the cut-off frequency f_c will be increased more and, consequently, the noise of these carriers. But for a single, isolated carrier, the noise can be still assumed as white. In this implementation, neither bitloading nor a cyclic prefix is applied because this would spoil the observation of the buck converter effects.

As DMT or OFDM in are generally prone to a high peak-to-average power ratio (PAPR), clipping is applied. To get a reasonable preservation of the signal amplitude, the clipping level is set to 2σ, where σ is the standard deviation of the signal. In this way, approximately 95.4 $\%$ of the amplitude values are preserved. The resulting clipping noise variance is about 0.013 [DS$^+$12].

6.2.3.3.3 Simulation Results The simulation results in Fig. 6.11 show two main aspects: First, the non-linear behavior of the LED exerts an impact on the BER. With signal pre-distortion, at modulation depth of 100 $\%$, a BER of $1 \cdot 10^{-4}$ given a data rate of 11 Mbps per single channel can be achieved, which is below the forward error correction (FEC) limit. Without this pre-distortion, it is not possible to obtain a BER any better than 10^{-2} in this scenario. Second, there is an optimal working point for the switching frequency, which is determined by the ratio of the sawtooth frequency and the symbol duration – probably caused by resonance effects in the circuit.

To reduce the BER error floor or to increase the achievable data rate one could implement modifications known from OFDM systems like bit loading, using a cyclic prefix or adapting different OFDM variants like asymmetrically clipped optical OFDM (ACO-OFDM) or even single carrier schemes like carrierless amplitude phase (CAP) modulation. Irrespective of the modulation format, there is also the possibility of employing a control loop via the load resistor R to minimize the difference between input waveform and output waveform.

6.2.4 Discrete-Step Amplitude Variation

This part is based on the publication [KH$^+$20].

Motivated by the great hardware requirements for the buck converter and the limited modulation ability of the binary switching driver, a compromise version is suggested. This driver is able to generate a set of different amplitudes without the need for complex hardware. Several parallel resistors are used, which can be switched on and off, each by an

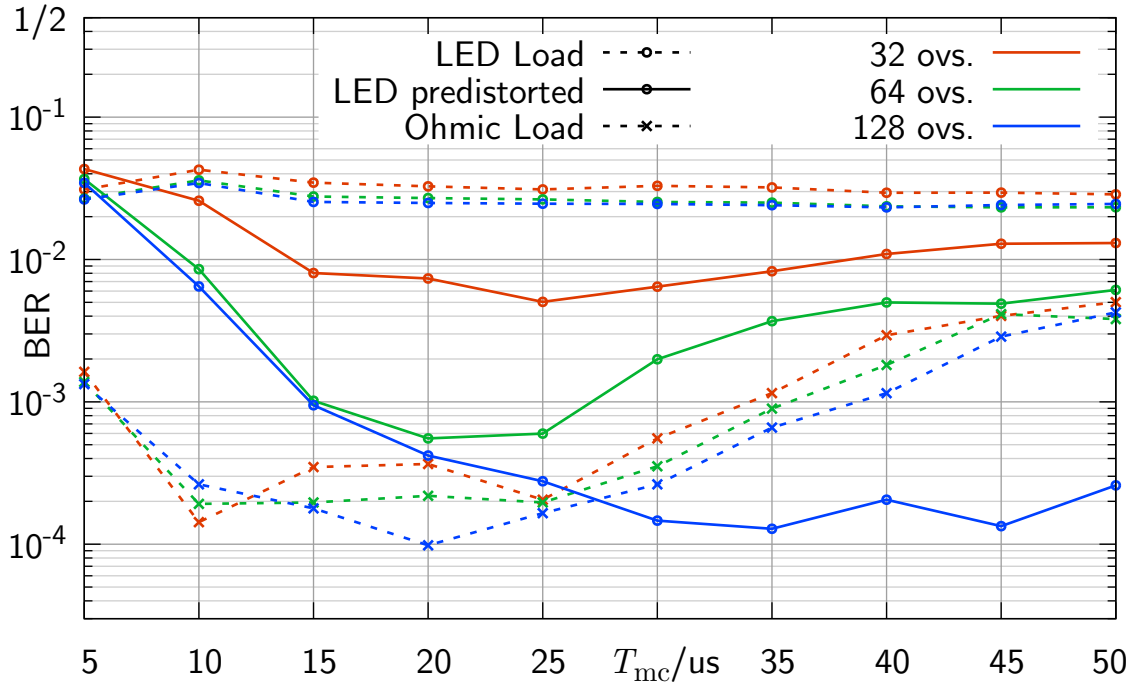

Figure 6.11: Numerical simulation results of the LED buck driver.

individual transistor. Different total resistance values can thus be achieved – each value creates a different LED forward current, which leads to different light intensity, too. The basic schematic is shown in Fig. 6.12 and illustrates the concept. The individual resistor values must to be chosen in such a way that they form a mathematical geometric series, i.e. $R_0 = 2R_1 = 4R_2 = 8R_3 = \ldots = 2^{N-1}R_{N-1}$. The sum value R_{total} of all resistors should limit the forward current to the allowed LED maximum current $I_{\text{f,LED}}$:

$$\begin{aligned} R_{\text{total}} &= \frac{1}{\frac{1}{R_0} + \frac{1}{R_1} + \frac{1}{R_2} + \ldots + \frac{1}{R_{N-1}}} \\ &= \frac{1}{\frac{1}{R_0} + \frac{2}{R_0} + \frac{4}{R_0} + \ldots + \frac{2^{N-1}}{R_0}} \\ &= \frac{R_0}{1 + 2 + 4 + \ldots + 2^{N-1}} \\ &= R_0 \sum_{k=0}^{N-1} \left(\frac{1}{2}\right)^k \\ &= \frac{V_0 - V_f}{I_{\text{f,LED}}}. \end{aligned} \tag{6.6}$$

In total, 2^N different intensity amplitude levels can be achieved with N parallel resistors. However, as the LED is non-linear, the achievable corresponding step size in the light intensity is not equally distributed. In terms of flicker and ripple, the light is of high quality compared to the buck converter and the binary switching driver as it is steady.

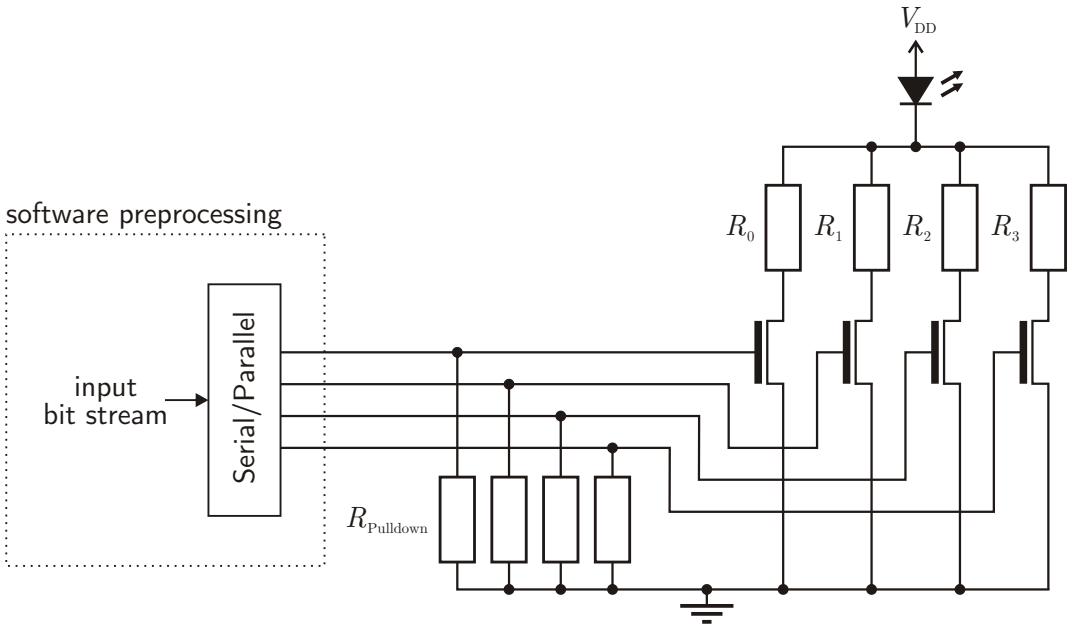

Figure 6.12: Schematic of a discrete-step driver for PAM-4, based on [KH+20].

Another way of creating PAM-4 symbols is to use a high-frequency PWM generator. In this case, the amplitude level is determined by the PWM duty cycle, hence, the average level corresponds to the modulated data symbol. This method is more suited for communication systems with low-data rates than for high-speed ones, because the PWM frequency needs to be much higher than the sample rate at the receiver, which might be technically challenging. A suitable application is LED-to-camera transmission. Here, the frame rates of cameras are low, typically in the range of tens to hundreds of frames per second.

6.2.4.1 Experimental Analysis of a Discrete-Step Driver

This part is based on the publication [KH+20].

For evaluation, a $N = 4$ resistors hardware example of the driver in Fig. 6.12 is examined with different baud rates between 1 Mbaud and 5 Mbaud. For modulation, AMI and RZ-OOK are used. The block diagram of the setup is given by Fig. 6.13: A 1 W warm-white LED with a forward current of 150 mA is placed 15 cm away from a Thorlabs PDA10A-EC photodetector with integrated amplifier. The mapped data signal is generated by a

Digilent Analog Discovery module, which controls directly the gate inputs of the switching transistors and also picks-up the amplified receiver voltage. After low-pass filtering the receive signal, the BER can be computed. The low-pass filter is second-order and its cut-off frequency set accordingly to the baud rate. The non-linearity of the LED is clearly visible in Fig. 6.14 a) next to the eye diagramm in b). Fig. 6.15 shows the impact of different data rates and dimming levels on the BER.

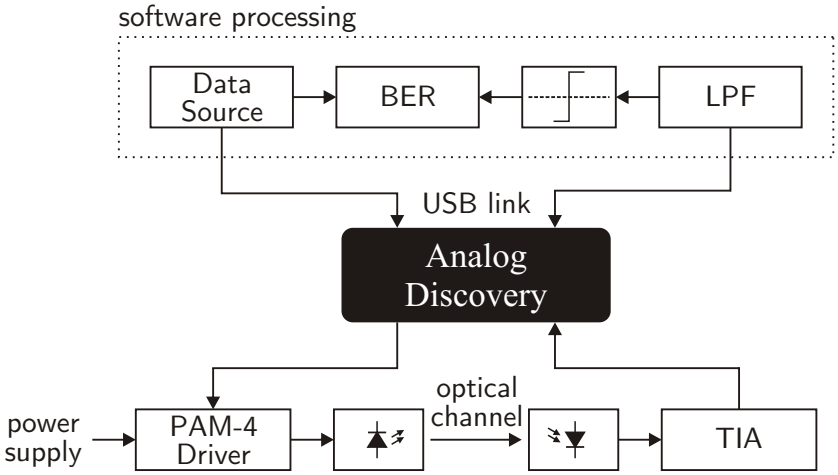

Figure 6.13: Discrete-step driver hardware example, based on [KH+20].

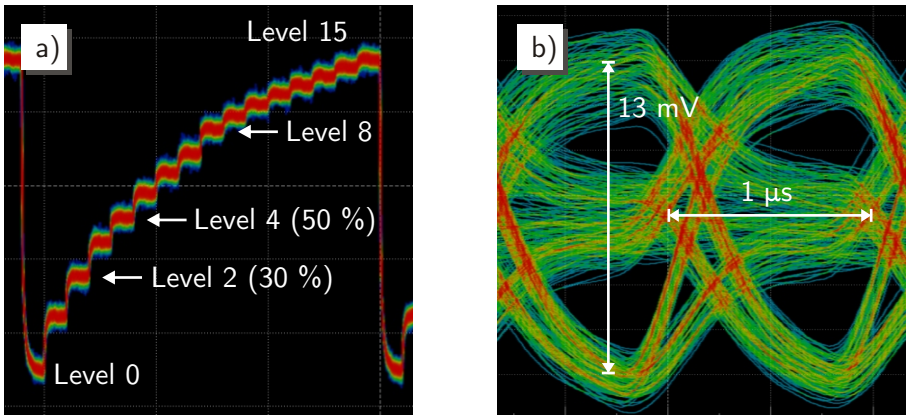

Figure 6.14: Discrete-step driver: a) non-linear amplitude level distribution; b) eye diagram at 1 MHz, based on [KH+20].

6.2.4.2 Experimental PAM-4 LED-to-Camera Transmission

The following results are presented in [KH+18b].

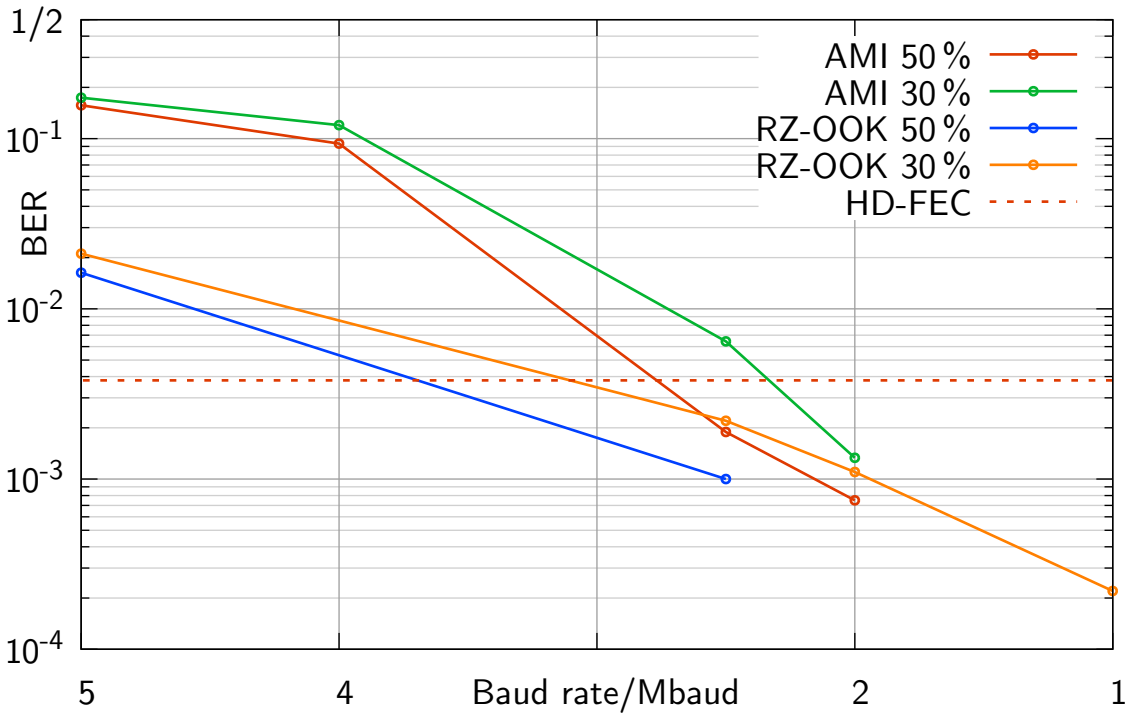

Figure 6.15: Discrete-step driver results.

For an experimental analysis of PWM generated PAM-4 symbols, an LED-to-camera transmission is established by using a Logitech HD Pro Webcam C920 and an off-the-shelf LED strip, which is operated at 9 V. At the transmitter side an Arduino microcontroller is used to generate PAM-4 symbols with the built-in PWM analog outputs for the blue and green channel and a clock signal for the red channel. The LEDs are switched by a BS170 NMOS transistor. The camera is placed 3 m away and connected to a computer where the video stream was analyzed with Python and openCV. The resolution is set to 1920×1080 pixels at a frame rate of 15 fps with an evaluated pixel area of 24×24 pixels. Due to the brightness saturation problem mentioned in Chapter 4.3.1, an anti-static foil is used a blur filter.

A training sequence and Gray coding are used and then a minimum-square-error decoder evaluated the selected video pixels for data rates between 100 bps and 33 bps. As there is cross-talk between the colors, the training sequence was transmitted twice - first with normal clock, then with inverted clock to cover all combinations a shown in Fig. 6.16.

The results in Fig. 6.17 show that a data rate higher than the frame rate can be reached with PAM-4 modulation as there are no errors below 44 bps.

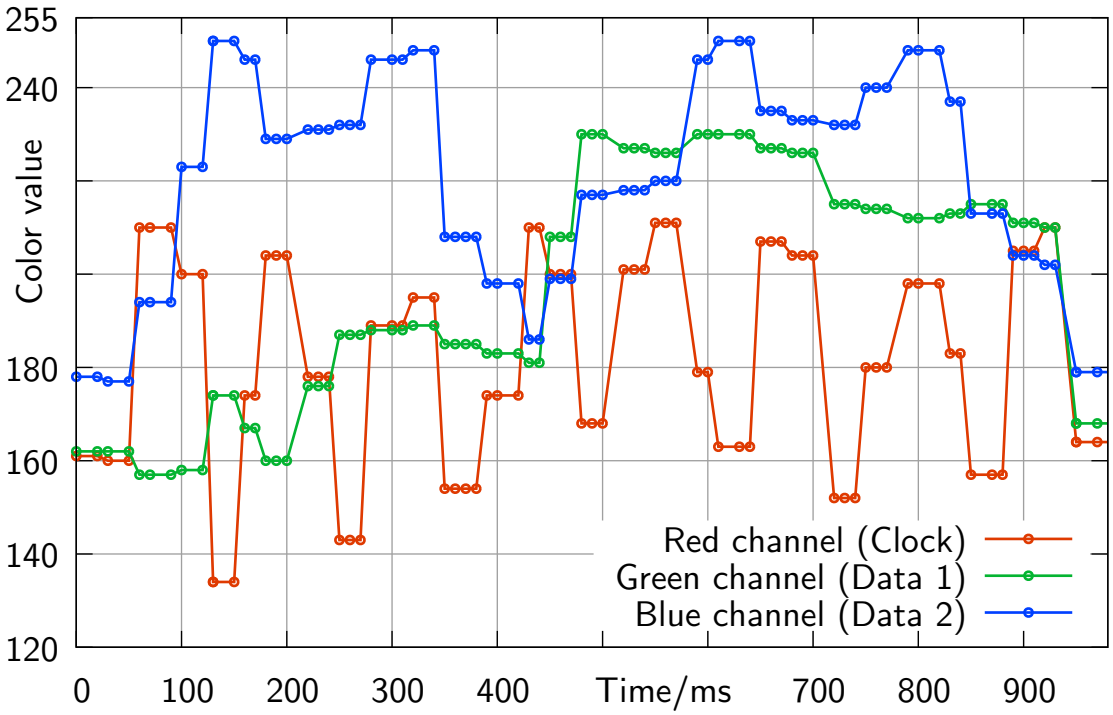

Figure 6.16: Training data sequences (blue and green channel) sent twice at 56 bps, first with regular clock (red), then with inverted clock.

6.3 LCD Filter

The following sections are based on publication [KF+19]. Variants of LCD filters are introduced and characterized experimentally.

6.3.1 Physical Composition

A single LC cell is a compound of at least three components: two polarization filters with a transparent conductive coating (mostly indium tin oxide (ITO)) and a liquid crystal material in between [Che11]. Incident light is polarized by the first filter and then the polarization is rotated by the liquid crystal molecules. Depending on the orientation of the second filter, the light can either pass – when it is orthogonal to the first one – or gets blocked when the two filters are in parallel. This is called either "normally white" when translucent or "normally black" in the other case. When a voltage is applied to the conductive coating of the polarization filters, the LC molecules untwist forced by the electric field and do not interfere with the light any longer. The behavior regarding the light inverts as indicated in Fig. 6.18: formerly blocked light can now pass. This principle

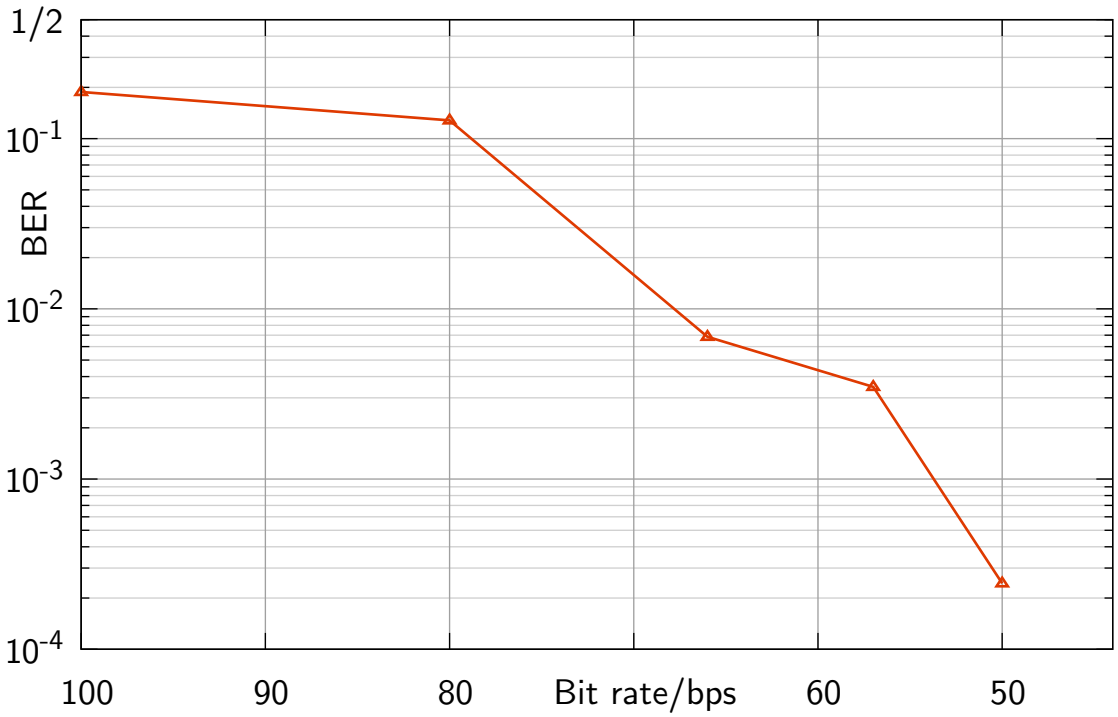

Figure 6.17: Bit-error rate for different data rates at 15 fps.

of light control causes significant transmission losses, even in transparent mode, as the polarization filters inherently reduce the incident light intensity.

In order to create an LCD, the area of one cell is divided into many sub-areas which can be switched individually. These sub-areas are known as pixels in display applications. The active area of one pixel is smaller than the full pixel size as address lanes and transistors need some space. In Fig. 6.19, a photo of a 3.5" off-the-shelf black-and-white display of the type Midas MCT035H6X240320PWL is shown under a microscope.

In the case of a color LCD, this problem intensifies even more: a single pixel is split into three sub-pixels with own address lanes each. The color filters cause additional losses. Fig. 6.20 shows a color LCD under a microscope.

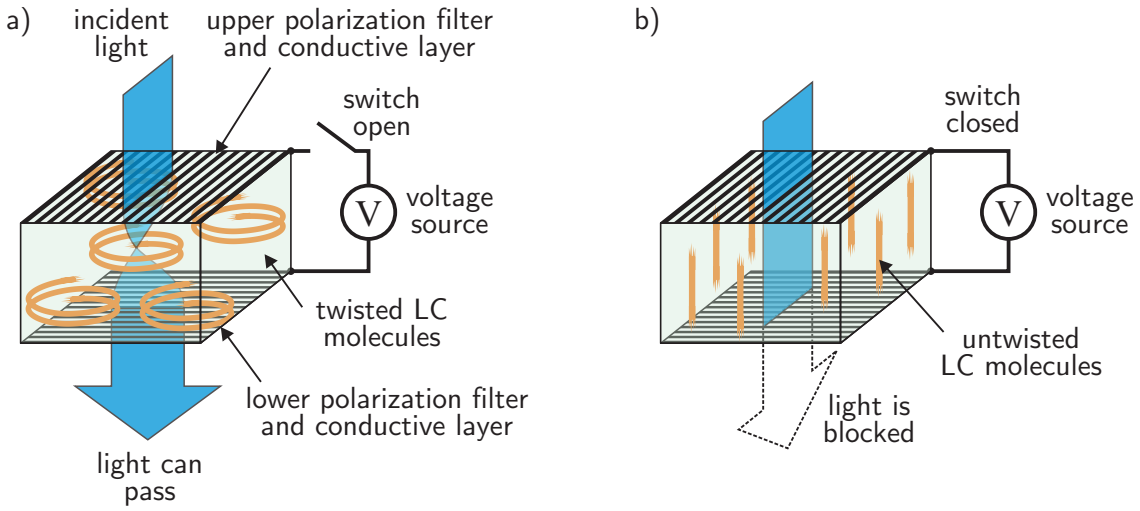

Figure 6.18: LC cell structure, based on [Che11].

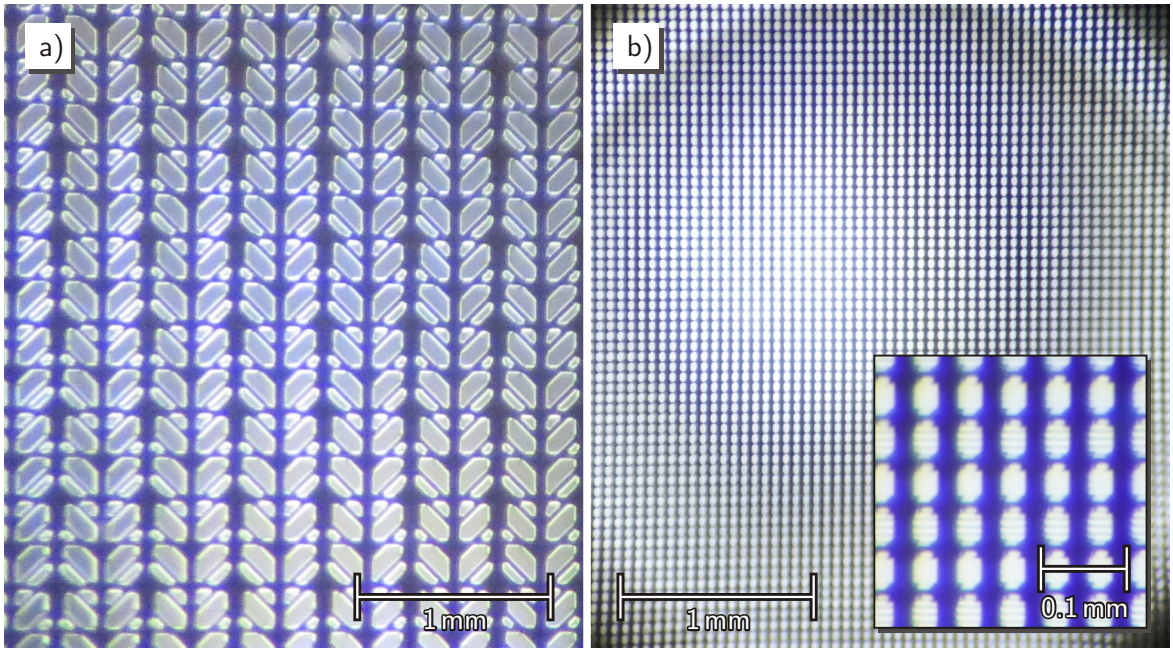

Figure 6.19: a) Microscopic view of Midas MCT035H6X240320PWL and b) ChiTu DXQ608-X04 at same scale with close-up view of the DXQ608-X04 pixels.

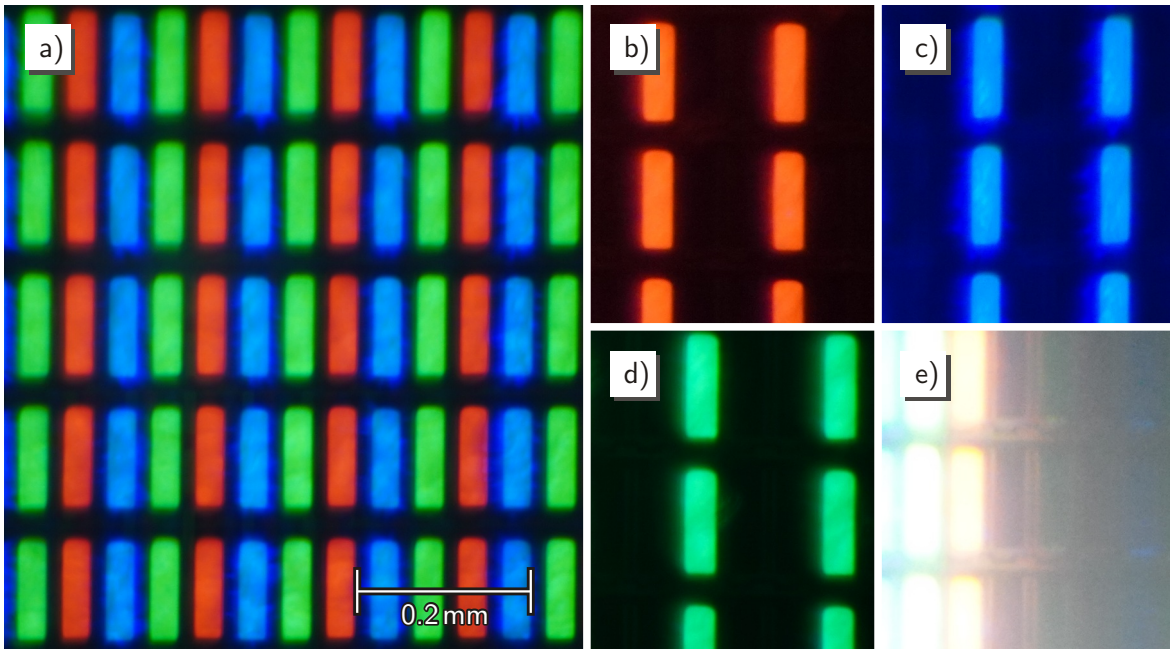

Figure 6.20: a) Microscopic view of Waveshare 3.5 RPI LCD switched to all white, b) red only, c) blue only and d) green only. e) Transition edge between white and black pixels.

6.3.2 Optical Characterization

In order to perform transmission simulations, the LC filter needs to be characterized in terms of optical properties and behavior. For this purpose, a single LC cell as well as a complete color LCD are evaluated in terms of light transmission and optical phenomena which can occur when used in a VLC system.

6.3.2.1 Single LC Cell

An LC cell from off-the-shelf welding-eye-protection glasses as shown in Fig. 6.21 is characterized in terms of transmission, dependent on the incident angle and the wavelength. For this purpose, the blue LED of a multicolored LED of type Osram LED Engin LZC-03MD07 is used as light source together with a Thorlabs PDA10A-EC photodetector. The LC cell is a normally white one and it is placed on a rotating frame. The cell is supplied with 10 V for switching to blocking mode and is put in a light-tight box as indicated in Fig. 6.22. To minimize reflections, the box is painted matte black at the inside. The resulting transmission factors are normalized to the received intensity without the LC cell along the path. The spectral response of the LC cell is measured with an spectrometer of type BTS256-EF made by Gigahertz-Optik GmbH and a white LED as light source. Here, the cell is placed over the sensor and the resulting spectral distribution is again normalized to the spectrum of the white LED. Figs. 6.23 and 6.24 present the transmission factors for the pass and blocking modes for the angular and wavelength dependency. In the Appendix C, the transmittance characteristics of differently colored LEDs are listed.

Regarding the spectral properties, it should be noted that the blocking ability of the LC cell decreases in the far-red to infrared region of the light spectrum. When a white phosphor LED is used without blue filter, an additional filter which cancels at least the infrared portion could improve the performance. Such an infrared filter was also used in the original welding protection glasses.

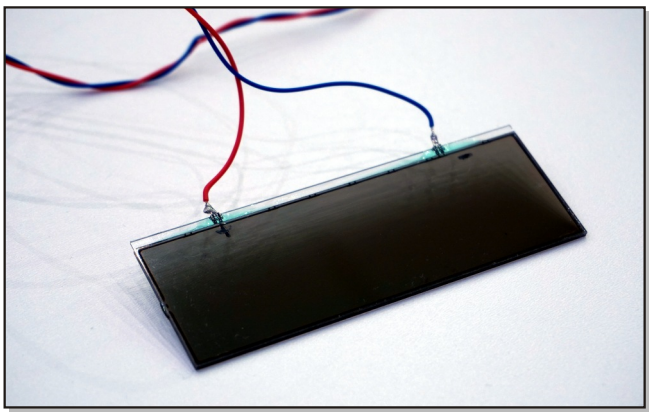

Figure 6.21: Single LC cell, taken from an automatic eye-protector for welding.

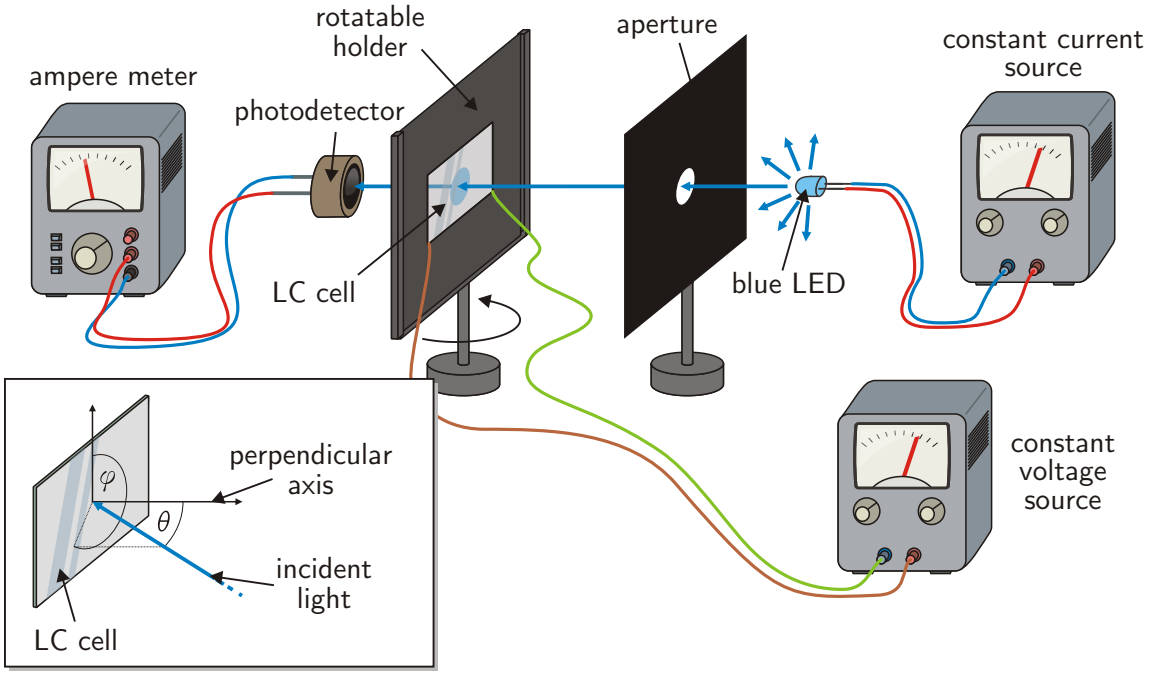

Figure 6.22: LC cell characterization setup for angular-dependent transmission factors, based on [KF+19].

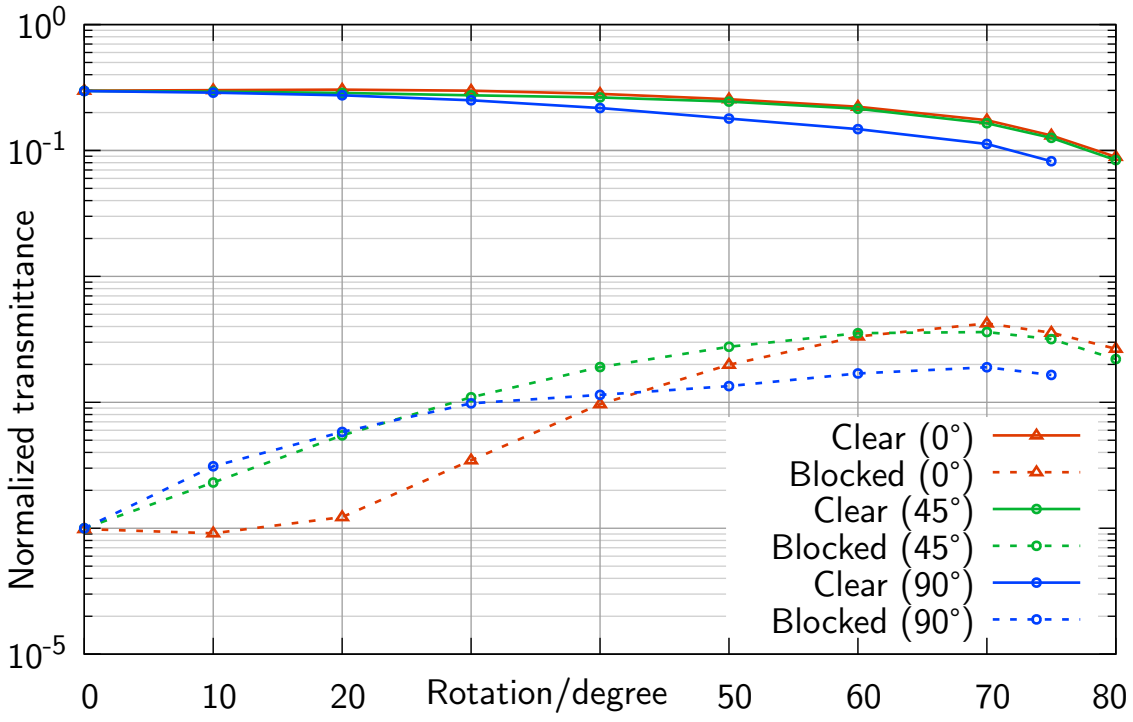

Figure 6.23: Angular-dependent transmission factor of single LC cell.

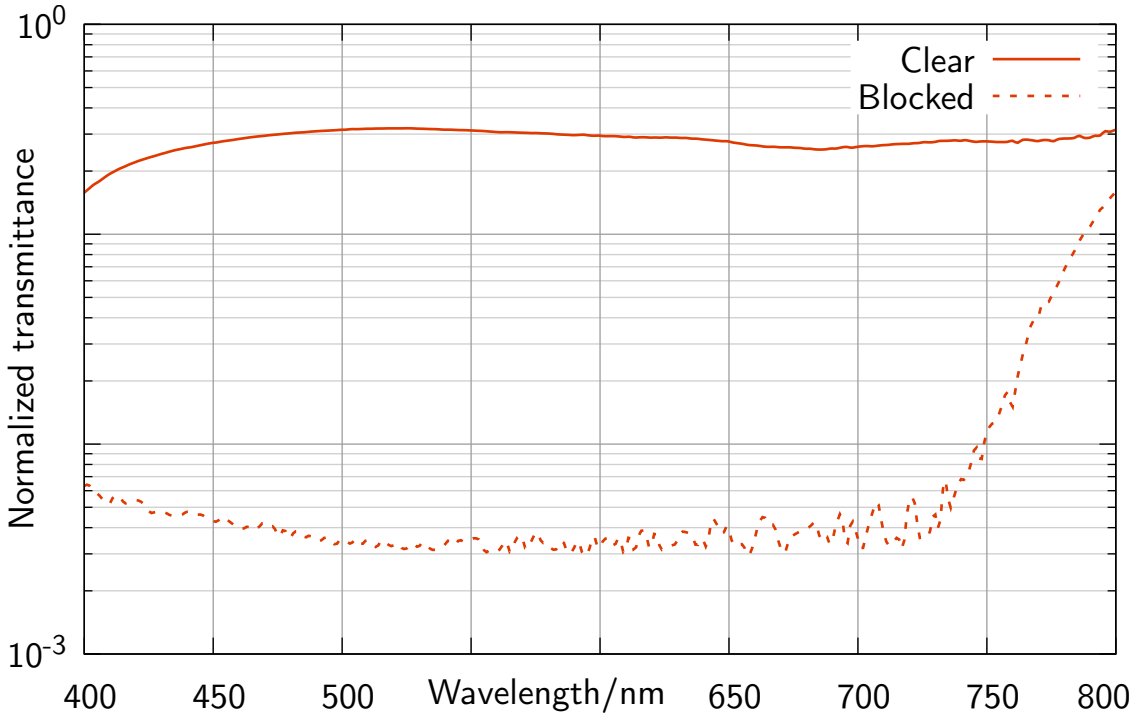

Figure 6.24: Wavelength-dependent transmission factor of single LC cell.

6.3.2.2 LCD Color and Monochrome Displays

Regarding the characteristics of a regular LCD, the backlights of a color Waveshare RPI LCD and a monochrome Sharp DXQ608-X04 were removed, so that only the bare LCDs remain. As in the case for the single LC cell, the transmission characteristics are measured, but in a slightly different setup. Only the boresight incident angle is evaluated. A Lumileds Luxeon L2C5-50801211E1900 LED is used, which offers a spectral distribution of light approximately between 420 nm and 750 nm. In Fig. 6.25, the wavelength-dependent transmission factors for full-white and full-black displays are shown. For the case of the color LCD, the transmission factors for only red, green and blue pixels are shown, too. As mentioned before, the pixel arrangement results in a higher loss compared to the single LC cell. Due to the low light intensity in the lower and upper region of the spectrum, the transmission measurements are here especially prone to noise. Additionally, the method of measurement influences the spectral distribution results: The overall brightness defines the integration time of the sensor, which means that incident light with a high intensity spectral portion and a low intensity portion, like colored light, gets received with a different integration time than low-intensity light with a flat spectral distribution. Because the accuracy of the measurement varies with the integration time of the sensor, phenomenons like the low part of the blue or green spectral transmittance gets below the blocking transmittance in Fig. 6.25 appear.

6.3.2.3 Aberration Errors

The higher the resolution of an LCD, the greater the pixel density and the smaller the structures. For modern LCDs with high-definition resolution and high pixel density, this structure size is in the micrometer range and thus approaching the wavelength of visible light. In a typical display application, this matter is not of concern, but when used as LCD filter in the presented VLC application, one should be at least aware of it. The LCD pixel grid, with its integrated transistors, address lanes and active area, behaves like a diffraction grating where the light is diffracted into a rainbow-like color spectrum, as illustrated in Fig. 6.26. This effect increases with the distance between LCD and photodetector or light source. Consequently, the shadow, which is cast by the aperture, has no sharp edge, but is blurry. As in a real world application, the distance to the photodetector is kept short, the width of the blurred edge is smaller in comparison with the photodetector size.

In a practical measurement, this results in smoothed edges when e.g. the already mentioned bar algorithm is used for detecting a light source. Fig. 6.27 shows the obtained

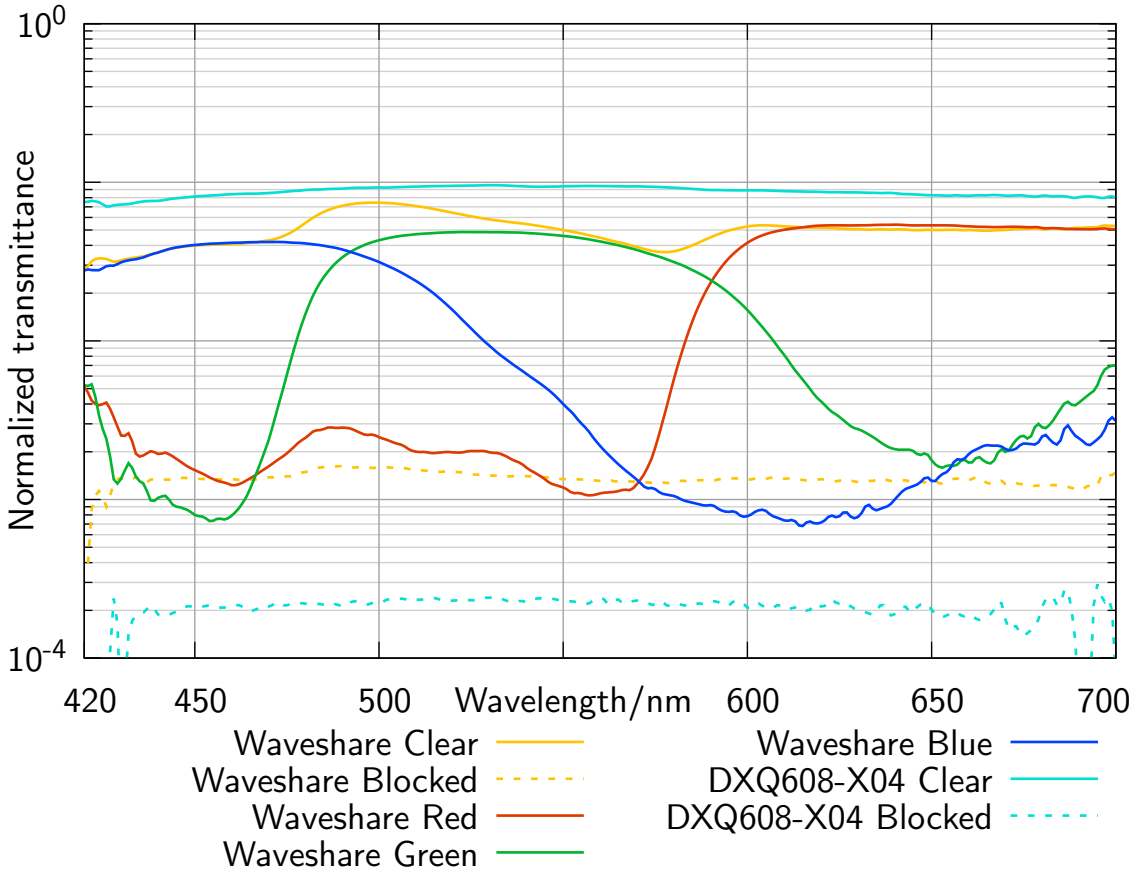

Figure 6.25: Wavelength-dependent transmission factors of a color and a monochrome LCD.

intensity using the receiver presented in Chapter 7.4 with two light sources. The bar width is set to the photodetector edge length and moved along the x direction of the LCD while one single LED is switched on. The smoothed beginning of the rising slope as well as the fading-out are visible.

Additional error contributions are reflections inside the receiver case due to not perfectly absorbing walls, reflections at the glass housing of the photodetector and the bottom side of the LCD, but also internally scattered reflections inside the LCD glass structure, which are also visible in Fig. 6.26 c). Moreover, a refraction occurs due to the non-zero thickness and higher refractive index of a real LCD. Here, the incident ray is refracted when entering the glass medium and also when exiting. Assuming the LCD behaves similarly to a plane-parallel glass pane, the overall incident angle is not changed, but its position is slightly different, as indicated in Fig. 6.28.

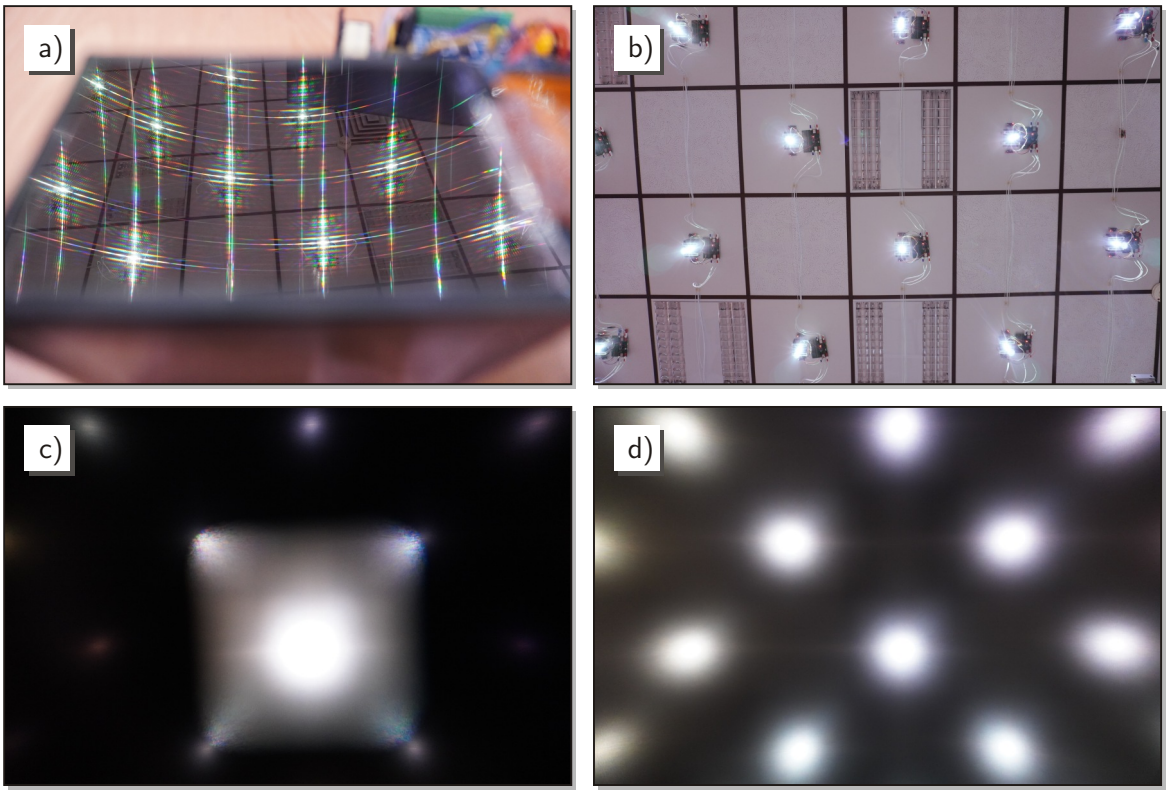

Figure 6.26: Spectral diffraction of light at a color LCD (Waveshare): a) reflected, b) ceiling view without LCD, c) see-through with LCD and white square area, d) see-through with all-white LCD.

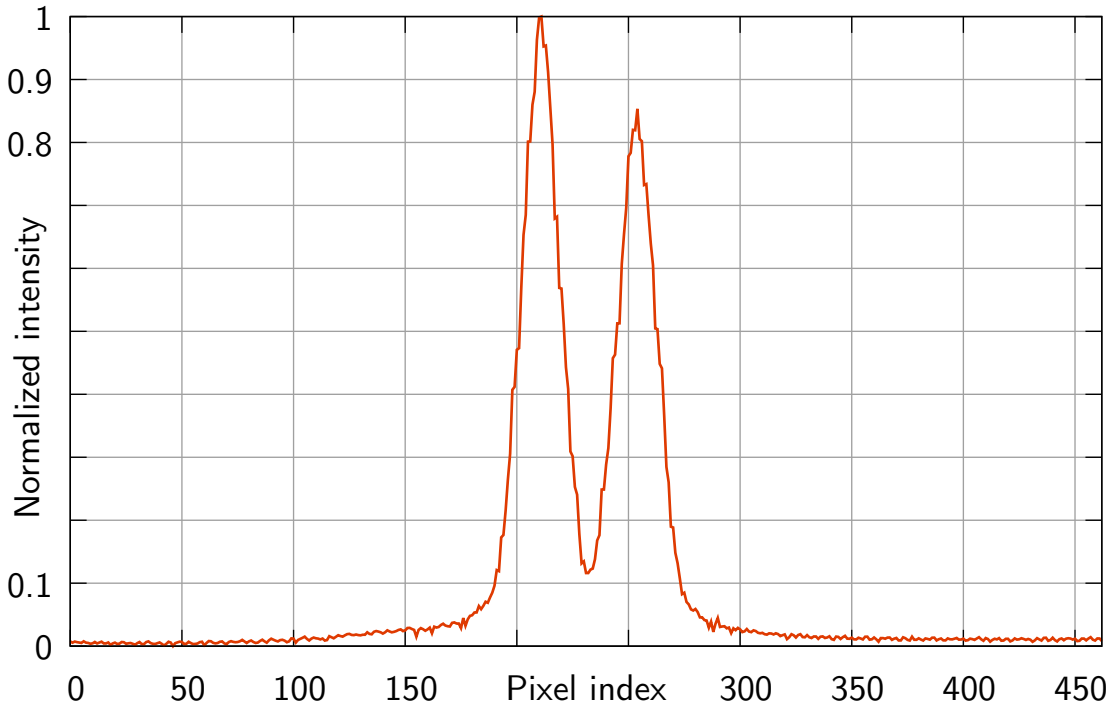

Figure 6.27: Smoothed transition at edges, caused by spectral diffraction and reflection of light at the LCD and housing.

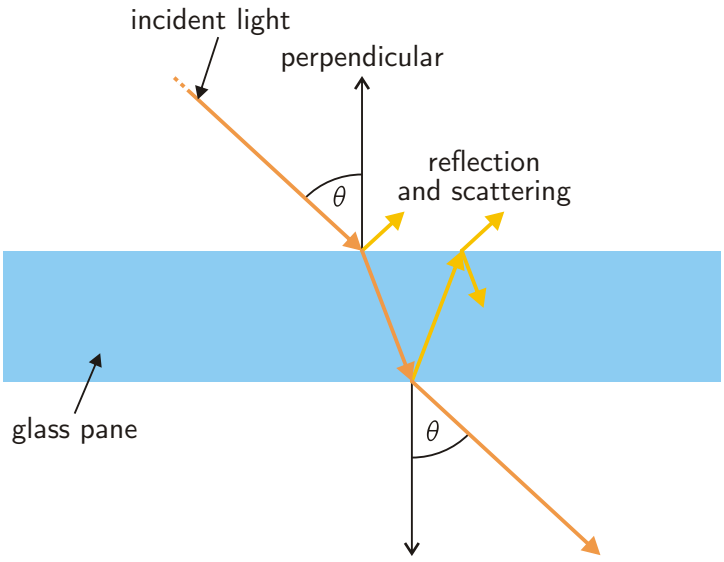

Figure 6.28: Refraction at a plane-parallel glass pane.

6.3.3 PDLC Foil

6.3.3.1 PDLC Technology and Filter Effect

Another similar LC variant is a polymer-dispersed liquid crystal (PDLC) foil, which is a composite of a polymer liquid crystal between two conductive transparent layers. It is commercially known as "smart glass" and is used as a decorative and functional element in architecture. In its normal state – the blocking mode – the foil diffuses light and prevents one from seeing through it. In "clear mode", the foil is transparent like regular glass.

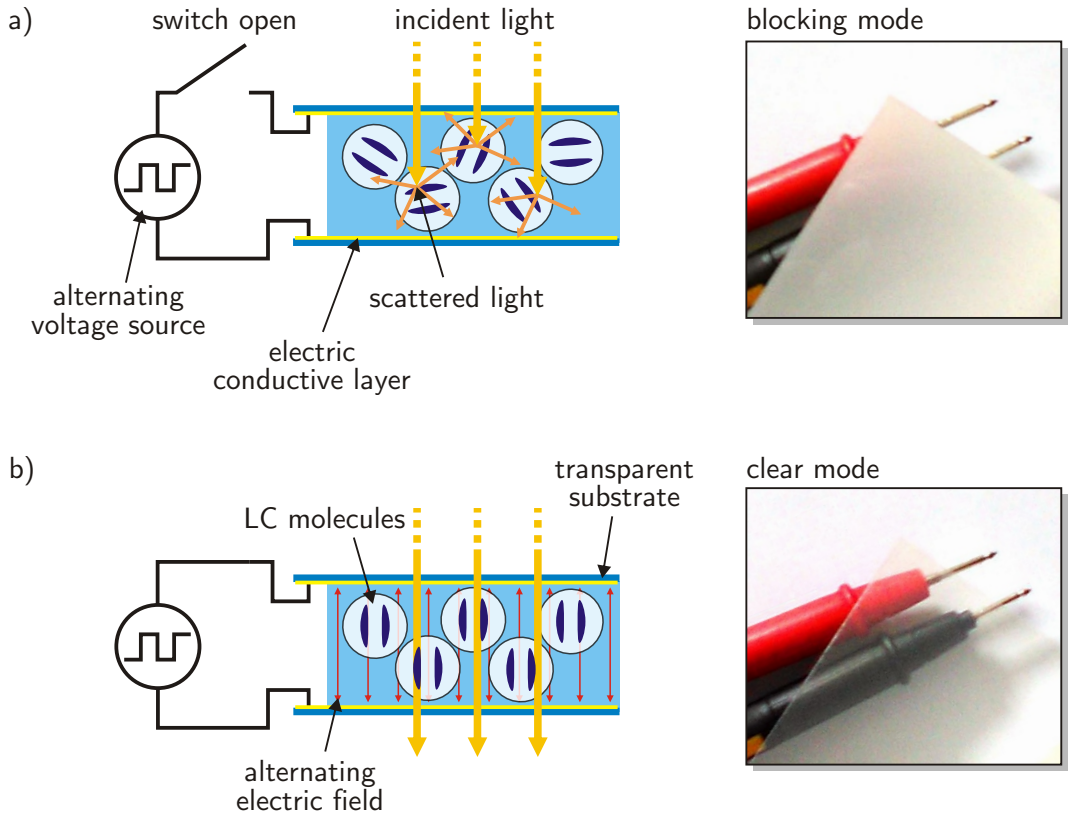

Figure 6.29: Different states of PDLC foil and the corresponding inner molecular structure: a) PDLC diffuse, LC molecules arbitrarily aligned; b) PDLC clear, all LC molecules aligned with respect to the applied electric field.

As illustrated in Fig. 6.29, the LC molecules are not aligned with each other in the blocking state and the incident light cannot pass straight through the layer. It is reflected and scattered in arbitrary directions, causing a diffuse propagation. Therefore, the effect of blocking the light is a combination of the following processes: i) diffuse transmission: the incident LOS is spread and distributed over a greater area, thereby causing a lower light intensity at the detector; ii) diffuse reflection: part of the light is scattered back and

reflected in the direction of the light source; iii) absorption: a small amount of light is also absorbed by the foil itself. In the transmission state, a voltage is applied to the LC layer. The molecules adapt their alignment to that of the electric field and do not scatter the light any more – the foil is transparent with a high transmission value. When a DC voltage is applied, the transmission ability degrades over time. To avoid this, an alternating voltage must be used [SP92].

6.3.3.2 PDLC Characterization

To measure the different transmission values, the foil is placed between a photodetector and a white phosphor LED as shown in Fig. 6.30, similar to the single LC cell. An aperture ensures that just a small, nearly parallel beam of light hits the detector without straylight. To obtain the angular characteristics, the foil is rotated from 0 to 80 degrees. Due to physical restrictions of the setup, the foil is located 9 cm in front of the photodetector, where the distance between detector and light source is 40 cm.

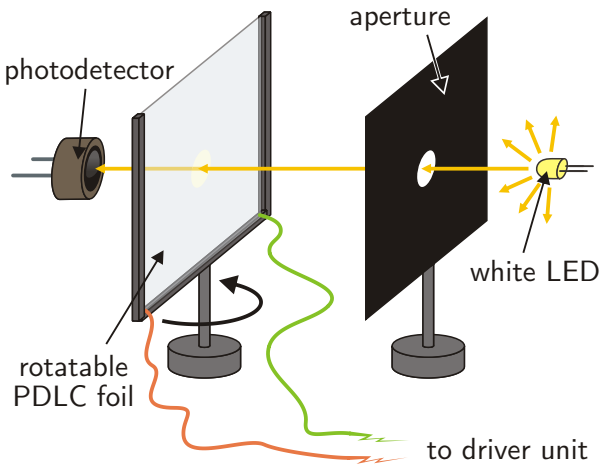

Figure 6.30: Experimental setup for PDLC foil characterization for the line-of-sight transmission with an LED light source. The foil can be rotated in the beam of light.

The foil is driven by a square wave voltage of 30 V amplitude at a frequency of 1 kHz. With these parameters, the maximum possible transmission factor w_1 through the foil is achieved. The transmission factor for the diffuse scattering state is called w_0. These two parameters were derived in additional experiments. As the distance between light source, foil and detector has a great impact on performance, the best result for w_0 can be achieved when the foil is located in the middle between the photodetector and the light source, but this is not a suitable VLC setup. Fig. 6.31 shows that the rotation of the foil has a great

impact on transmission. As incident light becomes more oblique when the foil is rotated, the transmission value is decreasing. Presumably this effect is caused by the misalignment of light and the liquid crystal molecules, which are still oriented with respect to the applied electric field. The other part of the characterization is shown in Fig. 6.32, where the spectral response of the foil is examined. As normal white phosphor-based LEDs are used for illumination systems with combined VLC, the filter should be effective throughout the complete visible-light spectrum. A PDLC foil offers a nearly-flat response with a slight dipping in the blue part of the spectrum. The ripple at the higher end of the spectrum is caused by noise originating from low light intensity in this spectral area.

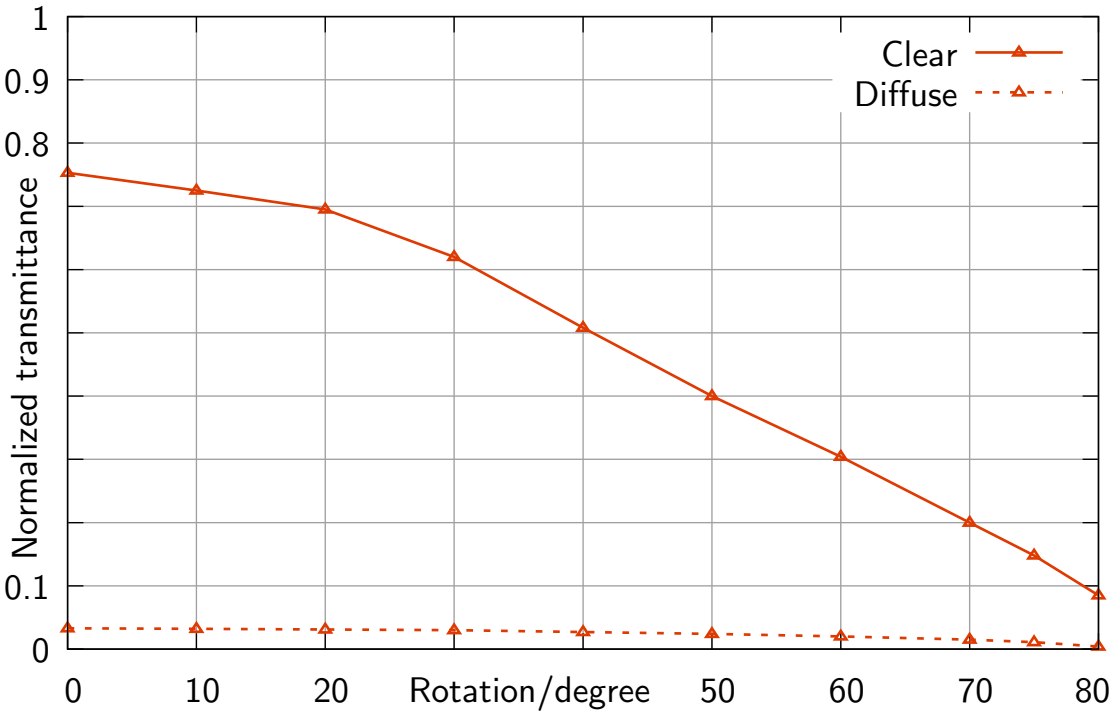

Figure 6.31: Experimentally measured PDLC transmission factors for blocking and non-blocking cases, dependent on the rotation.

6.4 Photodetectors

A silicon photodetector is a current source, which produces a photocurrent due to the inner photoelectric effect [Don00], similar to a photovoltaic cell. Here, incident photons can create an electron-hole pair, if the photon's energy is higher than the bandgap of the semiconductor materials. The photocurrent is approximately proportional to the incident

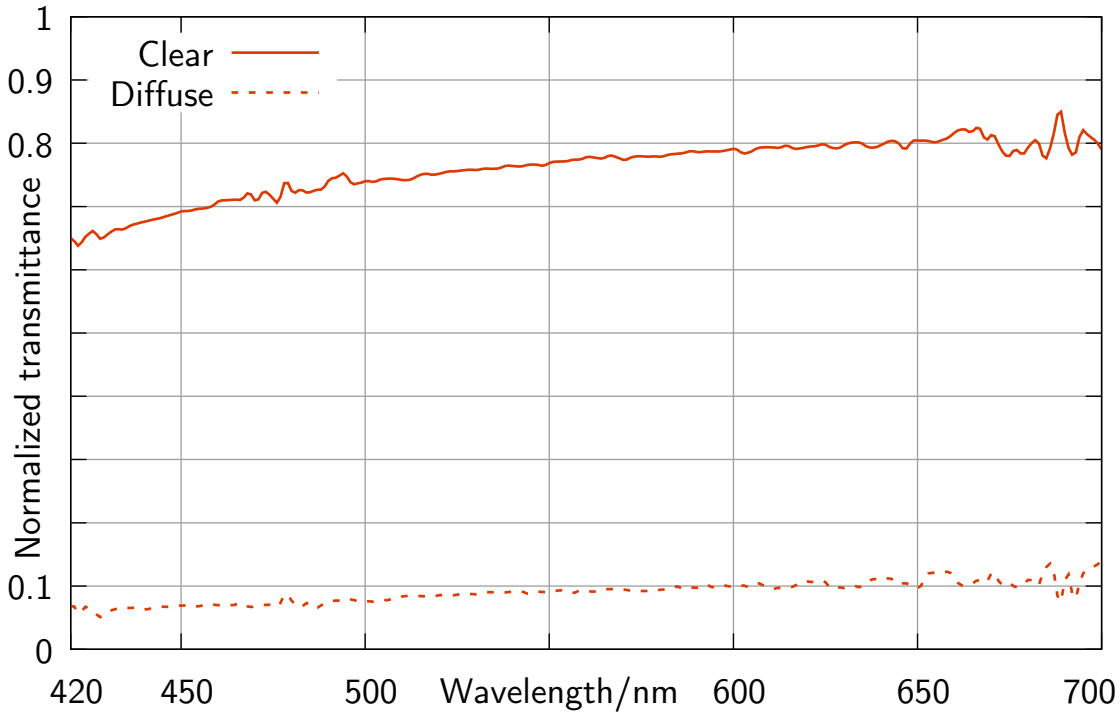

Figure 6.32: Experimentally measured PDLC transmission factors for blocking and non-blocking cases, dependent on the wavelength.

light intensity. There are some variants with a pn junction as well as others with a pin junction for faster frequency response.

6.4.1 Optical Characteristics

The FOV of a photodetector is determined by its housing and the optical concentrator (lens) – if present. There are many different types of housings, as shown in Fig. 6.33. The active area is mostly of a rectangular shape of different sizes. Silicon-based photodetectors have a spectral responsivity, which is wavelength-dependent. The highest sensitivity is in the infra-red region and decreases nearly linearly with increasing wavelength, as shown in Fig. 6.34 for an Osram SFH 206 K photodiode. For some applications, dedicated "blue-enhanced" detectors are available, which are more sensitive to light in the blue part of the spectrum than regular ones.

Incident photons cause shot noise in the electrical domain as each photon produces a

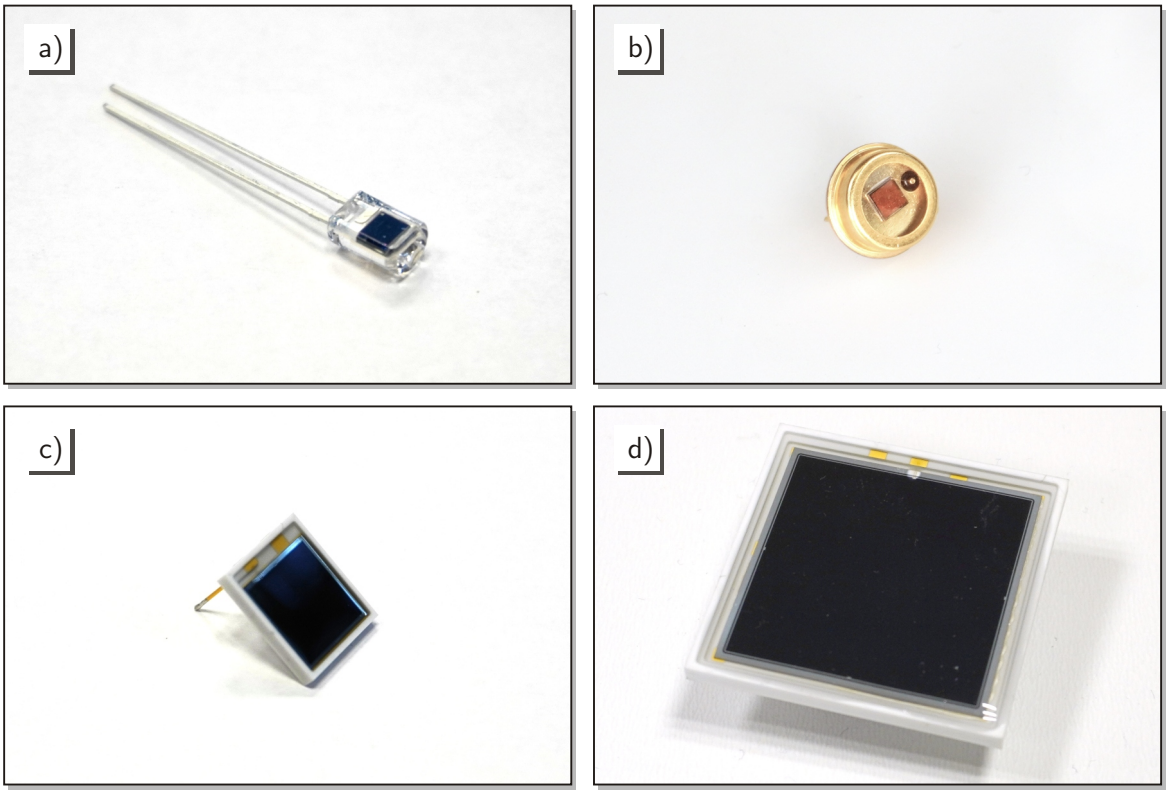

Figure 6.33: Examples of different photodiodes: a) Osram SFH 206 K silicon diode with a sensitive area of 7.02 mm^2, b) Epigap EPD-440-0-3.6 gallium phosphide diode with a sensitive area of 10.9 mm^2, c) Hamamatsu S3590 silicon PIN diode with a sensitive area of 100 mm^2, d) Hamamatsu S3584 silicon PIN diode with a sensitive area of 784 mm^2.

discrete current pulse. The variance is given by

$$\sigma^2_{\text{shot}} = 2e_0 R_{\lambda,k} P_{\text{r}} B, \tag{6.7}$$

where electron charge is represented by e_0 and the Boltzman constant by k_{B}. The electrical bandwidth is given by B. Shot noise is caused by all types of light sources, regardless of whether these are desired light sources or interferers. Thus, the noise variance increases linearly with the total optical receive power P_{r}.

6.4.2 Electrical Characteristics

Photodiodes can be used in either the photovoltaic mode or the photoconductive mode. In the photovoltaic mode, the photocurrent flows in forward direction. The photodiode

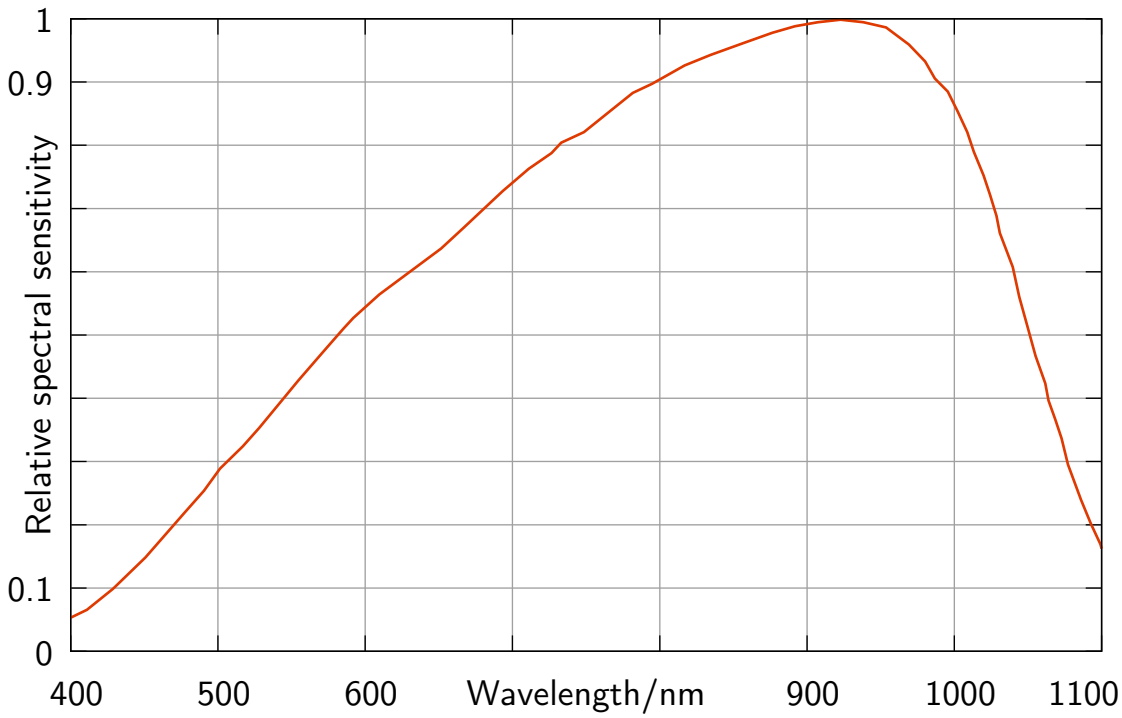

Figure 6.34: Spectral responsivity of an Osram SFH 206 K photodiode; extracted from [OSR20].

generates a positive voltage, which depends on the load. This mode is used for harvesting electrical energy with large-area photodiodes, commonly known as solar cells.

In the photoconductive mode, the photocurrent flows in the reverse direction and the frequency response is much higher than in the photovoltaic mode. This mode is used for intensity measurements, as needed for a VLC receiver. By applying a reverse bias voltage, the junction capacitance can be decreased for an even faster system response, but doing so causes a higher dark current. The small-signal behavior can be modeled by the equivalent circuit given in Fig. 6.35. For special applications, highly adapted variants of photodetectors, like the avalanche diode, are also available [Don00].

There are also some reports of using a solar-panel cell for simultaneous energy harvesting and data reception [WT+15; CM+17].

6.5 Receiver Circuits

For amplifying the usually weak photocurrent, a trans-impedance amplifier (TIA) can be used. These types of amplifiers transform current into an amplified voltages, which is

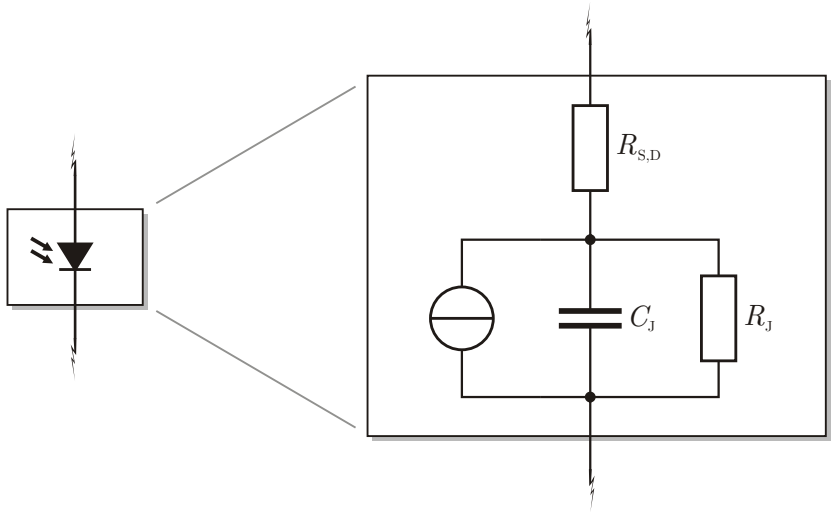

Figure 6.35: Small-signal circuit model for a photodiode, based on [Don00].

proportional to the current. A realization can be achieved by using an operational amplifier (op amp) in the configuration shown in Fig. 6.36 a) [HH89; Gra96]. The feedback resistor R_{f} defines the amplification factor and the feedback capacitance C_{f} prevents oscillation of the circuit. There are different ways of connecting the photodiode as well as different ways of biasing [Bak17]. The most simple case is a bias voltage of zero, so that the photodiode operates effectively in a short circuit as the op amp tries to keep the voltage between its input pins at zero. The cathode of the photodiode is connected to the negative input and the anode to ground as well as the positive input of the op amp. This way, a single-rail operation of the amplifier is possible as only one supply voltage is mandatory and this circuit can easily be integrated into a larger-scale circuit. To prevent further oscillation, the input levels of the op amp should be kept at a certain minimum level above ground voltage as shown in Fig. 6.36 b), and should not reach the upper rail supply voltage, too. This can be realized by pinning the positive op amp input to a lower bound voltage created by a voltage divider with $R_1 >> R_2$.

The op amp is the major noise source in a VLC receiver as it is prone to thermal noise. The variance of this noise is given by

$$\sigma^2_{\mathrm{therm}} = 4k_{\mathrm{B}}TBR_{\mathrm{f}}^{-1}, \tag{6.8}$$

where k_{B} is the Boltzman constant and T is the absolute temperature.

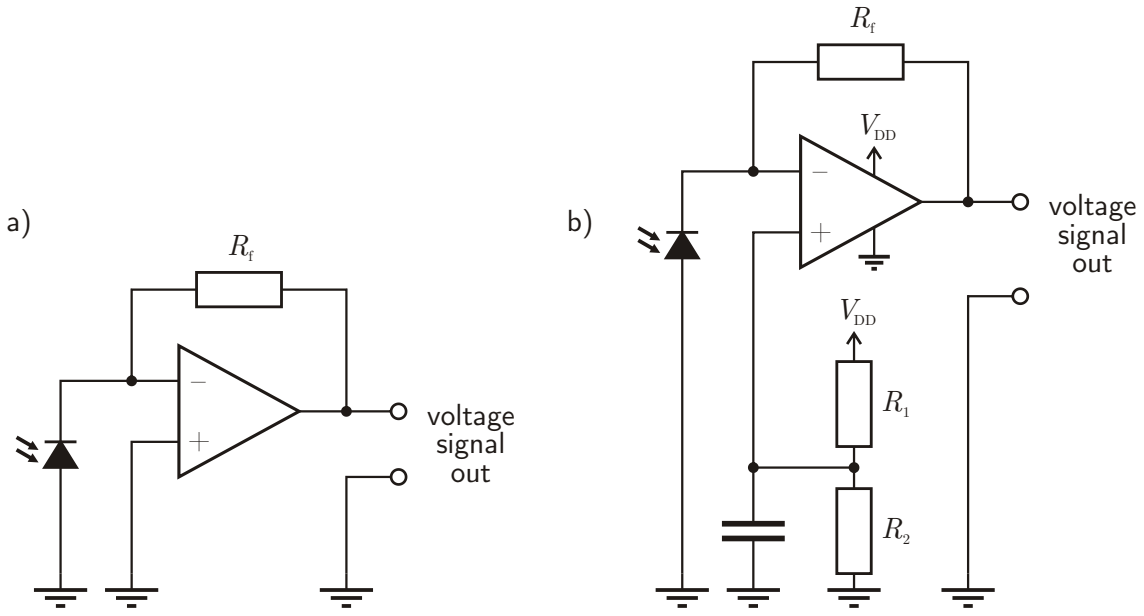

Figure 6.36: a) Basic TIA circuit; b) TIA circuit with bound for single-rail operation, based on [Cal14].

6.6 Summary

This chapter provides an overview of the hardware components of a typical VLC transmission system, starting at the transmitter side with the LED. The electrical and optical characteristics are briefly explained and different types of LEDs are presented. Afterwards, driver and modulator variants are introduced. The range of drivers includes those for simple binary signals as well as complex ones, which support nearly arbitrary signals. The most simple LED driver is a single resistor for steady-state operation. This type of driver is extended subsequently to achieve a binary modulation of the emitted light. For supporting an almost arbitrary modulation, a driver circuit based on a buck converter is proposed and tested with DMT modulated signals in a LTSpice simulation. Due to the high hardware requirements of the buck converter when used for high-speed modulation, a compromise version of the binary level modular is created that also supports multiple amplitude levels while maintaining low hardware complexity. This discrete-step amplitude modulator is then tested with PAM-4 modulated data in a physical experiment.

For the receiver side, the physical composition and properties of different LC filters are discussed and experimentally derived. Therefore, a single LC cell is experimentally characterized with respect to their spectral and angular transmittance behavior. These values are taken for the numerical simulation model of the previous chapter. Furthermore, off-the-

shelf color and monochrome LCDs, and for comparison, a PDLC foil are also evaluated in terms of transmittance, including possible aberration errors. Finally, the optical and electrical properties of photodiodes are discussed and principles of transimpedance amplifier circuits are presented.

7

Experimental Testbed

For further investigations of massive MIMO scenarios, a room-sized testbed was constructed. It is used to verify the principle of LCD-based interference suppression by delivering a proof-of-concept. The testbed consists of a fixed LED transmitter array and a mobile receiver unit equipped with the LCD filter.

7.1 Conception

The main purpose of the testbed is to generate different lighting scenarios, which can be evaluated in terms of the LCD interference mitigation principle presented in the previous chapters. It is not designed for actual data transmission, although also suitable for this purpose. A receiver equipped with a photodiode and LCD should be freely placeable in the room and should be able to initiate different measurements and LED configurations. A second application for the testbed would be to evaluate different LCD-based angle-of-arrival methods for future research, but doing so is beyond the scope of this dissertation. The requirements for these purposes are to provide

- many LED lights in order to create a massive LED array,
- control for each LED individually in terms of color and intensity,
- a flexible user interface for setting LED states,
- an interface for automatically executed measurement modes.

Based on the system draft in Fig. 4.2, a modified version is now presented in Fig. 7.1. The system provides 40 LEDs in total controlled by a Raspberry Pi computer (TX Raspi)

and a mobile LCD receiver, also Raspberry Pi-based (RX Raspi), which is able to control the LEDs with a shell interface on the TX Raspi, accessible via WiFi. The functional software diagram is sketched in Fig. 7.2. The TX Raspi serves as WiFi access point for the RX Raspi and for user access.

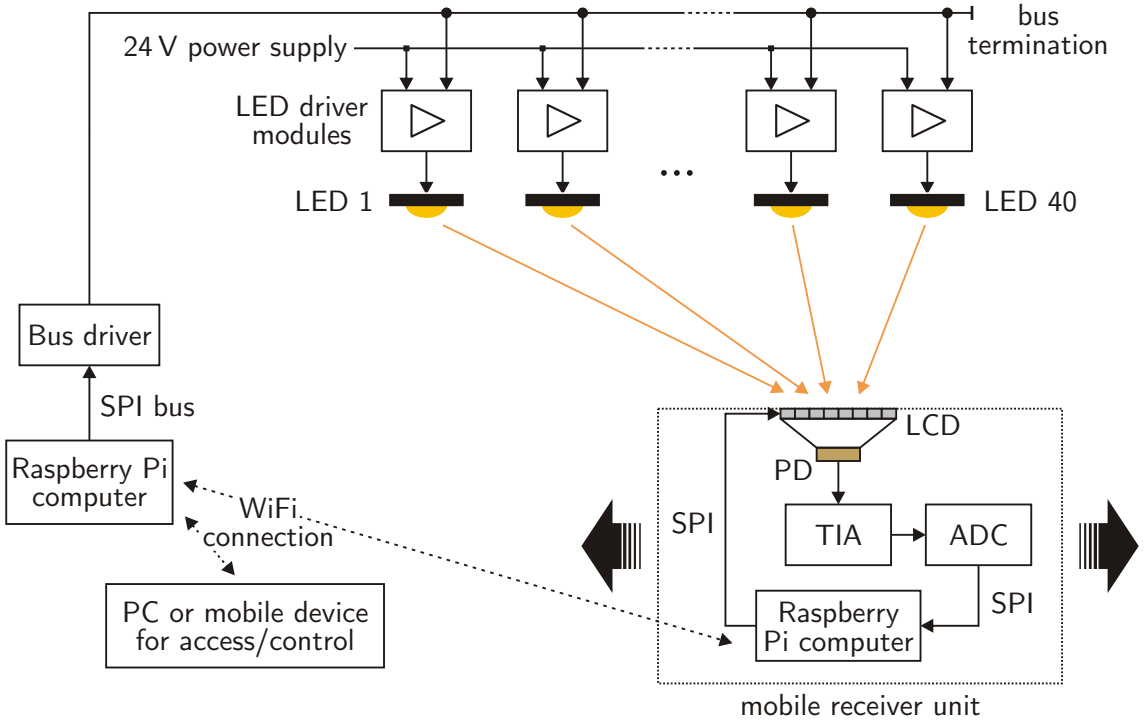

Figure 7.1: Functional block diagram of testbed hardware components.

7.2 Setting

The transmitter array is installed in a 5.86 m $\times$ 7.10 m room with a ceiling height of 3.02 m. It features an LED array of 40 LEDs, which are arranged in an interleaved 4×10 grid at the ceiling, as shown in Fig. 7.3. As the ceiling features suspended tiles, individual tiles can easily be exchanged with a transmitter module mounted on a tiled-size plate.

Alongside one room wall, the power supply is located, which has taps for every row of transmitter modules. Four modules, whose power sockets are linked together, form a row. The power supply has two parallel strings of $2 \times 6\,\mathrm{mm}^2$ cross-section, handling five rows each in order to keep the supply current at a reasonable level. The maximum power consumption is around 1 kW at a system voltage of 24 V, delivered by two switching power supplies for the two strings.

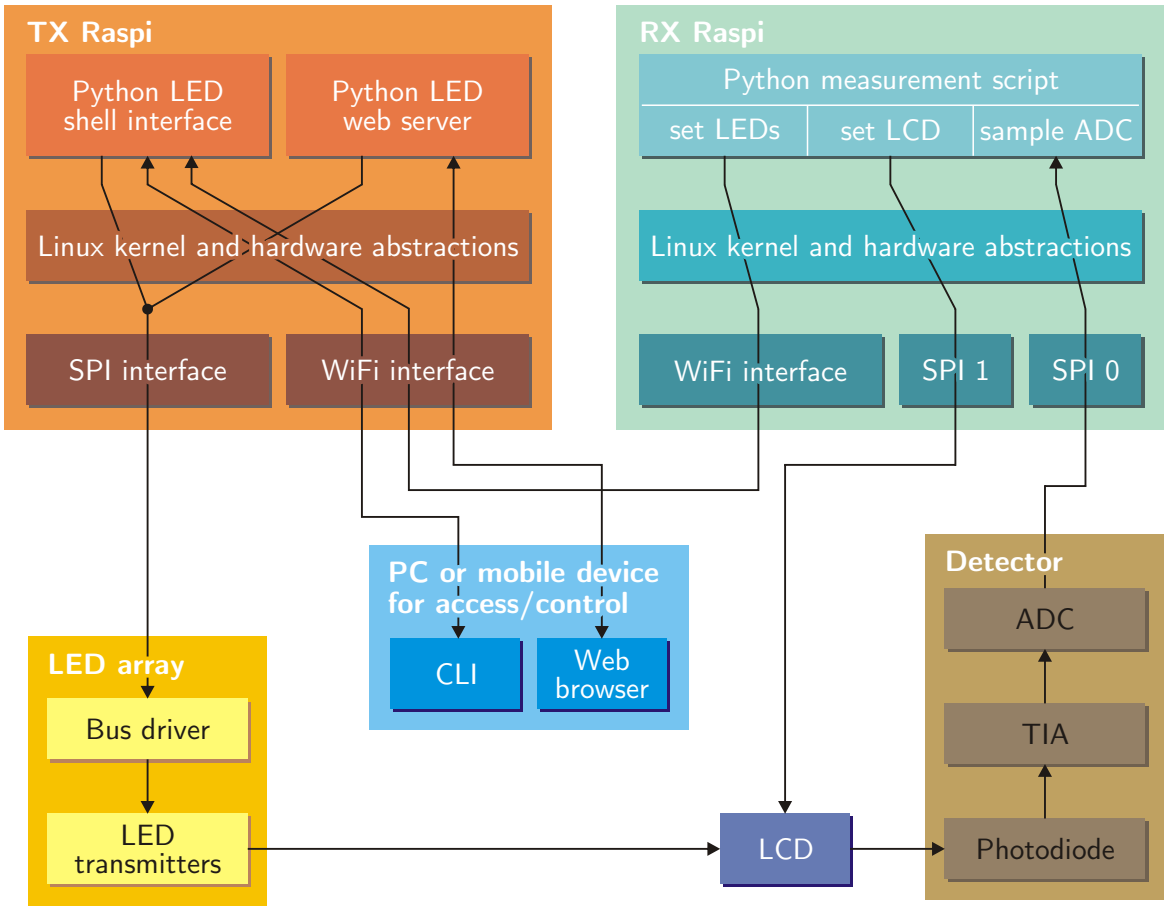

Figure 7.2: Overview of testbed software components and hardware interfaces.

All 40 modules are connected in parallel along a modified serial peripheral interface (SPI) bus, as shown in the block diagram given in Fig. 7.1. The bus is realized by regular twisted-pair ethernet cable (CAT6) and is terminated with 100 Ω at the last transmitter. In order to maintain a proper signal along the bus, repeater modules are used. A Raspberry Pi-based unit is employed for controlling the LEDs. At the receiver side, a photodetector module was built and equipped with the LCD interference suppression filter. The receiver can be placed anywhere in the room in order to conduct measurements.

7.3 Transmitter Design

7.3.1 LED Transmitter Modules

One transmitter element, as shown in Fig. 7.5, consists of a four-color LED of the type LED Engin LZC-03MA07, mounted on a heatsink (Fischer Elektronik V 7331G) with thermal

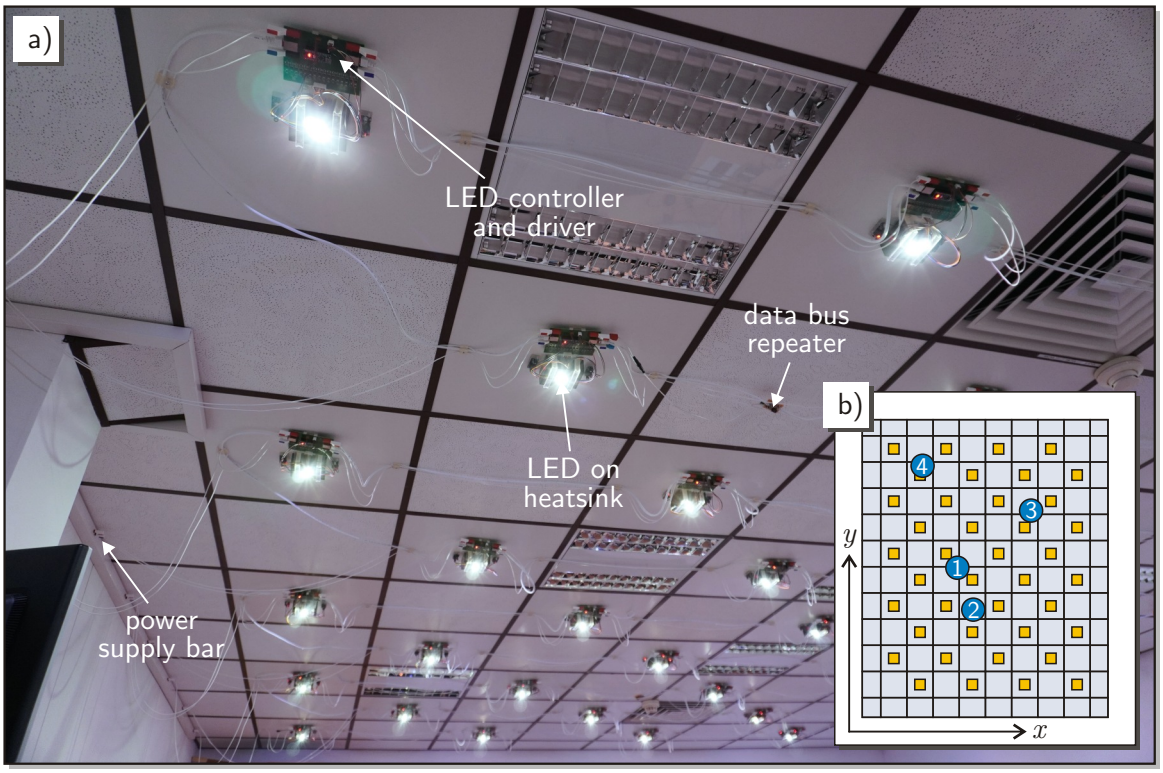

Figure 7.3: a) Photo of testbed while LEDs are switched on; b) arrangement of LEDs (yellow squares) and receiver positions 1-4 (top view), based on [KH+22].

compound glue, a custom-made printed circuit board (PCB), two LM2596 DC-DC step-down converters and an Arduino Nano, which is an ATmega328-based microcontroller board. The basic structure is given in Fig. 7.4 as a block diagram. The LED is capable of 10 W maximum electrical power per color, however, in this design only 7 W were used in order to extend lamp lifetime and to keep the current low. To limit thermal losses small, the voltages of the two DC-DC converters are set closely to the LED forward voltage. The four colors are red, green, blue and amber, with the spectral distribution shown in Fig. 7.6. The common yellow-green gap of LEDs is clearly visible. Two LED channels share a common voltage supply, as red and amber have similar forward voltages. This also applies to green and blue. The driver board employs the principle of the discrete-step amplitude driver presented in Chapter 6.2.4. It supports 16 amplitude levels per color by using four different resistors in parallel. These resistors can be switched by power MOSFETs of type FDS6670A, which are controlled by the Arduino microcontroller. The typical rise and fall time is 13 ns, while the typical switch-on delay is 11 ns. The typical switch-off delay is 40 ns [Fai03]. Regarding the LED, the manufacturer does not specify any rise or fall times in

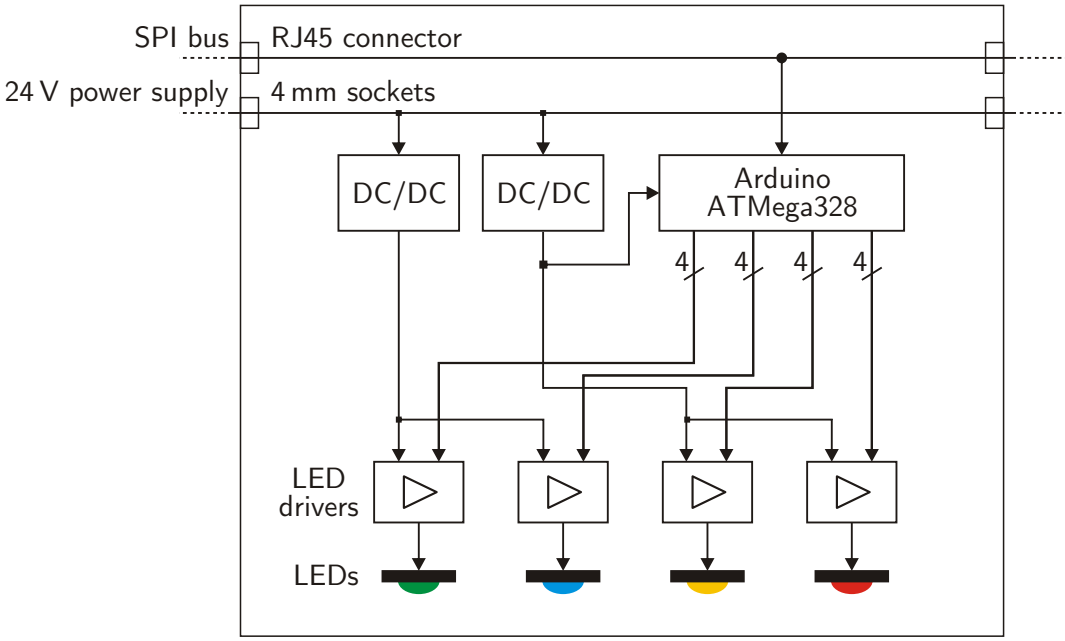

Figure 7.4: Block diagram of transmitter module.

the corresponding data sheet [LED18]. It should also be noted that the switching speed of the LED is highly dependent on the driver circuit as mentioned in Sec. 6.2.2. The full schematic of one transmitter module is given in Appendix D.4.

7.3.2 Control Unit

The control unit consists of a Raspberry Pi computer, where several Python scripts can be executed to set the state of the LEDs. Therefore, the hardware SPI interface is used to generate the bus signals. An example script is provided in Appendix D.1. A driver module, similar to the repeater modules, amplifies the signals and transmits them over the data bus. There is a Python interface, which can be accessed at command-line interface (CLI) level via a secure shell (SSH) connection over the integrated WiFi access point by the receiver module. Additionally, the web interface for setting the LEDs by e.g. laptops or smart phones is also provided by a Python script, which starts at boot time.

7.3.3 Bus Design and Control Signals

The bus connects every transmitter and the control unit in a meandering path. There are two data lanes – master out/slave in (MOSI) for uploading data to the LEDs, and master in/slave out (MISO) for receiving data from the LED modules. The latter one

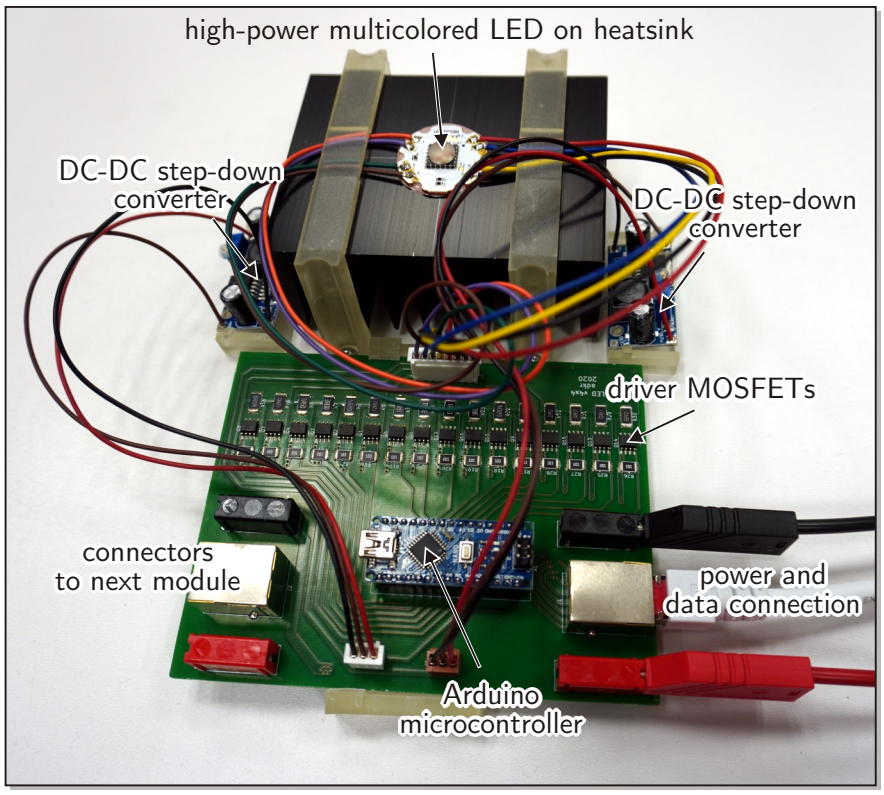

Figure 7.5: Photo of one transmitter module, based on [KH+22].

is not implemented, but can theoretically be retrofitted in software for the transmitter modules and by using a voltage level converter for the Raspberry Pi. Currently, only a one-way transmission is implemented. For addressing each individual device, the SPI bus uses commonly a so-called chip select (CS) lane. As this is not feasible with 40 transmitters, there is only one CS lane for all and the addressing of the modules is realized in software. Lastly, there is also a clock lane (serial clock, SLCK) which defines the speed of data transmission via the bus. Each Arduino microcontroller has a tap along the bus, where the data and clock lanes are connected to the SPI pins. It has also a unique ID in the range of 1 to 40 in its firmware, addressing the number of the transmitter module.

One data package consists of three bytes, where the first byte is the address byte and the following two bytes define the state of the LEDs. The address byte 0x00 is the broadcast address. Regarding the payload, the first data byte addresses the green (G) and blue (B) channel in the order 0xGB and the second data byte amber (A) and red (R) as 0xAR. Hence, each color state is defined by four bits. The Arduino collects these three bytes and checks, if the address byte is either 0x00 for broadcasting or its own ID. In this case, the payload data is written into the appropriate output registers to set the pin states. Subsequently,

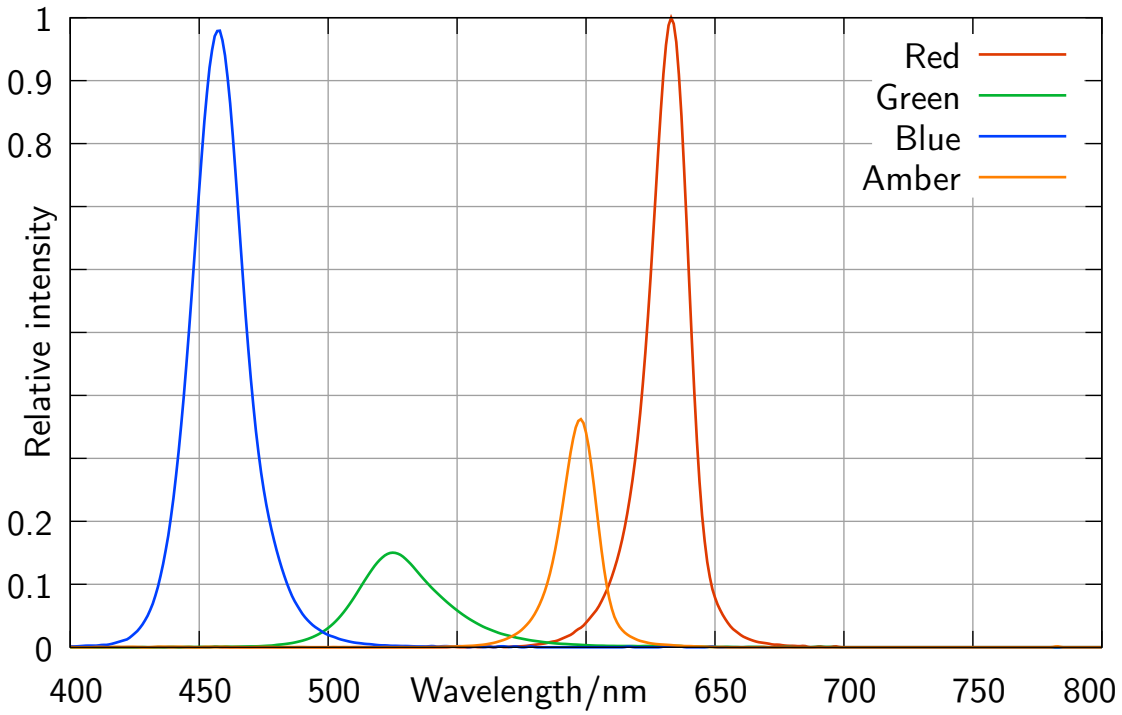

Figure 7.6: Relative spectra of testbed at full power, normalized to peak intensity of red.

the byte counter is reset. In the case of a transmission error or an incomplete transmission, the byte counter also resets after some time. The clock frequency of the Arduino is the limiting factor in terms of speed. A reliable communication is possible with a bus clock frequency of 1 MHz. The firmware source code of the Arduino is given in Appendix D.2.

7.3.4 Repeater Modules

The repeaters (Fig. 7.7) as well as the bus driver module at the Raspberry Pi are based on the 74HC245 circuit. This is an octal bus transceiver integrated circuit (IC), which operates at a logic level voltage of 5 V, but also detects 3.3 V logic levels as generated by the Raspberry Pi. All four SPI lanes (MOSI, MISO, CS and SCLK) are fed through the bus transceiver IC, and the remaining four channels are grounded. The MISO lane is not fed back to the Raspberry Pi as input. To do so, an level converter would be required as the input pins of the Raspberry Pi are not 5 V tolerant. Hence, in its current state, there is no direct feedback from the LED transmitter modules back to the Raspberry Pi. Due to the long cable lengths of the data bus, there are three repeaters distributed along the

bus, as indicated in Fig. 7.3 a). As the system voltage is 24 V, a (fused) DC-DC step-down converter is used for achieving the desired supply voltage of 5 V.

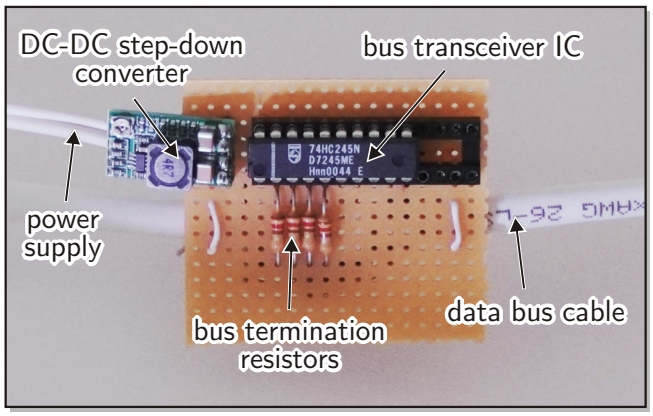

Figure 7.7: Photo of one repeater module at the ceiling.

7.4 Receiver Design

The receiver module consists of an "Osram SFH 206 K" photodiode, a modified "Waveshare 3.5inch RPI LCD (A)" LCD, as shown in Fig. 7.8, a custom-made TIA board based on a "TI OPA847" operational amplifier (op amp), a "Waveshare RB-Wav-08" analog-to-digital converter (ADC) shield and a Raspberry Pi computer. The functional arrangement is depicted in the block diagram in Fig. 7.1 as "mobile receiver unit". The photodiode is located below the LCD at the center with an adjustable distance in a custom-made light-proof housing. In Fig 7.9, the receiver module is depicted, with a close-up view of the photodiode in Fig 7.10. While the LCD is to be mounted directly on top of the Raspberry Pi PCB, the connection needs to be extended by jumper wires. The backlight is removed, so that the bare LCD is free to place over the photodiode. The Raspberry Pi can sample the TIA output via the ADC shield and can also set the LCD pixels. As described in Section 7.3.2, the control unit also serves as WiFi access point and the receiver Raspberry Pi can connect to it in order to control the LED modules at the ceiling.

7.4.1 Photodiode and TIA

The SFH 206 K photodiode is a silicon PIN diode in a clear epoxy package. It features a typical photocurrent of 80 µA and a sensitive range of 400 nm to 1100 nm with an active area of 7.02 mm^2. It is therefore quite suitable for VLC applications.

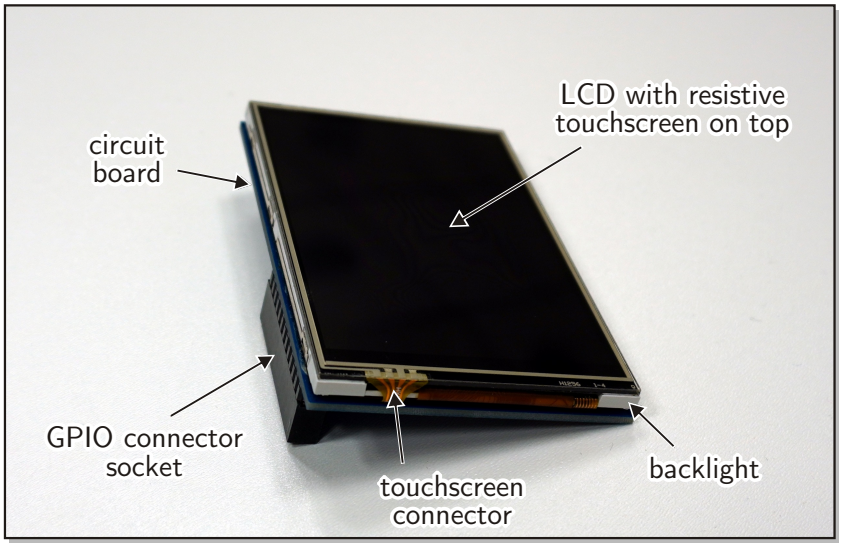

Figure 7.8: Unmodified Waveshare LCD, designed as stack-on-top shield for a Raspberry Pi computer.

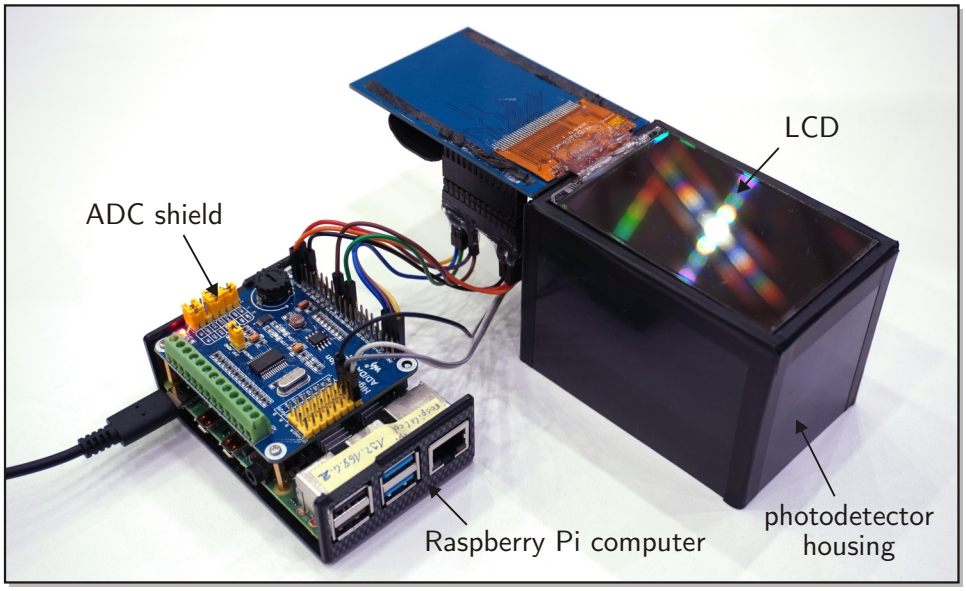

Figure 7.9: Receiver unit with one photodetector and LCD, based on [KH+22].

The requirements posed by the TIA are that it can run single-railed at 5 V and that the amplification factor is high enough to obtain a reliable reading of the output value with the ADC. A high bandwidth is not necessary in this arrangement. The schematic is given in Fig. 7.11. Experiments show that a feedback resistor of 20 MΩ was needed as the Waveshare LCD has a high attenuation on the receive intensity. An alternative would

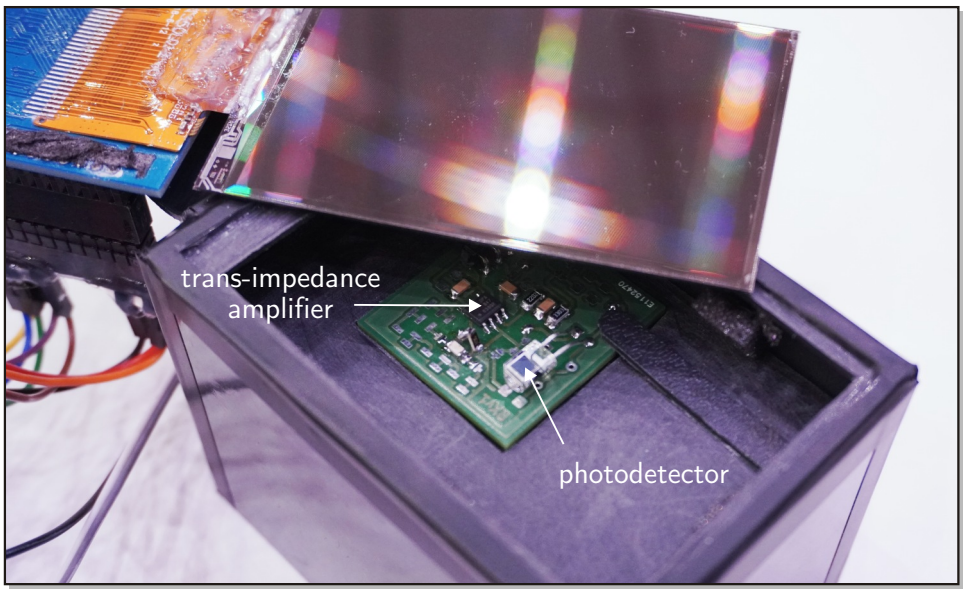

Figure 7.10: Detailed view of photodiode inside its lightproof housing, based on [KH+22].

be using an amplifier with two stages, a TIA stage followed by a voltage amplifier stage. Because of the single-rail operation, the input must not be too close to zero, e.g. when the receive intensity is too low – otherwise the op amp can oscillate. Therefore, a voltage divider is used to keep a certain minimum level.

7.4.2 LCD, ADC and Raspberry Pi Setup

The LCD as well as the ADC are shields for the Raspberry Pi, which means that they are both meant to be stacked directly on top of the general purpose input/output (GPIO) pin header of the Raspberry Pi. Both are addressed by an SPI interface of which the Raspberry Pi provides two different ones, each with multiple channels. This means that only one shield can be used at any time as they occupy the same SPI interface. To solve this problem, one device needs to be changed to the second interface. As the LCD is located at the photodiode housing, it can use the second SPI interface, and the ADC can be stacked as designed to the GPIO header using the first SPI interface. Hence, the provided display driver needs to be changed because the usage of the first SPI interface is hard-coded for the designed purpose.

The Raspberry Pi uses so-called "device-tree overlays" (.dto files) for the Linux Kernel, which activate different hardware functions of the processor and peripherals. These overlay files are compiled from an overlay source file (.dts files). For building this receiver module,

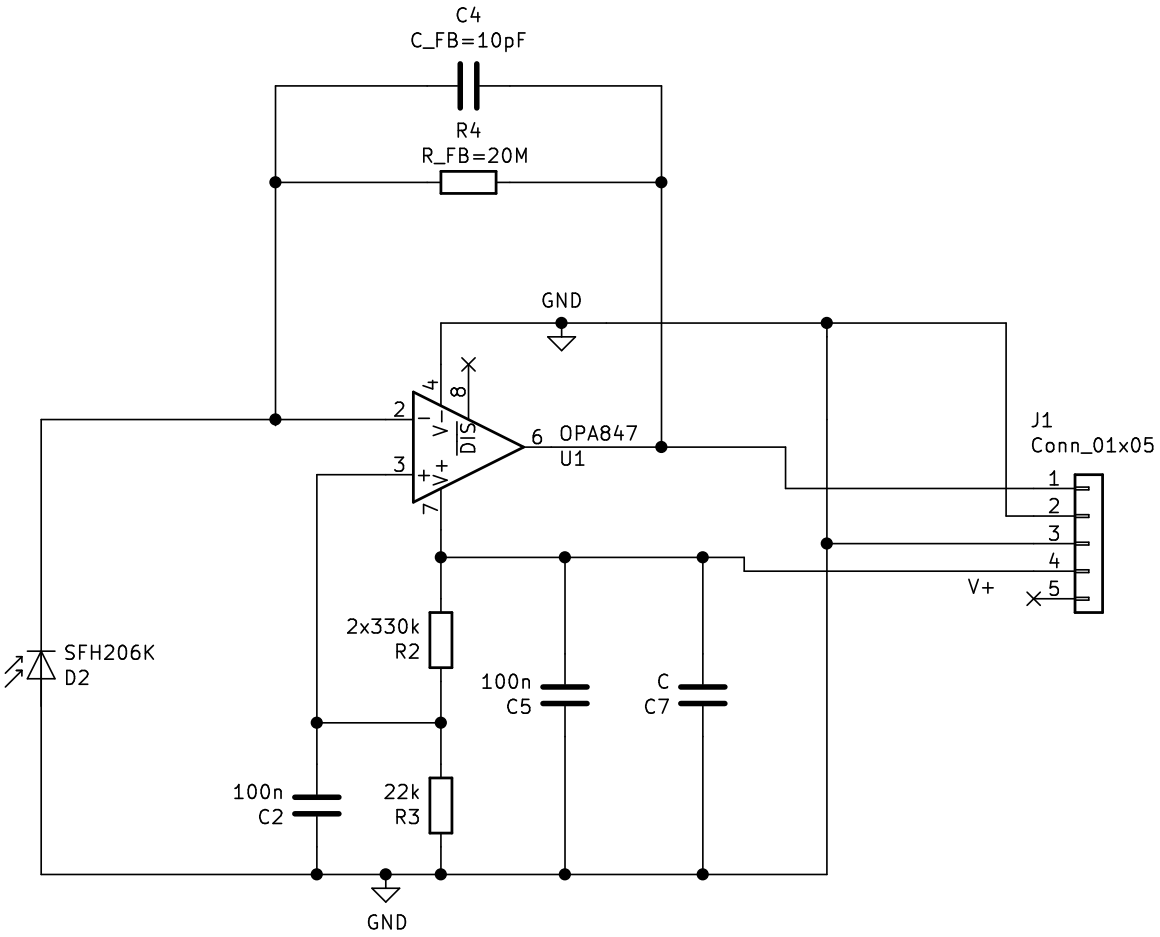

Figure 7.11: TIA schematic of the receiver circuit.

the source file "waveshare35a.dts"[1] was modified so that the display driver uses the second SPI interface of the Raspberry Pi.

7.4.3 LCD Control

The Linux Kernel provides a framebuffer device, which represents the display. This device behaves like a file in which data can be stored. By writing bytes into this framebuffer, the kernel pushes the corresponding data onto the SPI interface using the modified display driver, and the display sets the pixels accordingly. The Waveshare LCD uses a color depth of 16 bits with a color mode of RGB565. This means that five bits are used for red, six bits for green and five bits for blue, which is quite common for these types of displays as the human eye is maximum sensitive to green. Creating different pixel patterns requires a

[1] https://github.com/swkim01/waveshare-dtoverlays/blob/master/waveshare35a.dts

control software to have access to the framebuffer device. By using Python scripts, both the LCD and ADC can be used to conduct measurements with different pixel patterns. An example of the bar search algorithm presented in [HK+22] is given in Appendix D.3.

7.5 Experimental Results

The receiver was placed on a table at different positions in the room at a fixed height of 0.77 m. For the tests, a set of four positions was used, which is given in Table 7.1. At each position the intensity h_n of each transmitter LED $n \in [0, \ldots, N-1]$ was measured individually while the LCD was switched to transparent mode. By using the bar search algorithm, the specific aperture position was found for each transmitter LED which results in the measured intensity h_{bar}, n. After setting the LCD aperture to one transmitter LED, in a second step all the others transmitters were switched on without LED n, too, to measure their interference intensity h_{all}, n. All values were stored for further offline processing. Based on the initial intensities and the superposition principle, the channel matrix is generated and the LTP-SC-UPM algorithm is used to calculate the allocation of the LEDs to the different receiver positions. Then, the bar-search intensities of the assigned L LEDs for position k were taken and summed up to get the signal power while the interference intensity is calculated with the help of the corresponding h_{all}, l values:

$$\mathrm{SIR}_k = \frac{\sum_{l=0}^{L-1} h_{\mathrm{bar},l}}{\frac{1}{L}\sum_{l=0}^{L-1} h_{\mathrm{all},l}}. \tag{7.1}$$

This results in an approximate signal-to-interference ratio, which gives a comparable performance measure for each receiver position. The results in Table 7.1 show that the LTP-SC-UPM algorithm can achieve a fair SIR distribution of around 18 dB. When only positions 1 and 2 are considered, the resulting SIR values are 21.90 dB and 21.79 dB, which is approximately 3 dB more because only two instead of four receivers are present.

Table 7.1: User positions with corresponding SIR values

User Positions		**SIR**
Position 1	[2.27 m, 3.57 m, 0.77 m]	18.04 dB
Position 2	[2.65 m, 2.57 m, 0.77 m]	18.44 dB
Position 3	[4.03 m, 4.93 m, 0.77 m]	18.12 dB
Position 4	[1.44 m, 6.00 m, 0.77 m]	18.09 dB

In Fig. 7.12, the allocation of the LEDs to the positions 1-4 is shown. The positions

are processed in the order their number suggests. Here, the weakness of the LTP-SC-UPM algorithm is visible: The entries, which are handled at last, have less suitable transmitters available. This can be seen for position 3 and 4, which both gets LEDs allocated from the bottom right corner, because these are the least free ones. Nevertheless, an almost equal power distribution is achieved.

Fig 7.13 shows a validation of the superposition principle regarding the intensity measured through their LCD aperture found by the bar-search algorithm for three light sources. Here, three different light sources are taken into account. First, the bar algorithm is used when all three light sources are switched on simultaneously. After doing so, the individual intensities are measured with the bar algorithm at the same position. It can bee seen that the three individually measured ones correspond nearly to the former all-at-once run after removing the dark current of each measurement.

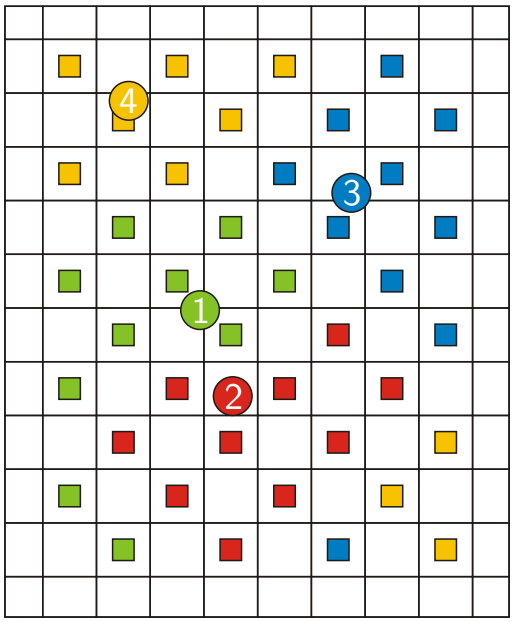

Figure 7.12: Allocation of LEDs to the receiver positions in the testbed using the LTP-SC-UPM algorithm (top view of room).

7.6 Summary

This chapter introduces the experimental massive MIMO VLC testbed, which was developed as part of this dissertation project. The main purpose of the testbed is to evaluate the effectiveness of the LCD filter and to confirm the outcome of the numerical simulation.

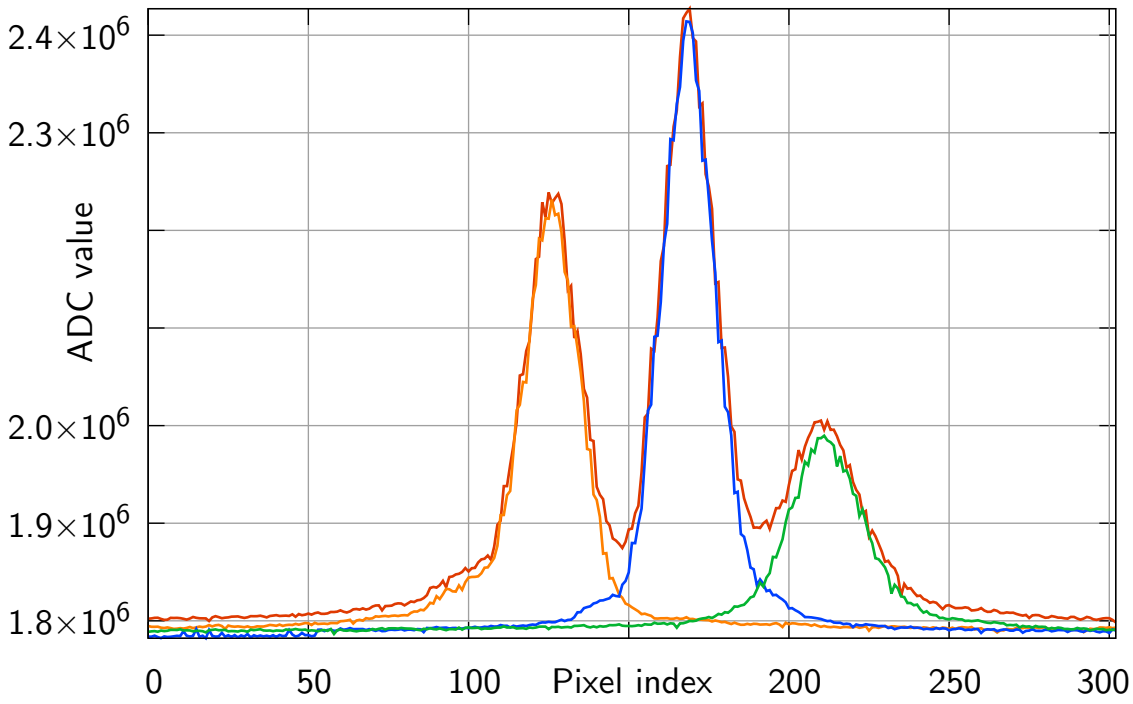

Figure 7.13: Validation of superposition principle with three neighboring LEDs: all LED are switched on simultaneously in the red curve. The other curves show the LEDs' individual intensity at the receiver.

After sketching the conception of the testbed and the overall setting, the transmitter and receiver design is presented. The transmitter array consists of forty LED modules, which can be controlled individually in terms of color and brightness. The connection to the modules is realized by using a data bus based on the SPI protocol. The LED array can be set by the control unit Raspberry Pi computer, which offers Ethernet and WiFi access for this purpose. The receiver unit uses also a Raspberry Pi computer, which connects to the control unit via WiFi. Furthermore, it controls the LCD interference suppression filter and reads out the photodetector, which is mounted below the LCD filter. During the measurement process, the receiver commands the control unit which LEDs should be switched on or off.

For testing the interference suppression principle, the complete testbed is characterized for four different receiver positions. At each position, the influence of every LED with and without LCD filter is measured and stored. Afterwards, the presented heuristic algorithm for solving the "Santa Claus" problem is applied to calculate the distribution of transmitter lights to the different receiver positions in order to maximize the resulting minimum signal-to-interference ratio.

8

Conclusion

In this dissertation, the mitigation of interference in VLC systems is investigated in theory and experiment. Different types of interference are modeled and their influence on communication aspects are discussed. The main focus is on inter-channel interference in multiuser MIMO systems. Based on this setting, several interference suppression methods are presented and evaluated. Special attention is paid to a novel LCD-based active technology, where an LCD is employed at the receiver side to block light from interfering sources while leaving the illumination characteristics of a VLC system unaltered. A dual-use system in terms of illumination and communication benefits particularly by this technology.

For the analysis of the investigated interference suppression methods, a detailed indoor channel model is derived from a communication engineering point of view. Starting from a single-user scenario, the MIMO aspect and multiuser access are integrated into the model.The proper choice of a performance metric is discussed with regard to the previously designed VLC model and the occurring interference. With respect to the constraints of a VLC system, suitable modulation formats are either adapted from the RF domain or developed solely to exploit the unique features of IM/DD systems and LED lighting specifically like multicolored emitters. The range of modulation formats dealt with includes single-carrier binary schemes as well as multicarrier ones.

Some of the modulation formats inherently suppresses inter-channel interference like spatial encoding techniques, but for other formats, a separate interference suppression is required. Therefore, different methods of doing so are presented, beginning with purely algorithmic approaches like ZF precoding. Due to their limited capabilities of removing interference physically, some measures are introduced, which are able to alter the path of light directly. In particular, the already mentioned LCD-based interference suppression

is taken and explained in detail as well as the occurring allocation problem of how to distribute the available light sources to the receivers present in the room. As a solution, the allocation problem is modeled as "Santa Claus problem" and a heuristic algorithm for solving it is suggested. Alternatively, a genetic evolutionary optimization approach is used to calculate solution candidates for the allocation. Several aspects of the LCD filter are discussed, including optical and geometrical questions regarding the performance. Next to the LCD filter, also other physical approaches are presented like passive ones, camera-based receivers or receivers with imaging optics in general. These systems suppress interference inherently under certain constraints, but lack the flexibility of the LCD filter.

In a next step, a numerical ray tracer based on the channel model is used to test the effectiveness of the proposed approaches regarding the LCD filter. The system is described in detail and how the LCD filter is implemented. Using this ray tracer, several numerical simulations are performed in order to test the performance of the LCD filter in different settings and scenarios. Starting with a single-user scenario, the complexity of the setting is increased with each scenario. In the end, a massive MIMO multicell scenario is under test. The simulations show that the LCD filter can increase the system performance compared to a reference setup. The references and settings are taken from original scenarios in the literature.

Regarding actual hardware, all necessary components of a VLC systems are presented, starting with LEDs and the appropriate drivers. For the different types of drivers, suitable modulation formats of the previously presented ones are suggested, and some of them are also experimentally verified. As main component in terms of interference suppression, the LCD technology and the working principle are explained and several types of LCDs are experimentally characterized. The derived models are used in the numerical ray tracer. Also, typical photodetectors and their receiver circuits are presented.

Finally, a VLC testbed is constructed in order to verify the outcome of the simulations in actual measurements. The testbed and its components are chosen in relation to the previously presented components and modulation techniques. For the testbed, a VLC receiver is constructed which features the novel LCD filter. By using the heuristic algorithm for solving the Santa Claus problem, allocation sets were calculated and a proof of concept regarding the ability of reducing the interference is given.

The presented experiments and results show that the proposed LCD filter in combination with the introduced optimization strategies is able to suppress interference occurring in massive MIMO VLC systems in a flexible way that conventional methods cannot achieve. Instead of lowering the interferers' power, their influence is reduced directly at the receiver

by using the LCD filter. Especially dual-use systems providing simultaneous illumination in indoor scenarios next to communication services benefit from this kind of interference mitigation.

The LCD itself enables this kind of interference suppression, but it is also the main limitation factor in this system. Even in the transparent state, the path loss is relatively high compared to other optical filters. By choosing high-contrast black-and-white display types instead of color LCDs, better light transmission can be achieved while maintaining good blocking ability. Due to the slow refresh rates of LCDs compared to typical data rates in optical systems, the configuration of the LCD filters consumes a lot of time of possible transmission time. This is especially important when using optimizing strategies that rely on updating the pixel pattern at each step, such as the pixel-wise genetic evolutionary optimization. Furthermore, the presented approaches require knowledge about the position of the transmitters and receivers or at least about the incident angles, so that the angle-of-arrival estimation takes significant time, too. Because this is a problem on its own, the relevant positions were assumed to be known in this dissertation. Consequently, one design goal of optimizing the LCD filter should be a fast adaption to the scenario, because with moving receivers, the optimization process has to be repeated for each position change. Here, implementing larger aperture sizes that are more tolerant of position changes could ease the situation, but at the cost of reduced interference suppression. Overall, the promising outcomes regarding the effectiveness motivate further research to explore more and faster optimization strategies and application fields.

For future research, the LCD interference suppression could be optimized by applying a non-binary allocation of light sources to available receivers similar as it is done in ZF precoding. LCDs have the ability to generate also gray scales, which might be useful for doing that. Support for dynamic scenarios with moving receivers should also be a focus when evaluating new optimization strategies. Additionally, color LCDs could be used and combined with color shift keying modulation. Here, a joint interference suppression and color space decoding might be possible.

Regarding the testbed, more than one receiver could be built to perform online processing of the measurements compared to the presented offline processing. Together with a faster channel estimation algorithm than the used bar search algorithm for finding of the incident angles and positions of the light sources, more accurate results could be achieved. By including many receiver positions, the position-dependent impact can be reduced. For doing so, suitable methods from the RF domain might be identified and adapted.

A

Notation

Acronyms

A	amber
AC	alternating current
ACO-OFDM	asymmetrically clipped optical OFDM
ADC	analog-to-digital converter
AMI	alternate mark inversion
ASK	amplitude-shift keying
AWGN	additive white Gaussian noise
B	blue
BER	bit error rate
bps	bits per second
CAP	carrierless amplitude phase
CAT6	category 6 cable
CCM	continuous current mode
CDMA	code-division multiple access
CLI	command-line interface
CMOS	complementary metal-oxide semiconductor
COB	chip-on-board
COG	chip-on-glass
CRI	color rendering index
CS	chip select

CSK	color-shift keying
DAC	digital-to-analog converter
DC	direct current
DEMOD	demodulator
DMT	discrete-multitone transmission
FEC	forward error correction
FOV	field-of-view
fps	frames per second
G	green
GaN	Gallium nitride
GPIO	general purpose input/output
HD-FEC	hard-decision forward error correction
IC	integrated circuit
ID	identification
IFFT	inverse fast Fourier transform
IM/DD	intensity-modulated/direct-detection
ISI	intersymbol interference
LC	liquid crystal
LCD	liquid crystal display
LED	light-emitting diode
LOS	line of sight
LPT	longest-processing time
Mbps	megabits per second
MIMO	multiple-input multiple-output
MISO	master in/slave out
MOD	modulator
MOSI	master out/slave in
MU-MIMO	multiuser multiple-input multiple-output
OCDMA	optical code-division multiple access
OFDM	orthogonal frequency-division multiplexing
OOK	on-off keying
OWC	optical wireless communication
PAM	pulse amplitude modulation
PCB	printed circuit board
PDLC	polymer-dispersed liquid crystal

PWM	pulse-width modulation
QAM	quadrature amplitude modulation
R	red
Raspi	Raspberry Pi
RF	radio frequency
RX	receiver
RZ	return-to-zero
SC-UPM	Santa Claus problem on unrelated parallel machines
SIC	successive interference cancellation
SINR	signal-to-interference-plus-noise ratio
SIR	signal-to-interference ratio
SISO	single-input single-output
SLCK	serial clock
SMOD	spatial modulation
SMUX	spatial multiplexing
SNR	signal-to-noise ratio
SPI	serial peripheral interface
TDMA	time-division multiple access
TIA	trans-impedance amplifier
TX	transmitter
VLC	visible light communication
VPPM	variable pulse position modulation
WiFi	wireless fidelity
ZF	zero-forcing
ZF-DPC	zero-forcing "dirty paper coding"

Mathematical Notation

x	scalar variable
$\boldsymbol{x}$	vector variable
$\mathbf{X}$	matrix variable
$\mathrm{x}(\cdot)$	function with argument $\cdot$
x	constant
$\hat{\cdot}$	estimate or received value

$(\cdot)^*$	complex conjugate
$(\cdot)^{\mathsf{T}}$	transposed matrix and transposed vector
$(\cdot)^{\mathsf{H}}$	conjugate transposed matrix
$\|\cdot\|_{\mathsf{F}}$	Frobenius norm of a matrix
$\odot$	Hadamard multiplication (element-wise multiplication)
$*$	convolution operation
$\mathrm{E}(\cdot)$	expected value
$\mathrm{erfc}(\cdot)$	complementary error function
$\mathrm{d_H}(\cdot,\cdot)$	Hamming distance

B

LPT-SC-UPM Allocation Algorithm

The LPT-SC-UPM presented in [KH+22] delivers an heuristic solution for the "Santa Claus problem on unrelated parallel machines" with special focus on user fairness. It should be noted that it can be implemented in a more efficient way at the expense of clarity and intuitiveness. The complexity can be reduced to $\mathcal{O}\left(KN\log(N)\right)$ then.

The notation is as follows: the function zeros($\cdot$) creates a vector or matrix consisting of zeros with the given dimensions in the argument, $\mathbf{H}[k][n]$ addresses the element in the k-th row and n-th column in $\mathbf{H}$ – the same applies to $\mathbf{G}[k][n]$ and equally to $\mathbf{H}_{\mathrm{opt}}$ and $\mathbf{H}_{\mathrm{tmp}}$. The function sum($\cdot$) returns the sum of all elements of the given vector or matrix, while argmin($\cdot$) delivers the index of the smallest element of the given vector and argmax($\cdot$) the index of the maximum element. The i-th element at index i of a vector $\boldsymbol{x}$ is referred as $\boldsymbol{x}[i]$.

Algorithm 1 LPT-SC-UPM allocation algorithm

Require: $\mathbf{H}_0$ ▷ Channel Matrix
Require: N ▷ Number of Transmitters
Require: K ▷ Number of Receivers
Ensure: $N \geq K$

$led\_taken \leftarrow$ zeros(N)
$\mathbf{G} \leftarrow$ zeros$(K \times N)$
$\mathbf{H}_{\text{tmp}} \leftarrow \mathbf{H}_0$
$\boldsymbol{prio} \leftarrow$ zeros(K)

Step 1: Prioritization of receivers with zero-gain paths
$k \leftarrow 0$
for $k < K$ **do**
    $n \leftarrow 0$
    for $n < N$ **do**
        if $\mathbf{H}_0[k][n]$ is 0 **then**
            $\boldsymbol{prio}[k]$ += 1
        end if
        n += 1
    end for
    k += 1
end for

Step 2: Allocation of light sources to receivers
while sum$(\boldsymbol{led_taken}) < N$ **do**
    $\mathbf{H}_{\text{opt}} \leftarrow \mathbf{H}_0 \circ \mathbf{G}$
    $\boldsymbol{sumsignal} \leftarrow$ zeros(K)
    $k \leftarrow 0$
    for $k < K$ **do**
        $n \leftarrow 0$
        for $n < N$ **do**
            $\boldsymbol{sumsignal}[k]$ += $\mathbf{H}_{\text{opt}}[k][n]$
            n += 1
        end for
        k += 1
    end for
    $det\_min \leftarrow$ argmin$(\boldsymbol{sumsignal})$
    if sum$(\boldsymbol{prio}) > 0$ **then**
        $det\_min \leftarrow$ argmax$(\boldsymbol{prio})$
        $prio\_select \leftarrow 1$

```
    else
        det_min ← argmin(sumsignal)
        prio_select ← 0
    end if
    led_max = argmax(H_tmp[det_min][0], ...
                     ..., H_tmp[det_min][N − 1])
    if led_taken[led_max] is 0 then
        led_taken[led_max] ← 1
        G[det_min][led_max] ← 1
        if prio_select is 1 then
            prio[det_min] −= 1
        end if
    end if
    H_tmp[det_min][led_max] ← −1
end while
return G
```

C

LC Cell Color Transmittance Characteristics

In addition to the presented transmittance values in Sec. 6.3.2.1, Fig. C.1 shows the values for colored light as well as for white light generated by a phosphorus LED (Osram LED Engin LZC-03MD07).

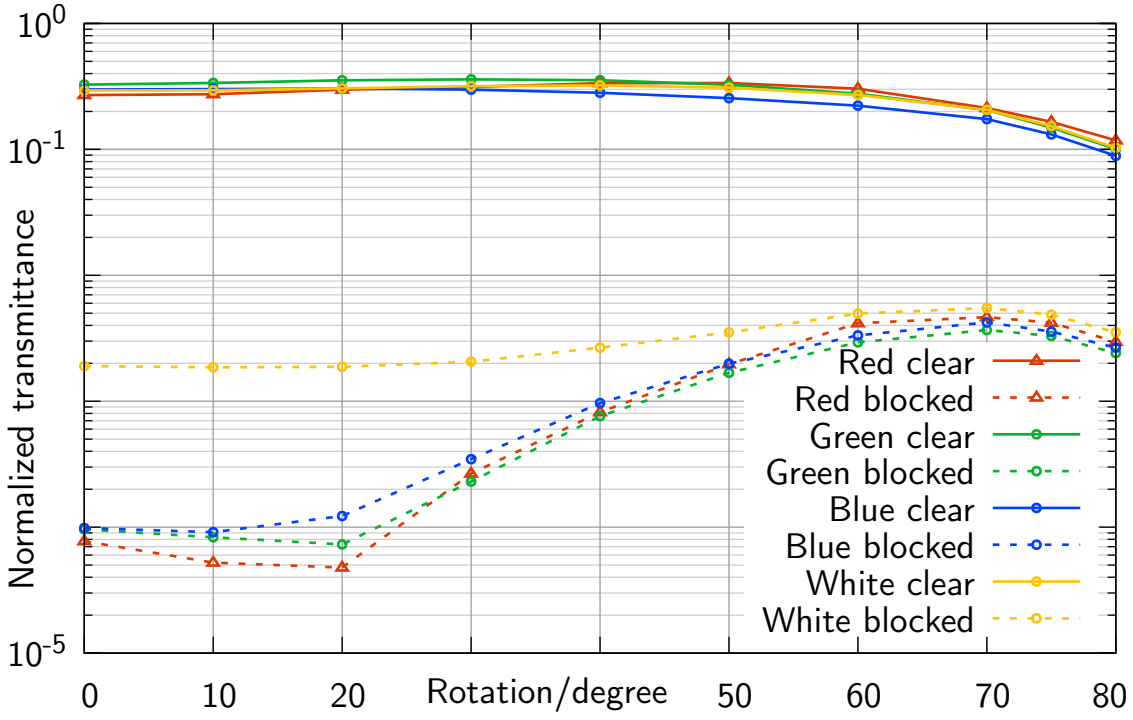

Figure C.1: Angular-dependent transmission factor of single LC cell.

D

VLC Testbed

Here the schematics and source codes for the VLC testbed components are given. The Python script is designed to run on a Raspberry Pi Computer with Debian/Raspian Linux and Python 3.

D.1 Python Transmitter Example

```
#!/usr/bin/env python3
import numpy as np
import spidev
import time
import sys

# LED dimensions
LEDx = 4
LEDy = 10
LEDarray = np.zeros((LEDx,LEDy), np.uint16) # Color scheme GGBBAARR

# Transform color values to bus format and send them
def color_transmit(addr=0x00, r_col=0x0,g_col=0x0,b_col=0x0,a_col=0
    x0):
     global spi
     if not isinstance(r_col, int) and len(r_col) == 4: # check if
         colors are combined
          color = r_col
          r_col=int(color[0])
          g_col=int(color[1])
```

```
19          b_col=int(color[2])
20          a_col=int(color[3])
21      payload = [addr, int((g_col<<4)+b_col), int((a_col<<4)+r_col)]
            # [address, databyte1, databyte2]
22      spi.xfer(payload)

24  # Process command-line arguments
25  if len(sys.argv) > 1:
26      led_id = int(sys.argv[1])
27      if led_id < 0 or led_id > LEDx*LEDy: # check if ID is valid
28          print("Invalid LED ID.")
29      else:
30          spi = spidev.SpiDev() # open SPI interface
31          spi.open(0, 0)
32          spi.max_speed_hz = 100000

34          # Default color values (0xF = on, 0x0 = off)
35          r = 0x0
36          g = 0x0
37          b = 0x0
38          a = 0x0

40          if len(sys.argv) > 2: # check color argument
41              color = int(sys.argv[2], base=16)
42              r = (color&0xF000)>>12
43              g = (color&0xF00)>>8
44              b = (color&0xF0)>>4
45              a = (color&0xF)

47          color_transmit(led_id,r,g,b,a)
48          spi.close()
49  else:
50      print("Commandline: setLED.py led_id color_rgba")
51      print("Example: ./setLED.py 13 1A1A")
52      print("For broadcasting, set led_id = 0")
```

D.2 Arduino Transmitter Firmware

```
1   #include <SPI.h>

3   #define ADDRESS 0x01    // ID of transmitter module
```

```
4  #define STANDBY 10
5
6  //#define DEBUG
7  //#define UPLOAD_SPI
8
9  void setup() {
10 #if defined(DEBUG)
11    Serial.begin (9600);   // debugging
12 #endif
13   DDRD = 0xFF; //PORTD as output
14   PORTD = 0x00;
15
16   DDRB = 0x03;
17   PORTB = 0x00;
18
19   DDRC = 0x3F;
20   PORTC = 0x00;
21
22 #if defined(UPLOAD_SPI)
23   pinMode(MISO,OUTPUT); //MISO enabled
24 #else
25   pinMode(MISO,INPUT); //MISO disabled
26 #endif
27
28   SPCR |= _BV(SPE); // Enable SPI in slave mode
29   SPI.attachInterrupt();
30
31 }
32 static volatile unsigned char i = 3;
33 static volatile unsigned char rx[] = {0x00, 0x00, 0x00};
34 static volatile unsigned char resync_counter = 0;
35
36 void loop() {
37   if (resync_counter > STANDBY) {
38     i = 3;  //reset byte counter
39   }
40   for (unsigned int k = 0; k < 6400; k += 1) {
41     for (unsigned int l = 0; l < 100; l += 1) {
42       asm volatile ("nop");
43     }
44   }
45   resync_counter += 1;
```

```
46 }
47
48 ISR (SPI_STC_vect) {
49   resync_counter = 0;
50   if (i) {
51     i--;
52     rx[i] = SPDR;
53
54 #if defined(UPLOAD_SPI)
55     SPDR = 0x42; //here upload data
56 #endif
57 #if defined(DEBUG)
58     Serial.print("i = ");
59     Serial.print(i);
60     Serial.print(", SPDR = ");
61     Serial.println(SPDR);
62 #endif
63   }
64   if (!i) {
65 #if defined(DEBUG)
66     Serial.print("rx[0] = ");
67     Serial.println(rx[0]);
68     Serial.print("rx[1] = ");
69     Serial.println(rx[1]);
70     Serial.print("rx[2] = ");
71     Serial.println(rx[2]);
72 #endif
73     if ((rx[2] == ADDRESS) || (rx[2] == 0x00)) {
74       PORTD = rx[1];
75       PORTC = rx[0]&0x3F;
76       PORTB = rx[0]>>6;
77 #if defined(DEBUG)
78       Serial.println("OK");
79 #endif
80     }
81     i = 3;
82   }
83 }
```

D.3 LCD and ADC Example with Bar Search

```
#!/usr/bin/env python3
import time
import numpy as np
from subprocess import Popen, PIPE
import ADS1256
import RPi.GPIO as GPIO

led_id = 5 # LED to find

# LCD dimensions
xsize = 480
ysize = 320
delaytime = 0.2 # seconds to wait for LCD to set
adc_repeat = 10 # averaging value for ADC measurements
barwidth = 17 # bar width in pixels
##########################################################

# RGB565 array for LCD values
framebuffer = np.zeros((xsize, ysize),np.uint16)

color = 0xFFFF # LCD bar color
led_color = 0xFFFF # LED ligt color

# open ADC device
ADC = ADS1256.ADS1256()
ADC.ADS1256_init()

def run_ssh_cmd(cmd): # SSH connection to LED control TX Raspi
    host = 'LEDraspi'
    cmds = ['ssh', '-t', host, cmd]
    return Popen(cmds, stdout=PIPE, stderr=PIPE, stdin=PIPE).stdout
        .read()

def get_ADC(): # read out and average photodiode ADC value
    global ADC, adc_repeat
    adc = 0
    for r in range(adc_repeat):
        adc += ADC.ADS1256_GetChannalValue(0)
    return int(adc/adc_repeat)

# clear all LEDs
print('Measure Dark Current...')
```

```
42 ssh_results = run_ssh_cmd('/home/pi/LEDControl/setLED.py 0 0x0000')
43 if ssh_results:
44     print(ssh_results)
45 time.sleep(delaytime)

47 # set LCD black
48 framebuffer = np.zeros((xsize, ysize),np.uint16)
49 framebuffer.transpose().tofile('/dev/fb1')
50 time.sleep(delaytime) # wait for LCD

52 adc_darkcurrent = get_ADC()

54 # set single LED
55 run_ssh_cmd('/home/pi/LEDControl/setLED.py '+str(led_id) + ' ' +
       hex(led_color))
56 time.sleep(delaytime)

58 print('Running Bar algorithm for searching LED '+str(led_id))

60 #num_steps = xsize+ysize - 2*barwidth
61 #last_step = 0

63 # vector for storing ADC values
64 results_x = np.zeros(xsize-barwidth,np.uint)
65 results_y = np.zeros(ysize-barwidth,np.uint)

67 # run bar search
68 for x in range(0,xsize-barwidth):
69     framebuffer = np.zeros((xsize, ysize),np.uint16)
70     for bar in range(0,barwidth):
71         for y in range(ysize):
72             framebuffer[x+bar][y] = color
73     framebuffer.transpose().tofile('/dev/fb1')
74     time.sleep(delaytime)
75     results_x[x] = get_ADC()

77 for y in range(0,ysize-barwidth):
78     framebuffer = np.zeros((xsize, ysize),np.uint16)
79     for bar in range(0,barwidth):
80         for x in range(xsize):
81             framebuffer[x][y+bar] = color
82     framebuffer.transpose().tofile('/dev/fb1')
```

```
83      time.sleep(delaytime)
84      results_y[y] = get_ADC()
85
86  # find maximum ADC values
87  xmax = np.argmax(results_x)
88  ymax = np.argmax(results_y)
89  print('Max-Coordinates LED '+str(led_id)+':',xmax,ymax)
90
91  # set box at found position on LCD
92  framebuffer = np.zeros((xsize, ysize),np.uint16)
93  for x in range(barwidth):
94      for y in range(barwidth):
95          framebuffer[xmax+x][ymax+y] = color
96  framebuffer.transpose().tofile('/dev/fb1')
97  time.sleep(delaytime)
98
99  # measure single LED
100 adc_single_led_lcdmax = get_ADC()
101
102 # measure all LEDs
103 run_ssh_cmd('/home/pi/LEDControl/setLED.py 0 ' + hex(led_color))
104 time.sleep(delaytime)
105 adc_all_leds_lcdmax = get_ADC()
106
107 # clear all LEDs
108 run_ssh_cmd('/home/pi/LEDControl/setLED.py 0 0x0000')
109 time.sleep(delaytime)
110
111 # clear LCD
112 framebuffer = np.zeros((xsize, ysize),np.uint16)
113 framebuffer.transpose().tofile('/dev/fb1')
114
115 print("adc_darkcurrent =",adc_darkcurrent)
116 print("adc_single_led_lcdmax =",adc_single_led_lcdmax)
117 print("adc_all_leds_lcdmax =",adc_all_leds_lcdmax)
118
119 # calculate SIR
120 SIR = (adc_single_led_lcdmax-adc_darkcurrent)/(adc_all_leds_lcdmax-
        adc_single_led_lcdmax-adc_darkcurrent)
121 print ("SIR =",SIR)
```

D.4 Transmitter Schematic

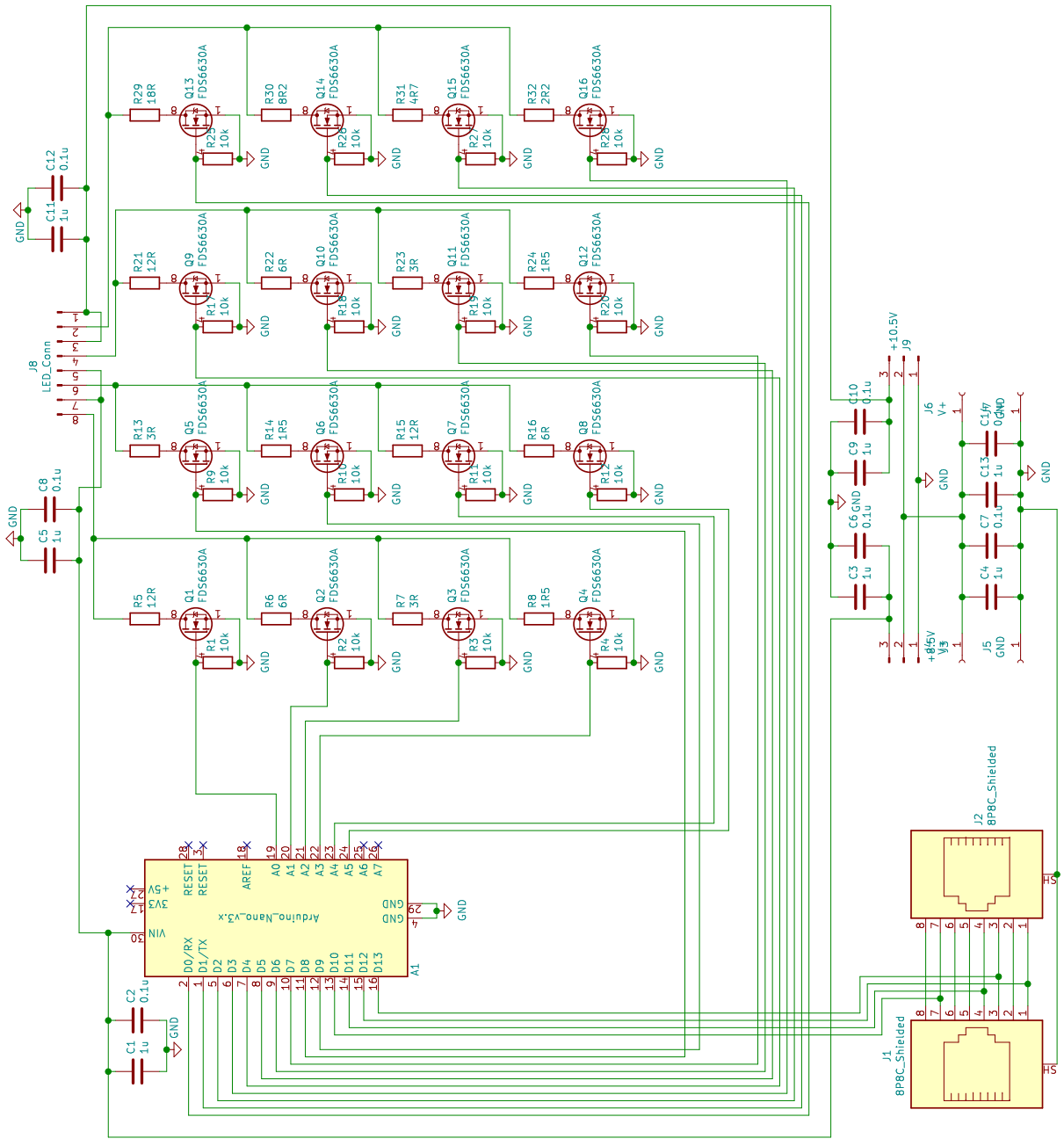

Figure D.1: Schematics for one transmitter module of the testbed presented in Chapter 7.

Bibliography

Journal and Conference Articles

[AM+22] H. Abumarshoud, L. Mohjazi, O. A. Dobre, M. Di Renzo, M. A. Imran, and H. Haas, "LiFi through reconfigurable intelligent surfaces: A new frontier for 6G?" *IEEE Vehicular Technology Magazine*, vol. 17, no. 1, pp. 37–46, Mar. 2022. DOI: 10.1109/MVT.2021.3121647.

[AV+18] A. Agrawal, R. Verschueren, S. Diamond, and S. Boyd, "A rewriting system for convex optimization problems," *Journal of Control and Decision*, vol. 5, no. 1, pp. 42–60, Jan. 2018. DOI: 10.1080/23307706.2017.1397554.

[AM+18] S. Al-Ahmadi, O. Maraqa, M. Uysal, and S. M. Sait, "Multi-user visible light communications: State-of-the-art and future directions," *IEEE Access*, vol. 6, pp. 70 555–70 571, 2018. DOI: 10.1109/ACCESS.2018.2879885.

[BS06] N. Bansal and M. Sviridenko, "The Santa Claus problem," in *Proceedings of the thirty-eighth annual ACM symposium on Theory of computing - STOC '06*, Seattle, WA, USA, May 2006, pp. 31–40. DOI: 10.1145/1132516.1132522.

[BK+93] J. R. Barry, J. M. Kahn, W. J. Krause, E. A. Lee, and D. G. Messerschmitt, "Simulation of multipath impulse response for indoor wireless optical channels," *IEEE Journal on Selected Areas in Communications*, vol. 11, no. 3, pp. 367–379, Apr. 1993. DOI: 10.1109/49.219552.

[CR+18] A. Chaaban, Z. Rezki, and M.-S. Alouini, "Capacity bounds and high-SNR capacity of MIMO intensity-modulation optical channels," *IEEE Transactions on Wireless Communications*, vol. 17, no. 5, pp. 3003–3017, May 2018. DOI: 10.1109/TWC.2018.2805726.

[CR+17] A. Chaaban, Z. Rezki, and M.-S. Alouini, "Fundamental limits of parallel optical wireless channels: Capacity results and outage formulation," *IEEE Transactions on Wireless Communications*, vol. 65, no. 1, pp. 296–311, Jan. 2017. DOI: 10.1109/TCOMM.2016.2621743.

[CM+16] J. Chau, C. Morales, and T. Little, "Using spatial light modulators in MIMO visible light communication receivers to dynamically control the optical channel," in *International Conference on Embedded Wireless Systems and Networks (EWSN), Graz, Austria*, Feb. 2016.

[CV97] B. Chen and A. P. Vestjens, "Scheduling on identical machines: How good is LPT in an on-line setting?" *Operations Research Letters*, vol. 21, no. 4, pp. 165–169, Nov. 1997. DOI: 10.1016/S0167-6377(97)00040-0.

[CA+18] X. Chen, C. Antonelli, S. Chandrasekhar, G. Raybon, A. Mecozzi, M. Shtaif, and P. Winzer, "Kramers-Kronig receivers for 100-km datacenter interconnects," *IEEE/OSA Journal of Lightwave Technology*, vol. 36, no. 1, pp. 79–89, Jan. 2018. DOI: 10.1109/JLT.2018.2793460.

[CM+17] X. Chen, C. Min, and J. Guo, "Visible light communication system using silicon photocell for energy gathering and data receiving," *International Journal of Optics*, vol. 2017, Art. no. 6207123, Jan. 2017. DOI: 10.1155/2017/6207123.

[CC+15] C.-W. Chow, C.-Y. Chen, and S.-H. Chen, "Visible light communication using mobile-phone camera with data rate higher than frame rate," *Optics Express*, vol. 23, no. 20, pp. 26 080–26 085, Oct. 2015. DOI: 10.1364/OE.23.026080.

[CS+89] F. Chung, J. Salehi, and V. Wei, "Optical orthogonal codes: Design, analysis and applications," *IEEE Transactions on Information Theory*, vol. 35, no. 3, pp. 595–604, May 1989. DOI: 10.1109/18.30982.

[DB16] S. Diamond and S. Boyd, "CVXPY: A Python-embedded modeling language for convex optimization," *Journal of Machine Learning Research*, vol. 17, no. 83, pp. 2909–2913, Jan. 2016.

[DS+12] S. Dimitrov, S. Sinanovic, and H. Haas, "Clipping noise in OFDM-based optical wireless communication systems," *IEEE Transactions on Communications*, vol. 60, no. 4, pp. 1072–1081, Apr. 2012. DOI: 10.1109/TCOMM.2012.022712.100493.

[EM+10] H. Elgala, R. Mesleh, and H. Haas, "Impact of LED nonlinearities on optical wireless OFDM systems," in *21st Annual IEEE International Symposium on Personal, Indoor and Mobile Radio Communications*, Istanbul, Turkey, 2010, pp. 634–638. DOI: 10.1109/PIMRC.2010.5671734.

[FH13] T. Fath and H. Haas, "Performance comparison of MIMO techniques for optical wireless communications in indoor environments," *IEEE Transactions on Communications*, vol. 61, no. 2, pp. 733–742, Feb. 2013. DOI: 10.1109/TCOMM.2012.120512.110578.

[FG+22] D. Fischer, J. Golak, and M. Mnich, "Exponentially faster fixed-parameter algorithms for high-multiplicity scheduling," Mar. 2022. DOI: 10.15480/882.4228. arXiv: 2203.03600.

[FH18] G. J. M. Forkel and P. A. Hoeher, "Constrained intensity superposition: A hardware-friendly modulation method," *IEEE/OSA Journal of Lightwave Technology*, vol. 36, no. 3, pp. 658–665, Feb. 2018. DOI: 10.1109/JLT.2017.2774926.

[FD+12] F.-A. Fortin, F.-M. De Rainville, M.-A. Gardner, M. Parizeau, and C. Gagné, "DEAP: Evolutionary algorithms made easy," *Journal of Machine Learning Research*, vol. 13, pp. 2171–2175, Jul. 2012.

[GB79] F. Gfeller and U. Bapst, "Wireless in-house data communication via diffuse infrared radiation," *Proceedings of the IEEE*, vol. 67, no. 11, pp. 1474–1486, Nov. 1979. DOI: 10.1109/PROC.1979.11508.

[Gon+16] C.-S. A. Gong *et al.*, "The high-efficiency LED driver for visible light communication applications," *Nature Sci. Rep.*, vol. 6, Art. no. 30991, Aug. 2016. DOI: 10.1038/srep30991.

[GI+77] T. Gonzalez, O. H. Ibarra, and S. Sahni, "Bounds for LPT schedules on uniform processors," *SIAM Journal on Computing*, vol. 6, no. 1, pp. 155–166, Mar. 1977. DOI: 10.1137/0206013.

[GP+13] L. Grobe, A. Paraskevopoulos, J. Hilt, D. Schulz, F. Lassak, F. Hartlieb, C. Kottke, V. Jungnickel, and K.-D. Langer, "High-speed visible light communication systems," *IEEE Communications Magazine*, vol. 51, no. 12, pp. 60–66, Dec. 2013. DOI: 10.1109/MCOM.2013.6685758.

[GL+07] J. Grubor, S. C. J. Lee, K. Langer, T. Koonen, and J. W. Walewski, "Wireless high-speed data transmission with phosphorescent white-light LEDs," presented at the 33rd European Conference and Exhibition of Optical Communication (ECOC), Berlin, Germany, 2007, pp. 1–2.

[GC18] A. K. Gupta and A. Chockalingam, "Performance of MIMO modulation schemes with imaging receivers in visible light communication," *IEEE/OSA Journal of Lightwave Technology*, vol. 36, no. 10, pp. 1912–1927, May 2018. DOI: 10.1109/JLT.2018.2795698.

[HY+20] H. Haas, L. Yin, C. Chen, S. Videv, D. Parol, E. Poves, H. Alshaer, and M. S. Islim, "Introduction to indoor networking concepts and challenges in LiFi," *Journal of Optical Communications and Networking*, vol. 12, no. 2, pp. A190–A203, Feb. 1, 2020. DOI: 10.1364/JOCN.12.00A190.

[HK+22] A. Harlakin, A. Krohn, and P. A. Hoeher, "Liquid crystal display based angle-of-arrival estimation of a single light source," *IEEE Photonics Journal*, vol. 14, no. 3, Art. no. 6829312, Jun. 2022. DOI: 10.1109/JPHOT.2022.3172511.

[HC+13] Y. Hong, J. Chen, Z. Wang, and C. Yu, "Performance of a precoding MIMO system for decentralized multiuser indoor visible light communications," *IEEE Photonics Journal*, vol. 5, no. 4, Art. no. 7800211, Aug. 2013. DOI: 10.1109/JPHOT.2013.2274766.

[JM17] K. Jansen and M. Maack, "An EPTAS for scheduling on unrelated machines of few different types," vol. 81, Oct. 2017, pp. 4134–4164. DOI: 10.1007/s00453-019-00581-w.

[JW+18] R. Jiang, Z. Wang, X. Zhu, and Q. Wang, "Interference-free LED allocation for visible light communications with fisheye lens," *IEEE/OSA Journal of Lightwave Technology*, vol. 36, no. 3, pp. 626–636, Feb. 2018. DOI: 10.1109/JLT.2017.2772325.

[KB97] J. M. Kahn and J. R. Barry, "Wireless infrared communications," *Proceedings of the IEEE*, vol. 85, no. 2, pp. 265–298, Feb. 1997. DOI: 10.1109/5.554222.

[Koo18] T. Koonen, "Indoor optical wireless systems: Technology, trends, and applications," *IEEE/OSA Journal of Lightwave Technology*, vol. 36, no. 8, pp. 1459–1467, Apr. 2018. DOI: 10.1109/JLT.2017.2787614.

[KG+18] T. Koonen, F. Gomez-Agis, F. Huijskens, K. A. Mekonnen, Z. Cao, and E. Tangdiongga, "High-capacity optical wireless communication using two-dimensional IR beam steering," *IEEE/OSA Journal of Lightwave Technology*, vol. 36, no. 19, pp. 4486–4493, Oct. 2018. DOI: 10.1109/JLT.2018.2834374.

[KF+17] A. Krohn, G. J. M. Forkel, P. A. Hoeher, and S. Pachnicke, "Capacity-increasing 3D spatial demultiplexer design for optical wireless MIMO transmission," presented at the 2017 European Conference on Optical Communication (ECOC), Gothenburg, Sweden, 2017, pp. 1–3. DOI: 10.1109/ECOC.2017.8346021.

[KF+19] A. Krohn, G. J. M. Forkel, P. A. Hoeher, and S. Pachnicke, "LCD-based optical filtering suitable for non-imaging channel decorrelation in VLC applications," *IEEE/OSA Journal of Lightwave Technology*, vol. 37, no. 23, pp. 5892–5898, Dec. 2019. DOI: 10.1109/JLT.2019.2941734.

[KH+22] A. Krohn, A. Harlakin, S. Arms, S. Pachnicke, and P. A. Hoeher, "Impact of liquid crystal based interference mitigation and precoding on the multiuser performance of VLC massive MIMO arrays," *IEEE Photonics Journal*, vol. 14, no. 5, Art. no. 7348112, Oct. 2022. DOI: 10.1109/JPHOT.2022.3199614.

[KH+20] A. Krohn, P. A. Hoeher, and S. Pachnicke, "Single-LED VLC-transmission with AMI and RZ-OOK for dimming support at fixed data rate," presented at the Advanced Photonics Congress (SPPCom 2020), Montreal, Canada, 2020. DOI: 10.1364/SPPCOM.2020.SpM4I.3.

[KH+18a] A. Krohn, P. A. Hoeher, and S. Pachnicke, "Visible light communication with multicarrier modulation utilizing a buck-converter circuit as efficient LED driver," in *Proc. ITG-Fachtagung Photonische Netze*, Leipzig, Germany, 2018, pp. 48–52.

[KH+18b] A. Krohn, P. A. Hoeher, and S. Pachnicke, "Visible light tricolor LED-to-camera data transmission suitable for internet-of-things and sensor applications," presented at the 2018 European Conference on Optical Communication (ECOC), Rome, 2018, pp. 1–3. DOI: 10.1109/ECOC.2018.8535387.

[KP+22] A. Krohn, S. Pachnicke, and P. A. Hoeher, "Genetic optimization of liquid crystal matrix based interference suppression for VLC MIMO transmissions," *IEEE Photonics Journal*, vol. 14, no. 1, Art. no. 7300705, Feb. 2022. DOI: 10.1109/JPHOT.2021.3126211.

[Lee91] C.-Y. Lee, "Parallel machines scheduling with nonsimultaneous machine available time," *Discrete Applied Mathematics*, vol. 30, no. 1, pp. 53–61, Jan. 1991. DOI: 10.1016/0166-218X(91)90013-M.

[LH+19] X. Li, B. Hussain, J. Kang, H. S. Kwok, and C. P. Yue, "Smart μLED display-VLC system with a PD-based/camera-based receiver for NFC applications," *IEEE Photonics Journal*, vol. 11, no. 1, Art. no. 7901008, Feb. 2019. DOI: 10.1109/JPHOT.2019.2892948.

[LC+16] K. Liang, C.-W. Chow, and Y. Liu, "RGB visible light communication using mobile-phone camera and multi-input multi-output," *Optics Express*, vol. 24, no. 9, pp. 9383–9388, May 2016. DOI: 10.1364/OE.24.009383.

[ML+15] H. Ma, L. Lampe, and S. Hranilovic, "Coordinated broadcasting for multiuser indoor visible light communication systems," *IEEE Transactions on Communications*, vol. 63, no. 9, pp. 3313–3324, Sep. 2015. DOI: 10.1109/TCOMM.2015.2452254.

[NN+21a] A. R. Ndjiongue, T. M. N. Ngatched, O. A. Dobre, and H. Haas, "Re-configurable intelligent surface-based VLC receivers using tunable liquid-crystals: The concept," *IEEE/OSA Journal of Lightwave Technology*, vol. 39, no. 10, pp. 3193–3200, May 2021. DOI: 10.1109/JLT.2021.3059599.

[NN+21b] A. R. Ndjiongue, T. M. N. Ngatched, O. A. Dobre, and H. Haas, "Toward the use of re-configurable intelligent surfaces in VLC systems: Beam steering," *IEEE Wireless Communications*, vol. 28, no. 3, pp. 156–162, Jun. 2021. DOI: 10.1109/MWC.001.2000365.

[NN+22] A. R. Ndjiongue, T. M. Ngatched, O. A. Dobre, and H. Haas, "Digital RIS (DRIS): The future of digital beam management in RIS-assisted OWC systems," *IEEE/OSA Journal of Lightwave Technology*, vol. 40, no. 16, pp. 5597–5604, Aug. 2022. DOI: 10.1109/JLT.2022.3176762.

[NH+15] A. Nuwanpriya, S. Ho, and C. S. Chen, "Indoor MIMO visible light communications: Novel angle diversity receivers for mobile users," *IEEE Journal on Selected Areas in Communications*, vol. 33, no. 9, pp. 1780–1792, Sep. 2015. DOI: 10.1109/JSAC.2015.2432514.

[OT+18] H. G. Olanrewaju, J. Thompson, and W. O. Popoola, "Performance of optical spatial modulation in indoor multipath channel," *IEEE Transactions on Wireless Communications*, vol. 17, no. 9, pp. 6042–6052, Sep. 2018. DOI: 10.1109/TWC.2018.2854573.

[PK+11] K.-H. Park, Y.-C. Ko, and M.-S. Alouini, "A novel power and offset allocation method for spatial multiplexing MIMO systems in optical wireless channels," in *Proceedings IEEE GLOBECOM Workshops*, Houston, TX, USA, 2011, pp. 823–827. DOI: 10.1109/GLOCOMW.2011.6162569.

[PO+17] K. Park, H. M. Oubei, W. G. Alheadary, B. S. Ooi, and M. Alouini, "A novel mirror-aided non-imaging receiver for indoor 2×2 MIMO-visible light communication systems," *IEEE Transactions on Wireless Communications*, vol. 16, no. 9, pp. 5630–5643, Sep. 2017. DOI: 10.1109/TWC.2017.2712689.

[PG+12] R. Paudel, Z. Ghassemlooy, H. Le Minh, S. Rajbhandari, and E. Leitgeb, "Lambertian source modelling of free space optical ground-to-train communications," presented at the 2012 8th International Symposium on Communication Systems, Networks & Digital Signal Processing (CSNDSP), Poznan, Poland, 2012, pp. 1–5. DOI: 10.1109/CSNDSP.2012.6292724.

[PP19] T. V. Pham and A. T. Pham, "Coordination/cooperation strategies and optimal zero-forcing precoding design for multi-user multi-cell VLC networks," *IEEE Transactions on Communications*, vol. 67, no. 6, pp. 4240–4251, Jun. 2019. DOI: 10.1109/TCOMM.2019.2900675.

[RA+17] V. P. Rachim, J. An, P. N. Quan, and W.-Y. Chung, "A novel smartphone camera-LED communication for clinical signal transmission in mHealth-rehabilitation system," presented at the 39th Annual International Conference of the IEEE Engineering in Medicine and Biology Society (EMBC), Jeju, Korea (South), 2017, pp. 3437–3440. DOI: 10.1109/EMBC.2017.8037595.

[RR+12] S. Rajagopal, R. Roberts, and S.-K. Lim, "IEEE 802.15.7 visible light communication: Modulation schemes and dimming support," *IEEE Communications Magazine*, vol. 50, no. 3, pp. 72–82, Mar. 2012. DOI: 10.1109/MCOM.2012.6163585.

[SS+19] M. L. G. Salmento, G. M. Soares, J. M. Alonso, and H. A. C. Braga, "A dimmable offline LED driver with OOK-M-FSK modulation for VLC applications," *IEEE Transactions on Industrial Electronics*, vol. 66, no. 7, pp. 5220–5230, Jul. 2019. DOI: 10.1109/TIE.2018.2868022.

[Sch16] H. Schulze, "Frequency-domain simulation of the indoor wireless optical communication channel," *IEEE Transactions on Communications*, vol. 64, no. 6, pp. 2551–2562, Jun. 2016. DOI: 10.1109/TCOMM.2016.2556684.

[Sch11] H. Schulze, "Some good reasons for using OFDM in optical wireless communications," in *Proceedings International OFDM Workshop*, Hamburg, Germany, 2011, pp. 1–5.

[SH22] H. Schulze and P. A. Hoeher, "On the general error event probability evaluation of optical intensity modulation schemes," *IEEE Photonics Journal*, vol. 14, no. 5, Art. no. 7954008, Oct. 2022. DOI: 10.1109/JPHOT.2022.3207834.

[SS+04] Q. Spencer, A. Swindlehurst, and M. Haardt, "Zero-forcing methods for downlink spatial multiplexing in multiuser MIMO channels," *IEEE Transactions on Signal Processing*, vol. 52, no. 2, pp. 461–471, Feb. 2004. DOI: 10.1109/TSP.2003.821107.

[SP92] G. Spruce and R. D. Pringle, "Polymer dispersed liquid crystal (PDLC) films," *Electronics Communication Engineering Journal*, vol. 4, no. 2, pp. 91–100, Apr. 1992. DOI: 10.1049/ecej:19920017.

[LK20] M. Le-Tran and S. Kim, "Superposed constellation design for spatial multiplexing visible light communication systems," *Optics Express*, vol. 28, no. 25, pp. 38 293–38 303, Dec. 2020. DOI: 10.1364/OE.412080.

[VK+10] J. Vucic, C. Kottke, S. Nerreter, K.-D. Langer, and J. W. Walewski, "513 mbit/s visible light communications link based on DMT-modulation of a white LED," *IEEE/OSA Journal of Lightwave Technology*, vol. 28, no. 24, pp. 3512–3518, Dec. 2010. DOI: 10.1109/JLT.2010.2089602.

[Wag31] C. Wagner, "Theory of current rectifiers," *Phys. Z*, vol. 32, pp. 641–645, 1931.

[WT+15] Z. Wang, D. Tsonev, S. Videv, and H. Haas, "On the design of a solar-panel receiver for optical wireless communications with simultaneous energy harvesting," *IEEE Journal on Selected Areas in Communications*, vol. 33, no. 8, pp. 1612–1623, Aug. 2015. DOI: 10.1109/JSAC.2015.2391811.

[WL+12] G. Wetzstein, D. Lanman, M. Hirsch, and R. Raskar, "Tensor displays: Compressive light field synthesis using multilayer displays with directional backlighting," *ACM Transactions on Graphics*, vol. 31, no. 4, Art. no. 80, Jul. 2012. DOI: 10.1145/2185520.2185576.

[YC+18] H. Yang, C. Chen, W.-D. Zhong, and A. Alphones, "Joint precoder and equalizer design for multi-user multi-cell MIMO VLC systems," *IEEE Transactions on Vehicular Technology*, vol. 67, no. 12, pp. 11 354–11 364, Dec. 2018. DOI: 10.1109/TVT.2018.2876788.

[YB+13] Z. Yu, R. J. Baxley, and G. T. Zhou, "Multi-user MISO broadcasting for indoor visible light communication," in *Proceedings IEEE International Conference on Acoustics, Speech and Signal Processing*, Vancouver, BC, Canada, 2013, pp. 4849–4853. DOI: 10.1109/ICASSP.2013.6638582.

Books and PhD Theses

[Arn15] S. Arnon, *Visible Light Communication*. Cambridge: Cambridge University Press, 2015.

[Che11] R. H. Chen, *Liquid Crystal Displays: Fundamental Physics and Technology*. Hoboken, N.J.: Wiley, 2011.

[CT06] T. M. Cover and J. A. Thomas, *Elements of Information Theory, 2nd ed.* Hoboken, N.J.: Wiley, 2006.

[Den18] X. Deng, *Throughput, Power Consumption and Interference Considerations in Visible Light Communication*. Ph.D. dissertation, Technische Universiteit Eindhoven, 2018.

[Don00] S. Donati, *Photodetectors: Devices, Circuits, and Applications*. Upper Saddle River, N.J.: Prentice-Hall, 2000.

[Gra96] J. Graeme, *Photodiode Amplifiers: Op Amp Solutions*. New York: McGraw Hill, 1996.

[Hoe13] P. A. Hoeher, *Grundlagen der digitalen Informationsübertragung, 2. Auflage*. Wiesbaden: Springer Fachmedien, 2013.

[Hoe19] P. A. Hoeher, *Visible Light Communications: Theoretical and Practical Foundations*. Munich: Hanser Publishers, 2019.

[HH89] P. Horowitz and W. Hill, *The Art of Electronics, Second Edition*. Cambridge: Cambridge University Press, 1989.

[Kam04] K.-D. Kammeyer, *Nachrichtenübertragung, 3. Auflage*. Wiesbaden: Teubner, 2004.

[93] "Licht," in *Der Brockhaus in fünf Bänden, 8., neu bearbeitete Auflage*. Mannheim: F.A. Brockhaus GmbH, 1993.

[Par80] B. N. Parlett, *The Symmetric Eigenvalue Problem*. Englewood Cliffs, N.J.: Prentice-Hall, 1980.

[Reh03] J. Rehrmann, *Das Netzteil- und Konverterhandbuch*. Gudensberg: edition trifolium, 2003.

[WW+18] Z. Wang, Q. Wang, W. Huang, and Z. Xu, *Visible Light Communications: Modulation and Signal Processing*. Hoboken, N.J.: Wiley, 2018.

Patents

[Bel80] A. G. Bell, "Photophone transmitter," U.S. Patent 235496A, Dec. 14, 1880.

[Elr93] S. A. Elrod, "Infrared beam steering system using diffused infrared light and liquid crystal apertures," U.S. Patent 5528391A, Jun. 4, 1993.

Standards, Technical Reports, and Online Sources

[Bak17] B. C. Baker, "Automating circuit designs for photodiode amplifiers," *TI Analog Applications Journal*, AAJ 1Q 2017. [Online]. Available: `http://www.ti.com/lit/pdf/slyt703` (visited on 10/06/2022).

[Cal14] J. Caldwell, "1 MHz, single-supply, photodiode amplifier reference design," *TI Designs – Precision: Verified Design*, Nov. 2014. [Online]. Available: `http://www.ti.com/lit/ug/tidu535/tidu535.pdf` (visited on 10/06/2022).

[Fai03] Fairchild Semiconductor, *Single n-channel, logic level, powertrench MOSFET*, FDS6670A, Rev. F, Jun. 2003.

[Han22] T. Handte, *AWGN Channel Capacity*, Webdemo, Institute of Telecommunications, University of Stuttgart, Germany, Nov. 2022. [Online]. Available: `http://webdemo.inue.uni-stuttgart.de`.

[IEE19] IEEE Standards Association, "IEEE 802.15 local and metropolitan area networks–part 15.7: Short-range optical wireless communications," Tech. Rep. 802.15.7-2018, Apr. 2019. [Online]. Available: `https://standards.ieee.org/standard/802_15_7-2018.html`.

[ITU19] ITU, "ITU-R Recommendation G.9991: High-speed indoor visible light communication transceiver - Sytem architecture, physical layer and data link layer specifications," International Telecommunication Union, Tech. Rep., Mar. 2019. [Online]. Available: `https://www.itu.int/rec/T-REC-G.9991/en`.

[LED18] LED Engin, *High luminous efficacy RGBA LED emitter*, LZC-03MA07, Rev. 1.8, Nov. 2018.

[OSR20] OSRAM Opto Semiconductors GmbH, *Radial sidelooker silicon pin photodiode*, SFH 206 K, Rev. 1.4, Jan. 2020.